












Excavation Simulations and Cutting Tool Wear

3

Lukas Brackmann , Arne Röttger, Hoang-Giang Bui , Sahir Butt ,
Golnaz Hoormazdi , Abdiel Ramon Leon Bal, Sebastian Priebe ,
Dennis Wingender, Hongwei Yang, Daniel Balzani , Klaus Hackl ,
Günther Meschke , Inka Mueller , and Jörg Renner

L. Brackmann (✉)

Materials Technology, Ruhr-Universität Bochum, Bochum, Germany

e-mail: lukas.brackmann@rub.de

A. Röttger

New Production Technologies and Materials, Bergische Universität Wuppertal, Wuppertal,
Germany

e-mail: roettger@uni-wuppertal.de

H.-G. Bui · G. Hoormazdi · K. Hackl

Mechanics of Materials, Ruhr-Universität Bochum, Bochum, Germany

e-mail: giang.bui@rub.de

G. Hoormazdi

e-mail: golnaz.hoormazdi@rub.de

K. Hackl

e-mail: klaus.hackl@rub.de

S. Butt · A. R. Leon Bal · S. Priebe · G. Meschke

Structural Mechanics, Ruhr-Universität Bochum, Bochum, Germany

e-mail: sahir.butt@rub.de

A. R. Leon Bal

e-mail: abdiel.leonBal@rub.de

S. Priebe

e-mail: Sebastian.Priebe@ruhr-uni-bochum.de

G. Meschke

e-mail: guenther.meschke@rub.de

© The Author(s) 2023

G. Meschke et al. (Eds.), *Interaction Modeling in Mechanized Tunneling*,

https://doi.org/10.1007/978-3-031-24066-9_3

Abstract

The mechanized tunnel construction is carried out by tunnel boring machines, in which the soil in front of the working face is removed, and the tunnel lining is carried out with shotcrete or the setting of segments and their back injection. Advancements in this field aim towards increase of the excavation efficiency and increase of the tool lifetime, especially in rock-dominated grounds. The latter is achieved by understanding the wear mechanisms abrasion and surface-fatigue, and by knowledge of the microstructure-property relation of the utilized materials. Improvements for tool concepts are derived, based on experiments and simulations. A key parameter towards efficient rock excavation is the shape of the cutting edge of the utilized disc cutters. Sharp cutting edges have proven to generate higher rock excavation rates compared to blunt ones. The compressive strength of the utilized steel has to be high, to inhibit plastic deformation and thereby to maintain sharp cutting edges. This requirement competes with the demand for toughness, which is necessary to avoid crack-growth in the case of cyclic loading. Solutions for this contradiction lie in specially designed multiphase microstructures, containing both hard particles and ductile microstructural constituents. Besides adapting the alloying concept, these required microstructures and the associated properties can be adjusted by specific heat-treatments.

D. Wingender · D. Balzani

Continuum Mechanics, Ruhr-Universität Bochum, Bochum, Germany

e-mail: dennis.wingender@rub.de

D. Balzani

e-mail: daniel.balzani@rub.de

H. Yang

School of Civil Engineering, Sun Yat-sen University, Guangzhou, China

e-mail: yanghw9@mail.sysu.edu.cn

I. Mueller

Technical Mechanics, Bochum University of Applied Sciences, Bochum, Germany

e-mail: inka.mueller@hs-bochum.de

J. Renner

Experimental Geophysics, Ruhr-Universität Bochum, Bochum, Germany

e-mail: joerg.renner@rub.de

3.1 Introduction

The excavation of soil and rock in mechanized tunneling is fundamentally different from that in other tunnel construction methods, such as open construction pits or blast excavation. In mechanized tunneling, tools are attached to a rotating shield, which also defines the tunnel's diameter. Thereby, the tools are selected taking into account the geological conditions. For example, chisels and scrapers are used in the case of non-cohesive soil, as they remove the geomaterial in a similar manner as a shovel. In contrast, disc cutters are employed in soft and hard rock, where material degradation occurs by crack initiation, crack propagation, and spalling of rock fragments. The profitability of tunnel construction is largely defined by the efficiency and speed of soil excavation. The excavation efficiency decreases due to the wear of the tools, so they have to be replaced upon reaching their wear limit. Precise knowledge of the tool wear and the associated excavation efficiency is essential for planning optimal tool change intervals and estimating construction costs. This chapter deals with excavation of soil and medium-strength rock, and the wear of the tools used for their excavation. It is important to understand both the soil-tool interaction to describe the degradation mechanisms and the tool wear on the microscale, thus deriving optimal material concepts for tunneling tools.

At the beginning of this chapter, the fundamental principles of soil and rock excavation are explained, and the results of recent advancements in the understanding of the rock excavation process are presented. The results of rock indentation tests and numerical simulations form the base for future design optimizations of tunneling tools, aiming towards improved excavation efficiency. Subsequently, the results of numerical simulations of the interaction between tunneling tools, such as disc cutters and chisel tools, and various soils and rocks are discussed with a focus on the determination of evolving cutting forces, especially at material interfaces, as is the case if tunneling occurs in heterogeneous ground conditions.

In the second part, the material concepts and wear mechanisms of tunneling tools are examined. Tool wear is discussed on macro- and micro-scale by explaining the interaction of the different tool microstructures and the abrasive particles in the ground to be excavated. In addition to abrasive wear, special emphasis is placed on the influence of cyclic mechanical loading and the connected wear mechanism of surface spalling. Several material concepts, such as hardfacing alloys and tool steels, are considered concerning their abrasive wear resistance and fatigue resistance. Furthermore, existing test methods for abrasiveness of soil and rock, as well as fatigue tests are described and critically evaluated. The numerical simulations investigate the previously introduced wear mechanisms on meso- and microscale. Mesoscale simulations address abrasive wear and focus on the interaction of abrasive particles with the tool surface during a scratching process. A bridge is built toward the scratch behavior of multiple particles, as well as particle mixtures from single-scratch simulations. The microscale simulations explore the material response of hard phase containing materials under static and cyclic loading conditions. The underlying computational methods are explained in detail, and the results of crack propagation sim-

ulations in different hard-phase containing materials are presented. Subsequently, novel techniques of in-situ monitoring of tool wear and damages using vibration analysis are presented. An experimentally based proof of concept for detecting damaged disc cutters is provided, after a short digress into the fundamental principles of wear detection and vibration analysis. A transfer of the gained results concludes the chapter with practical recommendations on increasing tunneling efficiency and improving tool lifetime.

3.2 Excavation of Geomaterials in Mechanized Tunneling: Experiments and Simulations on Failure Mechanisms

Mechanized tunneling relies on tunnel boring machines (TBMs) that have to be equipped with appropriate tools for the excavation of the material along the anticipated path. The terminology regarding the material “below our feet”, for which we use the term “geomaterials” in an overarching sense, is unfortunately convoluted. Conventionally, the material below our feet is classified as either soil or rock. Appealingly simple, with only two groups, the classification and its use in different scientific communities bears complications. In geo-engineering, for example, the term “soil” is at times used synonymous with “ground,” the latter meaning “solid material below us” in an objective way. Furthermore, either group is diverse in composition and mechanical behavior. Soils represent loose and unconsolidated sediments produced by the deposition of particles after their transport through air or water over vastly variable distances. A first subgroup of soil, the organic soils, with the adjective often dropped in agricultural context, is characterized by a substantial fraction of organic matter and forms the pedosphere. The introduction of the two further subgroups, granular and cohesive soils, rests on a mixture of structural and mechanical characteristics. For soils, cohesiveness, actually at conflict with the defining “loose,” results from the presence of water that mediates and amplifies electrical forces between soil particles to the extent that they form aggregates with some shape stability, in cases associated with significant plasticity. While the mechanical property, cohesiveness, cannot be used alone to distinguish soils and rocks, the cause for the cohesion and its mechanical ramifications are strikingly different for them. The cohesiveness of rocks results from welding of grains, either by a “substance”, the cement, acting as a glue leading to lithification of sediments or by the formation of “intact” grain boundaries (held together by interatomic forces as in metals or ceramics) during their genesis (crystallization from melts or recrystallization by solid-state reactions).

The overall success and the predictability of costs of excavation projects critically hinge on an (in the best of cases) a-priori knowledge or an experience-based principal understanding of the deformation behavior of the subsurface material to be penetrated. The selection of an appropriate excavation technique and associated tools requires at least a material classification, but the more is known about strength parameters the better. The excavation techniques and the activated failure processes shift from soil to rock. Cutting

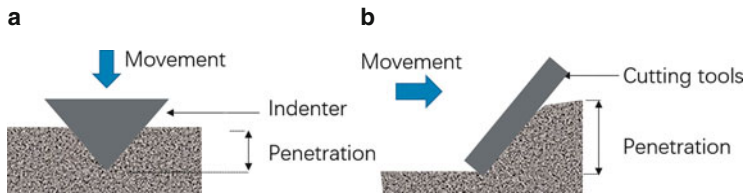


Fig. 3.1 Two basic processes in excavation: indentation (a) and cutting (b)

or scraping suffices to disintegrate soils, while indentation and fragmentation is required for rock (Fig. 3.1).

As a rule of thumb, the contents of organic matter decreases while the cohesiveness increases with depth. On an absolute scale, organic soils and cohesive soils exhibit compressive strengths as low as tens of kPa. The compressive strength of granular soils and highly porous sedimentary rocks overlap (1 to 10 MPa); crystalline rocks may exhibit strength up to a few hundreds of MPa. The significant changes in porosity during deformation and their effect on strength was first noted for soils; the related critical-state concept [38, 104] also has some applicability to porous rocks [22]. Likewise, the concept of effective stresses, introduced by Terzaghi for soils [93, 94], applies to rocks as well [71].

3.2.1 Excavation of Soft Soils

The mechanized excavation of soils by means of tunnel boring machines is characterized by the engagement of the scraper tools mounted on the cutting wheel with the ground. The TBM advancement actually leads to a strong and transient tool-soil interaction, during which the excavation tools penetrate the tunnel face and push the soil mass away, leading to destructuration and failure of the material that ultimately enters the excavation chamber. The excavation operation of soils involves the development of large displacements and deformations, as well as a strong coupling between skeleton deformation and pore pressure variations causing significant fluid flow in partially and fully saturated soils [63, 64]. The intrinsic complexity of mechanized excavation problems, associated to a great extent with the interaction between the excavation instrument and the penetrated soil, has stimulated experimental and numerical investigations [6–8, 52, 53] of tool-soil interaction processes. Here, we report on the development of an experimental device that allows for measuring the topology of the soil during the excavation and the evolution of the reaction forces on the tool when penetrating dry and partially saturated soils, and on the validation and application of single-phase [7, 8] and two-phase [53] numerical models based on the Particle Finite Element Method (PFEM) [68] coupled with a standard hypoplastic formulation for the modeling of granular materials [103].

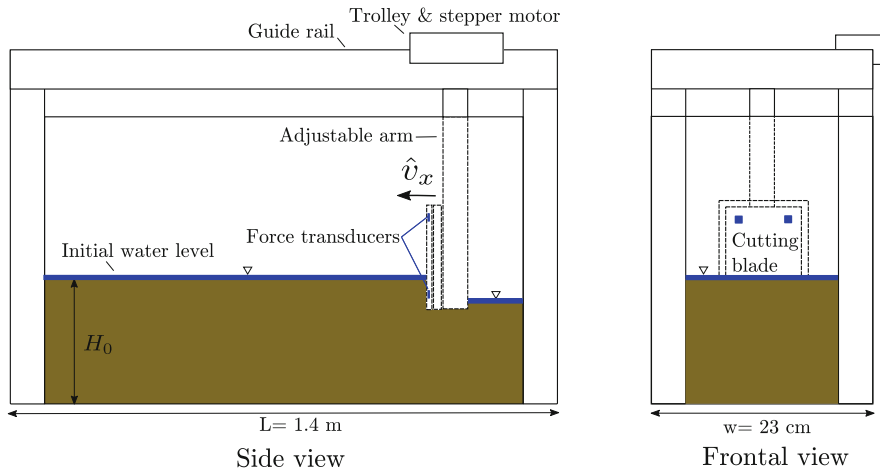


Fig. 3.2 Setup and main components of the developed excavation device (re-drawn after: [6])

3.2.1.1 RUB Excavation Device

The setup of the excavation device consists of a rectangular container filled in with sand and enclosed by four Plexiglass walls. The relevant dimensions are indicated in Fig. 3.2. The excavation tool is a rectangular Plexiglass panel with a height of 25 cm, displaced along the excavation container by a stepper motor and a trolley mounted on a dual linear guide rail system with sliding bearings. The excavation device permits adjusting the penetration depth of the cutting blade. Four force transducers, attached to the cutting blade, register reaction forces and torque during the experiment.

The excavation tests were carried out in dense Haltener Silbersand [76], a siliceous sand with rounded grains. The following conditions were considered in the experiments: initial height of sand in the container $H_0 = 30$ cm, penetration depth of the tool $d_p = 10$ cm, and horizontal velocity of the tool $\hat{v}_x = 1.2$ cm/s. After each test run, the sand was leveled to the same initial height (30 cm). Water-saturation is reached via a hose entering the container; water is added until a level is attained that slightly exceeds the soil surface.

3.2.1.2 Computational Analysis of Tool-Soil Interactions

The computational plane-strain and 3D PFEM simulations of tool-soil interactions for dry and water-saturated conditions, involving single and multiple cutting tool, used the configurations displayed in Fig. 3.3. Excavation analyses of dry soils were performed utilizing dimensions extracted from [20]: $L = 2.2$ m, width $w = 20$ cm, initial height of granular material $H_0 = 30$ cm, penetration depth of the tool $d_p = 20$ cm, height of the tool $H_{\text{tool}} = 25$ cm and its thickness $t_{\text{tool}} = 2.5$ cm. The tool moves with a prescribed horizontal velocity of $\hat{v}_x = 1.0$ cm/s. In simulations with multiple cutting tools, the horizontal velocity of the tools was $\hat{v}_x = 15$ cm/s. For simulation of the excavation of water-saturated soil, the model dimensions were: $L = 1.4$ m, $w = 23$ cm, $H_0 = 30$ cm, $d_p = 10$ cm, and $t_{\text{tool}} = 2.5$ cm.

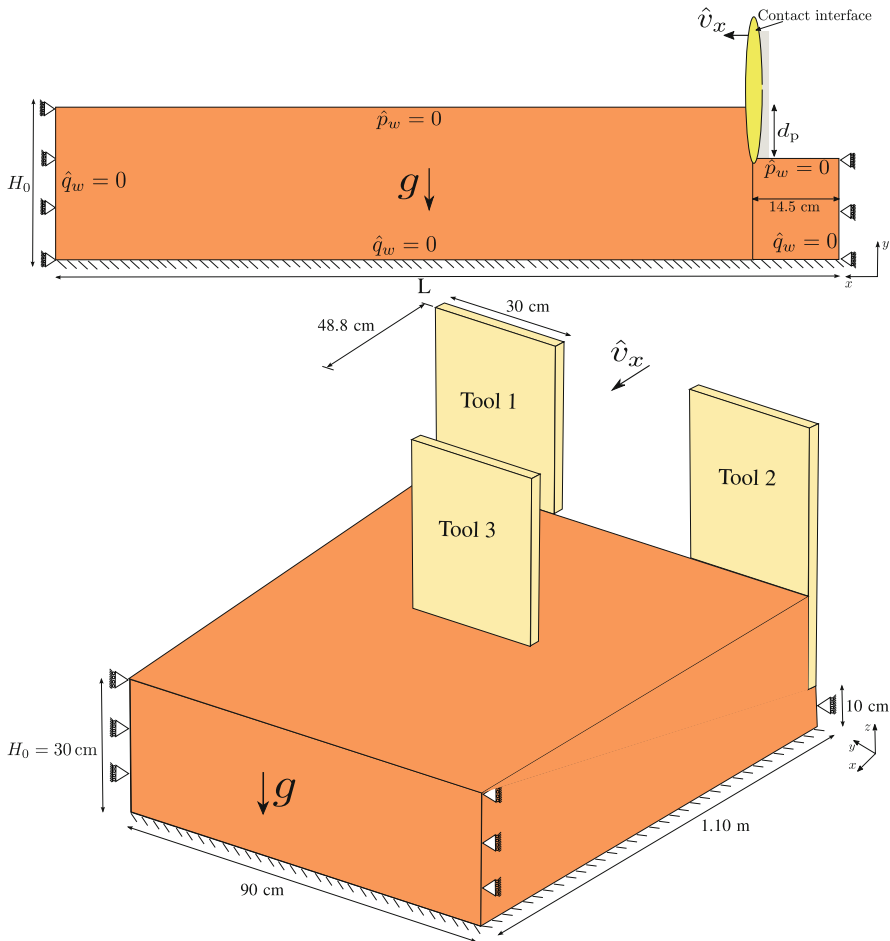


Fig. 3.3 Initial geometry, model setup and boundary conditions of the 2D (top, re-drawn after: [53]) and 3D (bottom, re-drawn after: [7]) PFEM excavation models

In this numerical model, the height of the tool is 5 cm larger than in the experiments (i.e. $H_{\text{tool}} = 30$ cm), to avoid soil over-passing the tool at the end. A horizontal tool velocity of 1.2 cm/s was applied. A frictional tool-soil interface discretized with triangular contact elements (shown as a red layer in Fig. 3.3, top, was considered in plane-strain excavation analyses, whereas a no-slip tool-soil interface was assumed for 3D simulations.

Excavation simulations for dry soil were performed assuming corn kernels [20]. The geotechnical and hypoplastic parameters adopted for corn can be found in [7]. The initial void ratio was set to $e_0 = 0.82$ (relative density of $I_d = 0.35$). Simulations of water-saturated soil, were carried out for Silbersand, assuming an initial void ratio of $e_0 = 0.66$ ($I_d = 0.70$). The hypoplastic parameters adopted for this sand are contained in [6, 53]. The constitutive model was initialized using at-rest later pressure conditions.

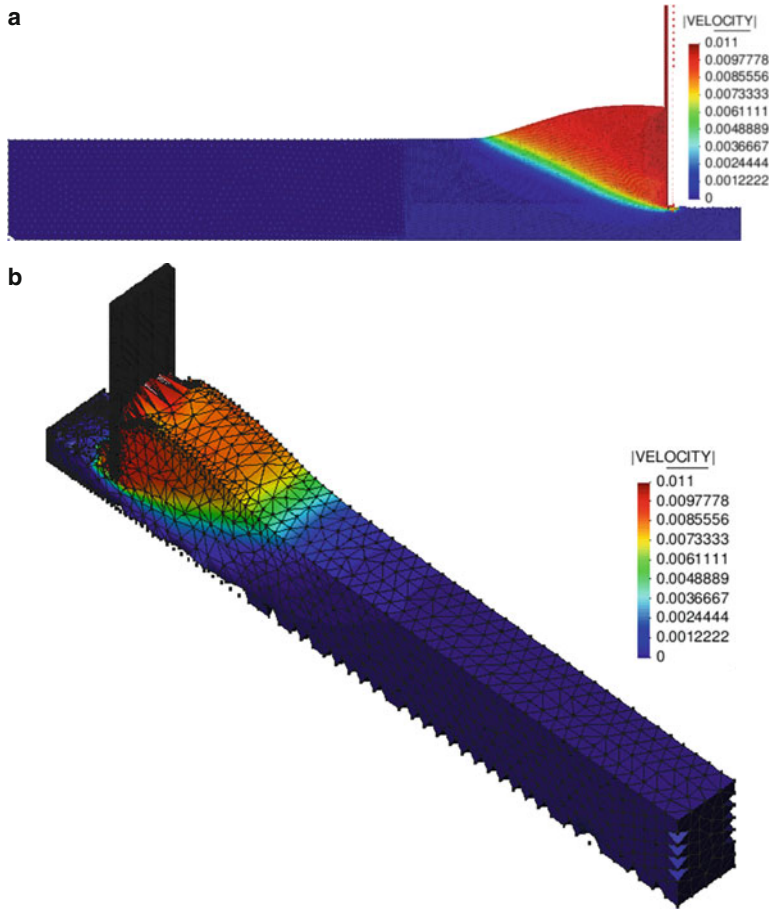


Fig. 3.4 Spatial distribution of the total velocities of the particles (in [m/s]) in the excavation according to the **a** 2D and **b** 3D excavation models, for a tool horizontal displacement of $S_x = 20$ cm

In both 2D and 3D numerical analyses assuming partially or fully saturated soil, the sides of the excavation models were impervious (Fig. 3.3), while the ground free surface was allowed to drain freely (i.e., $\hat{p}_w = 0$). In plane-strain simulations of partially saturated sand, the saturated hydraulic conductivity K_w^{sat} was estimated from the Kozeny-Carman permeability model [18]; the Soil-Water Characteristic Curve (SWRC) was defined via van Genuchten's model [97].

The spatial distributions of the total velocities of the particles in the deformed ground, according to the 2D and 3D excavation models (Fig. 3.4), show higher velocities near the cutting tool and within the heap of excavated material, than in the rest of the domain. The simulation results also show a shear slip plane in the velocity field, propagating from the bottom of the excavation tool towards the ground free surface.

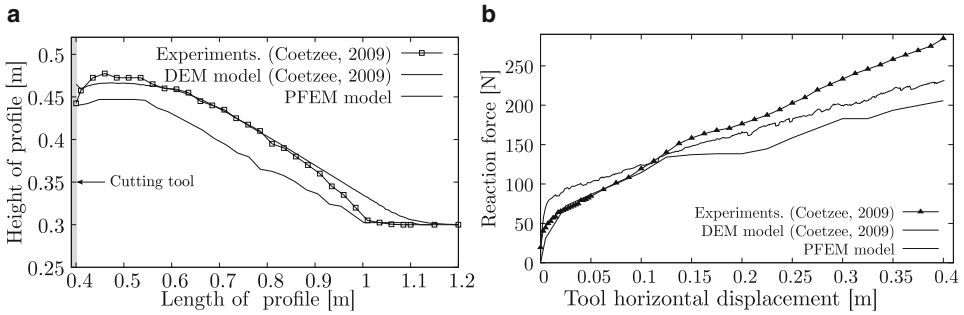


Fig. 3.5 **a** Profiles of the ground free surface for a tool horizontal displacement of $S_x = 40$ cm. **b** Evolution of the tool reaction forces, according to experiments and DEM simulations [20] as well as PFEM analyses [7] (re-drawn after: [7])

The profile of the ground free surface computed with the PFEM is compared with experimental and DEM results reported in [20] (Fig. 3.5a). In general, a very good correlation between laboratory results and numerical predictions from the hypoplastic PFEM model is observed for the assessed tool displacement. The evolution of the horizontal reaction force generated on the cutting tool vs. its horizontal displacement, displays an initial increase with a steep slope, where predictions obtained from PFEM analyses exceed DEM and laboratory results (Fig. 3.5b). As the excavation process continues, the reaction forces steadily increase due to the accumulation of granular material in front of the tool. For the evaluated horizontal displacement range of the tool, PFEM predictions [7] agree well with the results obtained from the DEM and the experiments presented in [20].

Tool-soil interaction analyses considering three cutting tools simultaneously excavating in soil are analyzed. The setup consists of one leading tool (tool 1) located ahead of the other two trailing tools (tool 2 and 3), which are positioned at the same level (Fig. 3.3, top). Similar to the PFEM results concerning excavations with a single tool (Fig. 3.4), distinctive shear slip lines emerge from the lower part of each cutting tool (Fig. 3.6a). The heaps in front of tools 1 and 2 exhibit a similar topology, characterized by an inclination towards the centerline of the container, while the heap in front of tool 3 resembles a semi-circular shape. Computed reaction forces on tools 1 (solid line) and 2 (dashed line) are very close, due to the similarity in the topologies of their associated excavation fronts, while for tool 3 (line with marks), higher reaction forces are calculated (Fig. 3.6b).

Excavation analyses in initially fully saturated Silbersand, are now considered. A staggered topology of the ground free surface occurs, i.e., bumps of soil develop ahead of the scrapper (Fig. 3.7a). In general, the computed and measured profiles of the free surface are in good agreement (Fig. 3.7b). For the assessed horizontal displacement of 35 cm, the maximum height attained by the heap of material in the test (denoted by \hat{H}_{\max}) was nearly $\hat{H}_{\max} = 20.26$ cm, at a horizontal distance of 11.03 cm from the tool. According to the PFEM simulations, the maximum height in the ground from the bottom of the tool (H_{\max})

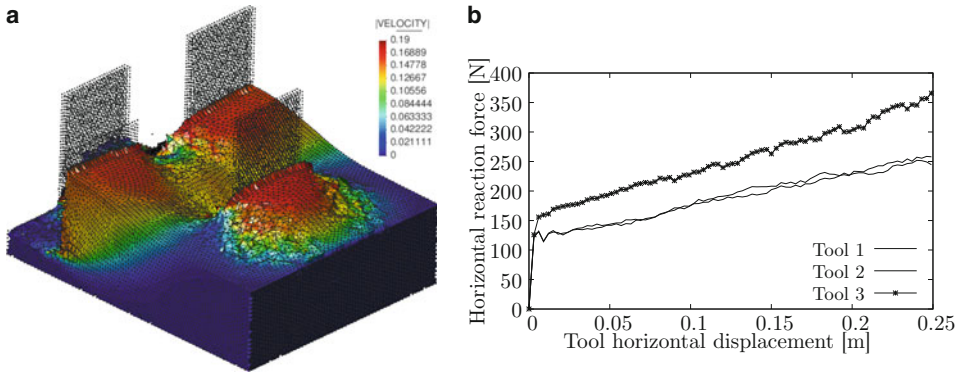


Fig. 3.6 **a** Spatial distribution of the total velocities of the particles (in [m/s]) for a horizontal displacement of the tools of $S_x = 20$ cm. **b** spatio-temporal evolution of the reaction forces in tools 1, 2 and 3 (re-drawn after: [7])

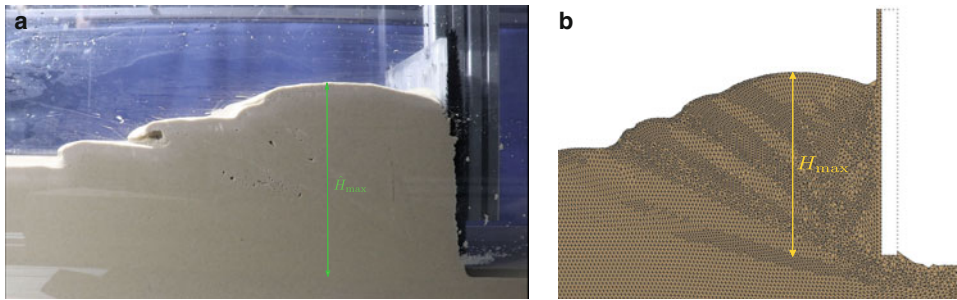


Fig. 3.7 **a** Measured and **b** computed profiles of the ground free surface for a tool horizontal displacement of $S_x = 35$ cm, in water-saturated excavations

is circa $H_{max} = 22.63$ cm computed at 10.29 cm ahead of the tool. It can also be observed a denser nodal distribution in shear deformation zones of the soil (i.e. shear bands) as compared to the rest of the excavation domain. This is achieved by means of an adaptive re-meshing procedure based on a soil dilation criterion, incorporated into the hypoplastic PFEM formulation for the improved capture of strain localization zones in the ground.

The capabilities of the proposed two-phase PFEM formulation are further assessed by means of the the computed and measured profiles of the ground free surface at selected tool displacements (Fig 3.8a). Experimental data (solid gray lines) show maximum heights of the excavation heap of ≈ 18.6 cm and 22.75 cm, for tool displacements of 25 cm and 45 cm, respectively. The maximum heights of the ground computed with the PFEM model (solid and dashed black lines), for corresponding tool displacements, are 18.9 cm and 25.5 cm. The computed and measured topology of the ground for the assessed tool displacements, are in good agreement.

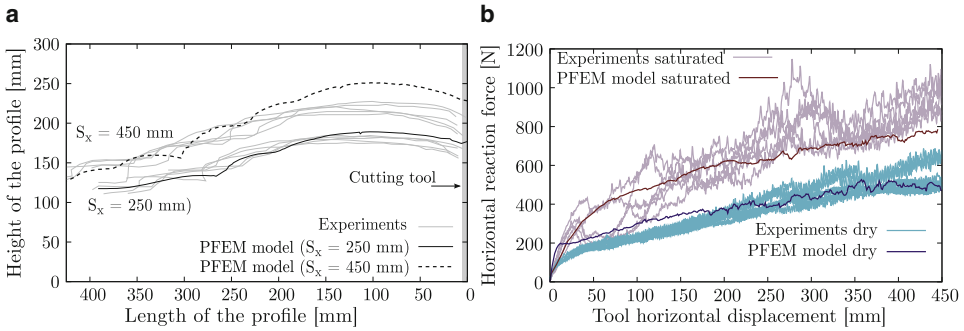


Fig. 3.8 Computed and measured **a** excavation profiles for tool horizontal displacements of $S_x = 25$ and $S_x = 45$ cm and **b** reaction force-tool displacement curves obtained from excavation analyses in dry and water-saturated sand (re-drawn after: [53])

We evaluate the tool reaction force-displacement curves generated during excavations in Silbersand (Fig. 3.8b). To complement the experiments performed in water-saturated sand, dry excavation tests were also carried out. Test results in initially fully saturated sand (red solid lines), show an initial increase of the reaction forces, followed by strong oscillations in the reaction forces, where a maximum reaction force of around 1100 N, at around 27.5 cm of tool displacement, is registered by the force transducers. Excavation experiments performed in dry conditions (aqua solid line), on the contrary, show a maximum reaction force of 490 N at the final displacement of the tool, corresponding to 45 cm. In this cases, no strong oscillations in the force plot are detected. Although the proposed model (results in dark red and dark aqua solid lines) is not able to fully reproduce the large oscillations observed in the reaction forces obtained from excavation tests in initially saturated sand, the numerical results lie within the experimental range.

Finally, 2D and 3D excavation analyses in fully saturated Silbersand, are presented. For these simulations, no-slip conditions at the tool-soil interface and a constant saturated hydraulic conductivity of $K_w^{\text{sat}} = 1 \times 10^{-4}$ m/s, are considered. Furthermore, the tool is horizontally displaced at constant velocity of 10 cm/s. The spatial distributions of pore water pressures in the deformed configuration of ground at a tool horizontal displacement of 36 cm, assuming initially loose i.e. $e_0 = 0.79$ ($I_d = 0.32$) and dense i.e. $e_0 = 0.70$ ($I_d = 0.58$) sands, are investigated (Figs. 3.9 and 3.10). For the evaluated tool displacement, pore pressures in the ground are mostly positive for initially loose sand, whereas for the denser specimen, negative pore pressures develop ahead of the excavation tool while the rest of the soil domain (e.g. near the left and bottom boundaries) undergoes positive pressures. Negative pore pressures are normally associated to the excavation [63] and strain localization phenomena [83] of dense, dilatant materials. Comparable distributions of pore pressures are computed with the 2D PFEM excavation model, for similar initial soil densities.

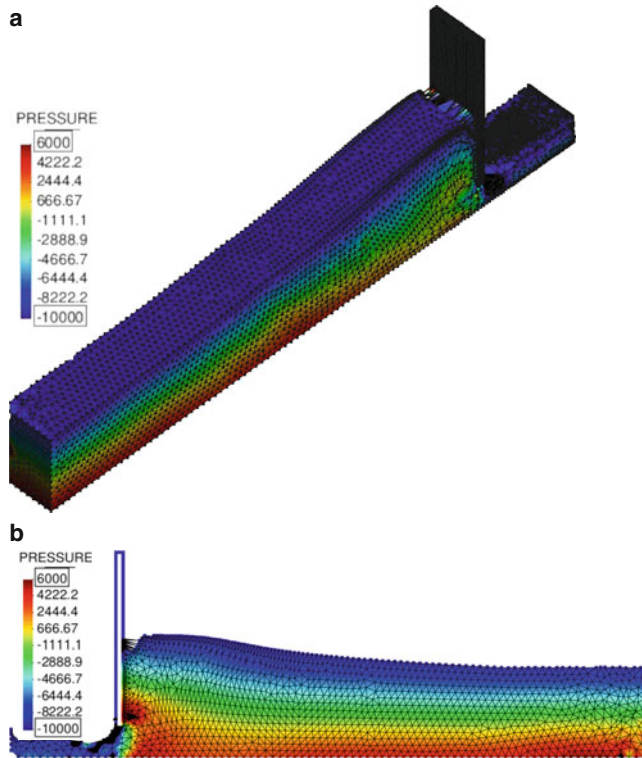


Fig. 3.9 **a** Three- and **b** two-dimensional spatial distributions of pore pressures (in [Pa]) in excavations performed on fully saturated loose sand ($e_0 = 0.79$) at a tool displacement of $S_x = 36$ cm

The topology of the ground free surface for a horizontal displacement of the tool of 36 cm, computed with both the 2D and 3D PFEM models, is analyzed (Fig. 3.11a). In general, slightly higher elevations of the free surface are observed in simulation results pertaining to dense sand (black solid line, blue dots), as compared to results involving loose sand. For loose sand, the 2D excavation model (red line) predicts a higher elevation of the ground free surface in comparison to its 3D counterpart (yellow dots). In the case of dense sand, the predicted curves remain close for the most part. Predictions obtained from the 2D and 3D PFEM models agree well. The computed evolution of tool reaction forces with respect to the horizontal displacement traveled by the tool, is assessed (Fig. 3.11b). Larger reaction forces are obtained for the tool-soil interaction carried out in the denser sand. For this set of simulations, the difference in the force levels between dense and loose sand is nearly sixfold at the end of the excavation process. For the selected soil parameters and tool displacement range, predictions from both versions of the excavation model, are in close agreement.

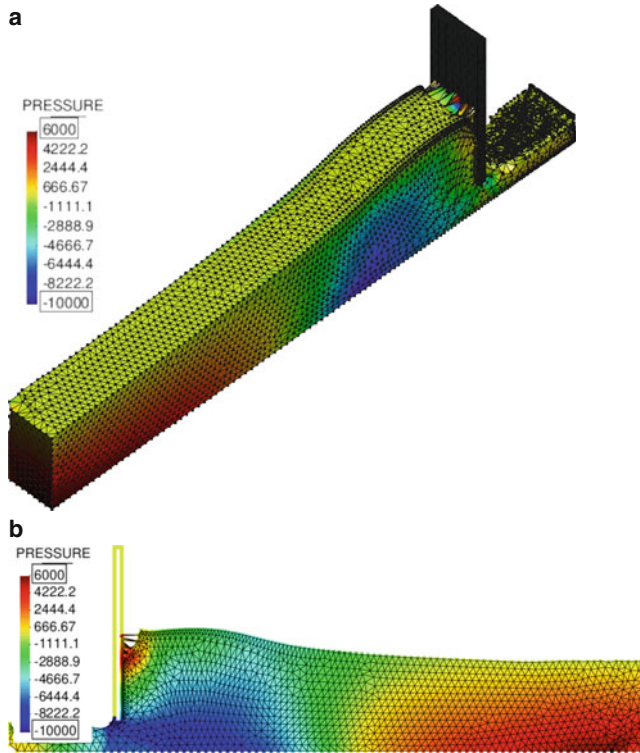


Fig. 3.10 **a** Three- and **b** two-dimensional spatial distributions of pore pressures (in [Pa]) in excavations performed fully saturated dense sand ($e_0 = 0.70$) at a tool displacement of $S_x = 36$ cm

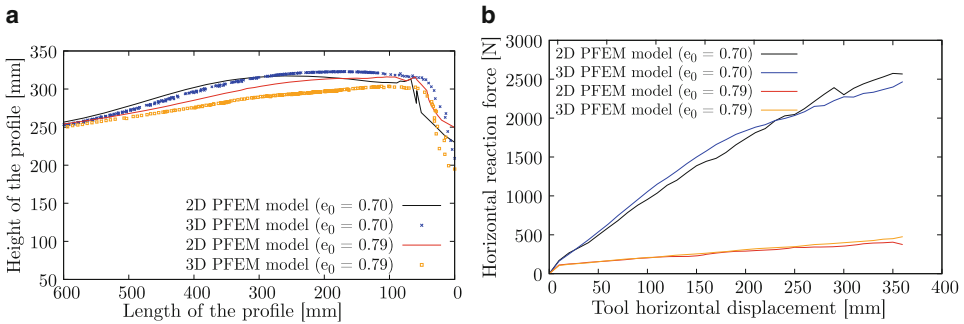


Fig. 3.11 **a** Computed free surface profiles of the ground for a tool horizontal displacement of $S_x = 36$ cm. **b** Reaction force-displacement curves computed during the tool-soil interactions performed with the 2D and 3D PFEM models, assuming dense and loose sands

3.2.2 Experimental and Simulation based Investigation of Rock Fragmentation

After briefly discussing the deformation characteristics of rocks, we present a suite of laboratory indentation test on a variety of intermediate-strength rock types. Finally, a peridynamic simulation model [13, 17] is presented that was used to simulate the indentation processes.

3.2.2.1 Deformation Characteristics of Rocks

Here, we briefly review the state of knowledge of the deformation characteristics of rocks focusing on aspects relevant for modeling purposes and intermediate-strength rocks. For modeling purposes, two questions are immanent: “How many parameter are needed to describe the deformation behavior? Where can the values of the relevant parameters be found?”. We address the first one below and regarding the second we refer to data collections in [3, 86]. For further reading, we suggest the compact overview [59] and the extensive treatments [41, 71].

Rocks are aggregates of minerals, naturally occurring, in most cases crystalline compounds of elements. The chemical composition of the most common rock-forming minerals is actually restricted to a limited number of elements, i.e., Si, O, Ca, Mg, Fe, Al, Na, K, and H. The abrasiveness, the extent to which rock fragments scratch a (metallic) tool, is controlled by the hardness of the minerals, well known for the common rock-forming minerals and classified by Mohs (relative) scale. In contrast, fracturing of rocks, the elementary step of excavation, is controlled by the structure formed by the minerals. Planning as well as substantial modeling of an excavation project obviously requires a quantitative description of deformation behavior.

Elastic deformation of rocks is probably of subordinate relevance for their excavation. Elastic strains resulting from removal of material, the creation of openings, will remain well below 1% in most cases, because elastic moduli of rocks range from a few to a few tens of Gigapascal [34]. Elastic in-situ parameters are constrained by surveys using elastic waves. However, such dynamic parameters often significantly exceed the relevant static parameters [29]. This discrepancy originates from rock-mass heterogeneity associated with fractures and faults that also causes a scale dependence of elastic parameters. The arrival of elastic waves reflects the fastest paths associated with the least damaged rock sections, while static parameters represent bulk behavior dominated by the weakest sections. Non-linearity and inelasticity even for modest stress perturbations associated with excavation (typically orders of magnitude smaller than Young’s moduli) are further consequences of the damage inventory.

As for any polycrystalline solid, the strength of rocks, i.e., a measure of the maximum stress they can bear in a specific loading configuration, depends on state variables, such as stress tensor components, temperature, and chemical milieu, and internal variables, such as grain size and porosity, including crack density. Under compression, the prevailing condition in the subsurface, geomaterials tend to fail on localized planes exhibiting obtuse

angles to the maximum principal (compressive) stress. This morphology and orientation relation led to address the failure planes as shear faults.

The presence of cracks and pores leads to the prominent dependence of compressive strength on mean stress. Failure of low porosity rocks in compression is accompanied by dilation, a relative increase in their volume, because failure results from nucleation, growth, and interaction of microfractures; therefore their strength increases with “confinement.” The higher the porosity is the more shear-enhanced compaction may occur, counterbalancing the dilation. Porous rocks may develop localized compaction bands normal to the largest principal stress or deform in a ductile manner by non-localized cataclastic flow [96] at sufficiently high confinement. Pore collapse can even be induced by isostatic loading owing to the stress concentrations on grain contacts.

The faster the loading the stronger the rock appears; however, the effect of loading rate on strength is irrelevant for most technical applications since a change of one order of magnitude in strength requires more than 10 orders of magnitude change in strain rate. An increase in temperature tends to weaken rocks. With the potential exception of some carbonate rocks, evaporates, and claystones, the reduction stays well below an order of magnitude as long as temperatures stay below about 300 °C, the current limit for engineering subsurface projects. The limited number of data on samples of significantly different size indicates a reduction on strength with increasing size that likely reflects a scaling between the size of pre-existing flaws and sample size. The presence of water tends to have a weakening effect; the identification of the underlying physical and chemical processes has proven difficult.

Before representing descriptions of the failure of rocks, it seems mandated to emphasize that the user of such relations (and associated empirical parameters) has to answer the question what is to be modeled. The immediate interaction of a cutting tool and a rock is probably dominated by the strength as determined on rock samples that are intact before the experiment, in the sense that pre-existing interfaces do not completely dissect them. In-situ, the pre-existing inventory (size, density) of discontinuities (joints, faults) affect failure progression and the fragment size. Studies on rock properties distinguish (intact) rock and rock mass (including mesoscopic structure, joints, faults).

Frictional strength poses a lower limit for the compressive strength of rock masses. Frictional strength of interfaces in rocks varies significantly with their roughness and the acting normal stress. Frictional sliding is associated with local wear of asperities and thus strongly depends on deformation history. When described by a conventional linear relation between shear stress and normal stress, Amonton’s law, the intercept, often addressed as cohesion, tends to increase with roughness. The slope, the coefficient of friction, converges to values between about 0.6 and 0.8 for many rocks, an empirical observation today known as Byerlee’s law or, probably more appropriately, rule [11].

In contrast to metals, rocks -not unlike concrete- exhibit a uniaxial compressive strength C that is about an order of magnitude larger than their tensile strength T [59]. The determination of tensile strength is technically cumbersome and thus such experiments are seldom performed. In contrast, measurements of the mode I fracture toughness

K_{Ic} , the resistance of a material against propagation of a single tensile fracture, are simple and thus often performed. From a fracture mechanical perspective, tensile strength obeys

$$T = K_{Ic} / \sqrt{\pi c_{ini}} \quad (3.1)$$

and thus constitutes a measure of the size of the pre-existing crack c_{ini} that leads to the macroscopic failure.

Fracture criteria of rocks, surfaces in the three-dimensional space of principal stresses, have been extensively investigated for more than half a century [71]. The commonly used linear Mohr-Coulomb criterion postulates that failure occurs on a plane, for which a critical shear stress

$$|\tau| = S + \mu_{int} \sigma_n \quad (3.2)$$

is reached, where S denotes an intrinsic shear strength and μ_{int} the coefficient of internal friction. The shear strength is related to the uniaxial compressive strength as $S = C / [2(\sqrt{1 + \mu_{int}^2} + \mu_{int})]$. Such a linear description is often acceptable for the limited range in normal stress relevant for technical applications. However, this formulation implies that the slope of the criterion μ_{int} and the orientation of the failure plane with respect to the least principal stress, β , are related by

$$\beta = \frac{\pi}{4} \pm \frac{\arctan \mu_{int}}{2}. \quad (3.3)$$

Experimental evidence does not support this assertion but documents an increase in the failure angle and a decrease in the coefficient of internal friction with increasing mean stress [59]. The non-linearity is reflected by the empirical Hoek-Brown criterion, in its most general form requiring the determination of three parameters [27]. Quite some effort has been spent on relating the parameters to rock-mass indices to allow for modeling of failure on the meter to decameter scale. Costamagna et al. [21] related failure to the Cardano condition for the existence of three real-valued eigenvalues of the characteristic equation of the stress tensor to arrive at linked friction and fracture criteria involving three parameters.

Murrell [67] extended the micromechanical Griffith concept of failure [37] to overall compressive stress states to arrive at a non-linear criterion with a single parameter,

$$\tau_{oct}^2 = 8T \sigma_{oct} = \frac{2}{3} C \sigma_{oct}, \quad (3.4)$$

where $\tau_{oct} = \sqrt{(\sigma_1 - \sigma_2)^2 + (\sigma_1 - \sigma_3)^2 + (\sigma_2 - \sigma_3)^2} / 3$ and $\sigma_{oct} = (\sigma_1 + \sigma_2 + \sigma_3) / 3$ denote octahedral shear and normal stress, the latter being identical to mean stress.

The second equality in Eq. 3.4 reflects the relation between tensile and uniaxial compressive strength $C = 12T$, inherent in the criterion, in good agreement with experimental

evidence. The fundamental criticism of fracture-mechanics based criteria as Eq. 3.4 addresses the notion that compressive failure is not caused by the propagation of a single critical defect. In contrast, compressive stresses eventually penalize growth [26] and the formation of the shear fault results from complex interaction and coalescence of multiple micro-cracks [58]. Subsequent fracture-mechanical treatments of compressive failure related the parameters of Mohr-Coulomb type linear criteria to the central parameters fracture toughness and initial crack length amended by a microscopic friction coefficient addressing the sliding of closed microfractures [5, 62, 89].

3.2.2.2 Laboratory Indentation Tests

Rock fragmentation in mechanized tunneling involves in general two basic processes: indentation and cutting (Fig. 3.1). In both processes, the fragmentation depends on the penetration depth of the used tool, though they differ in whether the tool travels normal (indentation) or parallel (cutting) to the rock surface. When penetration increases up to a critical depth, the rock behavior transits from non-localized deformation to localized deformation, i.e., fracturing, the latter of which is favorable for rock fragmentation. The simple, well-reproducible and accurate indentation test has long been utilized to measure different material properties, such as hardness [43], yield stress [91], and fracture toughness [85], though mostly for glasses and ceramics, and to assess rock properties, such as drillability and cuttability [90, 92]. The maximum indentation pressure p_{\max} is a pivotal parameter in interpretation of indentation tests; it represents the specific energy for removing a unit rock volume in cutting experiments with a Non-Truncated Tip Indenter (NTTI) [92].

The indentation process can be continuously monitored using advanced experimental techniques, such as electron scanning microscopy [54], digital image correlation [107], acoustic emission [19, 106], infrared thermography [57], and electronic speckle interferometry [19]. Numerical simulations, based, for example, on the discrete element method [40] and the finite element method [56], have also been performed. These experimental and numerical studies revealed that rock indentation involves several operating processes including volumetric compaction, plastic deformation, and macro fracturing.

Many simplified models have been proposed to explain the stresses and the deformation under indenters in brittle solids, perhaps most notably in glasses, among which is the cavity expansion model (CEM) [42, 51]. Ever since its transfer to rock, a frictional geo-material [19, 39], the model has gained popularity, but formulations were limited to the Non-Truncated Tip Indenter (NTTI). Such ideally sharp indenters suffer from severe wear due to the high stress concentration at their tips. The tool wear lowers the fragmentation efficiency as energy is invested in the deformation of the tools instead of in rock breakage, which motivates usage of cutting tools with truncated tips. The use of Truncated Tip Indenters (TTI) changes the failure mechanism; a phase of compressive failure below the flat indenter precedes the tensile splitting. Often, indentation tests conducted using a TTI were erroneously interpreted using relations developed for NTTI. The incorporation of tip truncation by [1] does not account for the ultimate fracturing. Recently, Yang et al.

[105] proposed a model based on the CEM for TTI that captures plastic deformation in compression and brittle tensile fracturing, and finite sample size. Here, we use the term “plastic” for macroscopically non-localized deformation irrespective of the deformation mechanisms on grain scale.

Mechanical and acoustic emission responses during indentation The investigations performed focused on intermediate-strength rocks, positioned between the two endmembers, soil and rock, either due to “weak” minerals (e.g., calcite, clays, halite) or “weak” structures (e.g., porous), because they pose particular problems regarding the “right” selection of excavation tools. We describe the general response of such intermediate-strength rocks to indentation using exemplary data from tests on a variety of sandstones, limestones, and tuffs with compressive strengths (UCS) from 11 to 140 MPa (Table 3.1). The damage progression and failure process was monitored during the indentation test using an acoustic-emission (AE) system (ASC Milne, Applied Seismology Consulting, UK). The uncertainty of locating AE hypocenters is around 8 ± 2 mm that is comparable to the size of the used AE sensors. Testing apparatus, procedures and specimen preparation are detailed in [105].

Typically, the force increases almost linearly to a distinct peak during the indentation process (Fig. 3.12); AE hypocenters gradually form a cluster beneath the indenter during the loading (Fig. 3.13). At the end of a test, the AE hypocenters trace the macroscopic fracture closely, indicating the validity of the AE technique for monitoring of the failure process. The indentation pressure typically exhibits a plateau-like maximum preceding the peak force, indicating that growth of the damage zone, where compressive failure conditions are reached, eventually proceeds at almost constant energy input until the tensile

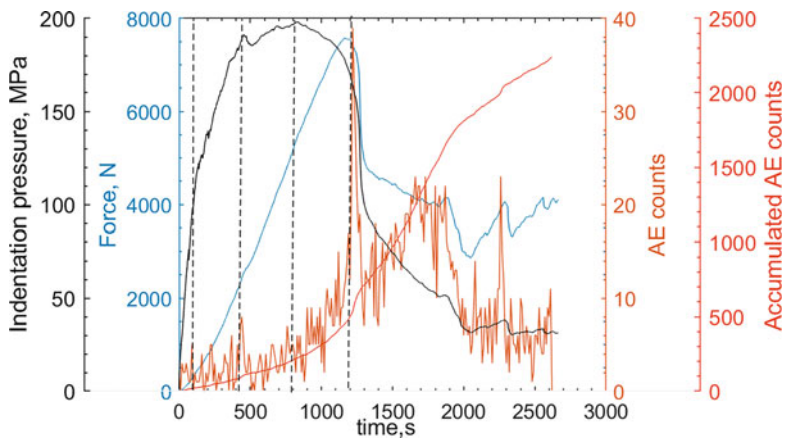


Fig. 3.12 Force, indentation pressure, number and total number of AE counts over an interval of 20 s as a function of time for a Gildehaus sandstone specimen of 84 mm diameter and 100 mm height. Tests performed in displacement control with a constant piston velocity of 0.05 mm/min

Table 3.1 Physical and strength parameters of eight rocks presented by mean values and their standard deviation, and the number of tested specimens in parentheses

Rock	Density kg/m ³	Porosity %	$v_{p,dry}$ km/s	$v_{s,dry}$ km/s	$v_{p,sat}$ km/s	$v_{s,sat}$ km/s	E GPa	Poisson's ratio	$K_{IC,dry}$ MN/m ^{1.5}	$K_{IC,sat}$ MN/m ^{1.5}	UCS MPa	ϕ °	ψ °	$p_{max,dry}$ MPa	$d_{max,dry}$ mm	$p_{max,sat}$ MPa	$d_{max,sat}$ mm
Anroechter sst (AS)	2468 ±5(3)	8.9 ±0.5(3)	4.93 ±0.07(3)	2.97 ±0.02(3)	4.99 ±0.13(3)	2.61 ±0.10(3)	38.2 ±0.1(2)	0.16 ±0.04(2)	1.36 ±0.08(3)	1.18 ±0.04(2)	140	33	35	513 ±57(4)	0.28 ±0.05(4)	499 ±183(3)	0.19 ±0.02(3)
Subbener sst (ST)	2087 ±32(3)	16.5 ±3.3(3)	3.22 ±0.07(3)	1.98 ±0.05(3)	3.74 ±0.05(3)	1.91 ±0.04(3)	18.9 ±2.9(2)	0.21 ±0.11(2)	0.53 ±0.03(6)	0.41 ±0.03(4)	30	33	30	370 ±72(4)	0.15 ±0.04(4)	316 ±31(3)	0.14 ±0.02(3)
Leistaedter sst (LS)	2116 ±55(3)	16.6 ±5.5(3)	2.68 ±0.09(3)	1.80 ±0.04(3)	2.90 ±0(1)	1.00 ±0(1)	11.4 ±0.4(2)	0.21 ±0.02(2)	0.25 ±0.02(3)	0.13 ±0.05(4)	15	44	21	185 ±52(4)	0.23 ±0.02(4)	113 ±50(3)	0.30 ±0.17(3)
Etringer Tuuff (ET)	1594 ±15(3)	27.0 ±1.5(3)	2.95 ±0.01(3)	1.64 ±0.01(3)	3.27 ±0.09(3)	1.58 ±0.03(3)	7.5 ±0.4(2)	0.43 ±0.05(2)	0.32 ±0.05(3)	16 ±0.14(2)	22	0	113	0.38 ±50(4)	125 ±0.38(4)	0.21 ±18(3)	±0.08(3)
Weiberner Tuuff (WT)	1396 ±10(3)	39.8 ±1.0(3)	2.52 ±0(3)	1.44 ±0.03(3)	2.39 ±0.01(3)	1.30 ±0.04(3)	4.0 ±0.9(2)	0.15 ±0.04(2)	0.25 ±0.02(3)	0.24 ±0.01(2)	11	n.d.	n.d.	71 ±4(4)	0.50 ±0.08(4)	48 ±9(3)	0.49 ±0.21(3)
Gauginger Tra- vertine (GT)	2203 ±31(3)	13.7 ±3.1(3)	4.93 ±0.11(3)	2.88 ±0.03(3)	5.18 ±0.14(3)	2.66 ±0.11(3)	28.5 ±1.7(2)	0.43 ±0(2)	0.84 ±0.14(3)	0.80 ±0.19(2)	50	n.d.	n.d.	486 ±159(4)	0.29 ±0.08(4)	534 ±162(3)	0.20 ±0.06(3)
Sellenberger shell limestone (SM)	2369 ±52(6)	9.0 ±5.2(6)	5.05 ±0.05(6)	2.77 ±0.03(6)	5.68 ±0.11(6)	2.65 ±0.01(6)	22.5 ±10.7(4)	0.44 ±0.01(4)	0.73 ±0.04(3)	0.48 ±0.03(2)	23	n.d.	n.d.	387 ±141(4)	0.16 ±0.03(4)	419 ±107(3)	0.14 ±0.06(3)
Gildehaus sst (GBS)	2010 ±20(18)	22.1 ±1.6(18)	2.56 ±0.06(34)	1.71 ±0.09(19)	3.20 ±0.09(15)	1.68 ±0.04(8)	9.5 ±1.2(3)	0.18 ±0.10(1)	0.30 ±0.03(9)	0.26 ±0.04(7)	57.0 ±4.5(3)	37	30	181 ±33(15)	0.58 ±0.22(15)	n.d.	n.d.

E : Young's Modulus; ϕ ($= \arctan(\mu_{im})$): internal friction angle, (see Eq. 3.2); ψ : Dilatation angle, i.e., parameter of non-associated flow rule; K_{IC} : Mode I fracture toughness determined from three-point bending tests on specimens of 10 mm diameter and 33 mm length; UCS: uniaxial compressive strength; p_{max} : peak indentation pressure determined from tests on specimens of 30 mm diameter and 50 mm height. Subscripts "dry" and "sat" indicate testing of dry or saturated specimens, respectively

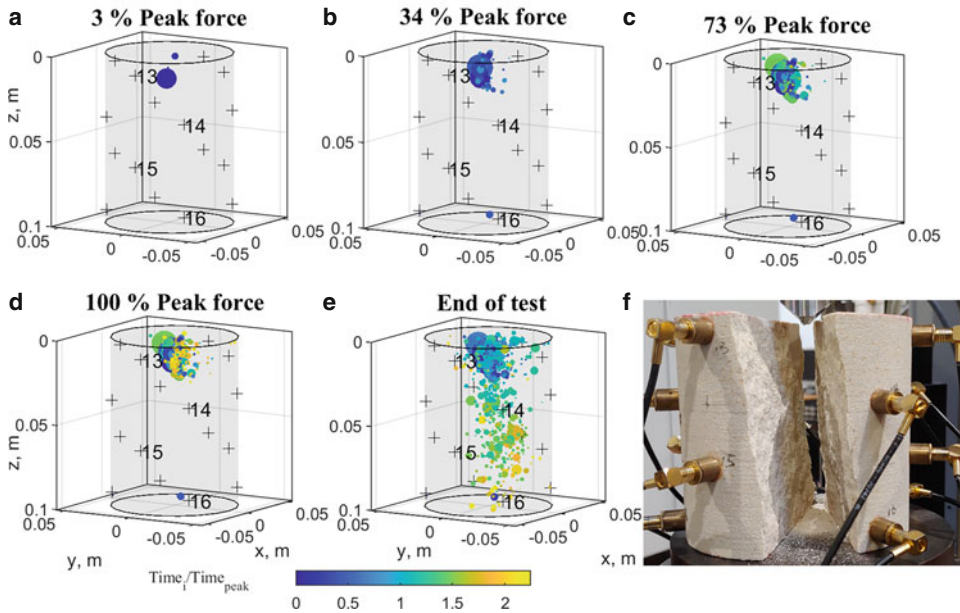


Fig. 3.13 Cumulative temporal-spatial distribution of AE hypocenters (circles) at different percentages of peak force (**a–d**) indicated in Fig. 3.12 by the vertical dashed lines, end of test (**e**) and photograph after indentation test (**f**). The marker size indicates the relative magnitude of AE energy. Crosses indicate sensor locations. The color bar indicates time relative to the one at peak force (with regard to [105])

tangential stress at the rim of this zone suffice to induce growth of a macroscopic tensile fracture that ultimately splits the specimen. When peak indentation pressure is surpassed, the cluster region representing the damage zone below the indenter does barely grow further (Fig. 3.13c, d), until growth of the macroscopic fracture becomes apparent.

The force-displacement curves for the “hard,” Anröchter Sandstone (AS in Table 3.1), with the highest uniaxial compressive strength (140 MPa) among the tested rocks, differ from that for the “weak” to “intermediate-strength” (uniaxial compressive stress less than about 80 MPa) rocks regarding the post-peak stage of indentation. For the intermediate-strength rocks, indentation beyond peak force is associated with a drop to a finite load that is then maintained for a displacement of several tenths of millimeters, during which the median crack propagates towards the bottom of the specimen. For the hard rock, brittle fracturing after peak force is more violent and typically results in coeval splitting of the sample and total loss of load bearing capacity.

Analysis of the results of indentation tests Analysis of the mechanical and acoustic-emission response indicates that the failure associated with rock indentation involves successively initial elastic deformation, punch-in of indenter into the specimen associated

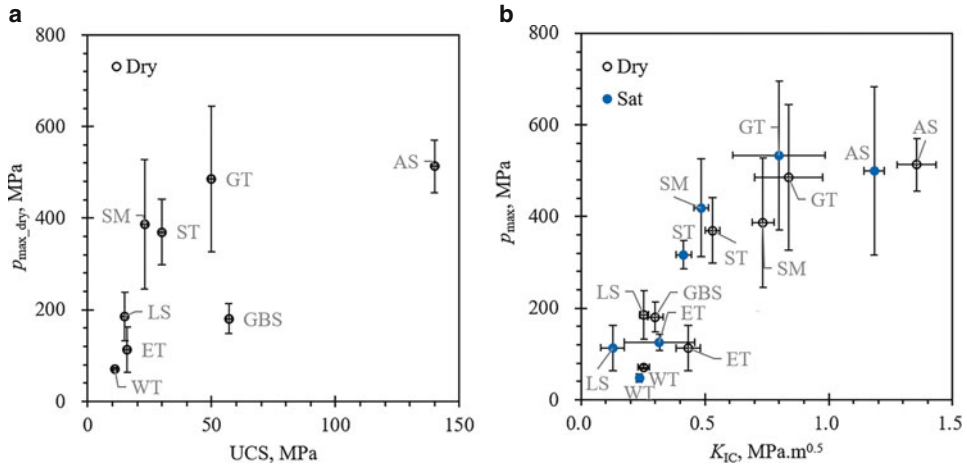


Fig. 3.14 Correlation between indentation characteristics and the two conventional strength parameters, uniaxial compressive strength (a) and fracture toughness (b). Uniaxial compressive strength (UCS) was only determined for dry samples. Indentation tests were not performed on saturated GBS samples. Error bars indicate standard deviations; a minimum of 3 tests were performed for each rock variety and saturation condition

with gradual formation of a crushed zone, formation of a damaged zone, and nucleation and growth of a macroscopic fracture that eventually splits the sample in half. We simplified sample failure due to indentation with a conceptual model as detailed in [105]. The model emphasizes the role of the peak-indentation pressure p_{\max} that indicates the resistance of the tested rock to compressive failure in the damage zone, e.g., described by the Mohr-Coulomb failure law (Eq. 3.2), that precedes the initiation of macroscopic tensile fracturing.

The experimentally observed maximum indentation pressures correlate with fracture toughness for the eight investigated rocks (Table 3.1). While saturation of samples with water systematically reduced toughness, the sample-to-sample variability is too large to identify an effect of saturation on maximum indentation pressure (Fig. 3.14a). The correlation between p_{\max} and uniaxial compressive strength (UCS) is also positive but the highly porous Gildehaus sandstone (GBS) seems to deviate from the general trend (Fig. 3.14b). The correlation of the maximum indentation pressure with the two strength parameters is consistent with our interpretation that it marks the transition from non-localized compressive failure in the damage zone to localized tensile fracturing at its boundary. The maximum indentation pressure increases with sample size, as evidenced by results for GBS specimens with a diameter from 30 mm to 84 mm.

For a specific rock variety, the sample-to-sample variability in maximum indentation pressure is not random, but we find an inverse correlation between p_{\max} and the associated penetration depth $d_{p_{\max}}$ (Fig. 3.15a). The pairs $(d_{p_{\max}}, p_{\max})$ do however show no systematic relation for the suite of rocks.

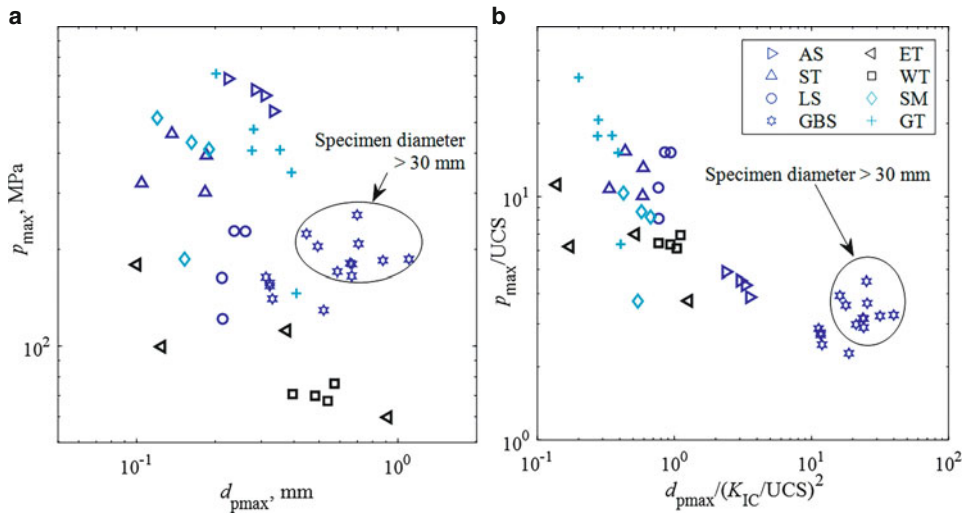


Fig. 3.15 Correlation between maximum indentation pressure and associated penetration depth in dimensional (a) and normalized form (b). Markers in blue, black and cyan indicate sandstone, tuff, and limestone, respectively. All but the encircled data points represent tests on samples with 30 mm diameter. The legend holds for (a) and (b)

To address material differences, the data is presented in normalized form, according to the theoretical analysis of [105]. Uniaxial compressive strength serves as a zero-order estimate of the stress corresponding to the yield conditions for the material in the damage zone, and we thus normalize maximum penetration pressure by it. The damage zone grows until its boundary reaches a pre-existing flaw, for which the tangential stress on the boundary corresponds to the critical stress concentration, the fracture toughness. For a given material, critical penetration depth and damage zone size correlate; damage zone size and the stresses in it—determined by compressive failure conditions—control the stress concentration on pre-existing flaws. The size of initial flaws scales approximately with $(K_{IC}/UCS)^2$ [5]; thus, we use this ratio to normalize critical penetration depth. As a result, there appears to be a general decreasing trend between the ratio of p_{max}/UCS and $d_{pmax}/(K_{IC}/UCS)^2$ (Fig. 3.15b); yet, some differences between the various tested rock types with compositional differences remain. A potential reason could be the material-dependence of the initial flaw-size relation beyond that accounted for by the two strength parameters. Furthermore, Zhu et al. [108] found that the initial-flaw size scaling involves a dependence on porosity beyond its effect on fracture toughness and uniaxial compressive strength.

3.2.2.3 Numerical Investigation of Rock Fragmentation

Simulation of rock excavation requires tools that can handle the discontinuities associated with fracturing leading to fragmentation. We developed a peridynamic model [87, 88]

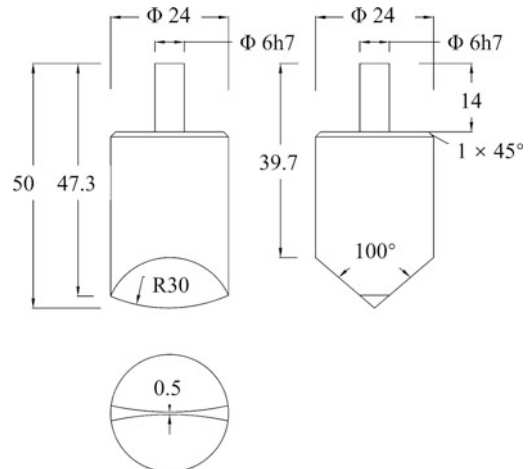
providing a natural way of incorporating discontinuities in the simulation domain. All peridynamic simulations were carried out using an extended version of the open source software *Peridigm* [55, 70]. The interested reader is referred to [14, 16] for further details on the simulation model.

We performed two sets of simulations with respect to the kinematics of the disc. Simulations of indentation tests (see Sect. 3.2.2.2 and [105]) were performed to provide insight into the formation of the crushed zone at the tool-rock interface and of tensile fractures emanating from that zone. Linear Cutting Machine (LCM) tests [79, 80] were treated to estimate the cutting forces required in the excavation process as a function of penetration depth. Besides homogeneous materials, we also considered mixed or heterogeneous ground conditions, situations where two or more types of rock or soil with significantly different mechanical properties are exposed at the tunnel face, to assess the variability of loads on the cutting discs and associated wear (see also Sect. 3.3.5).

These analyses are motivated by the characterization of the impulse load exerted on the cutting disc when it traverses a material interface, as this can cause excess vibration in the cutter head and increased fluctuations in torque and thrust of TBM. These peak loads also complicate the extraction of damage sensitive features based on the force oscillations.

Simulation of indentation tests Our simulations of indentation tests cover a total of six specimen sizes, with a combination of three diameters 30, 50 and 84 mm and two heights 50 and 100 mm. The truncated-tip indenter used is the same for all simulations (Fig. 3.16). For validating the current model, we use the experimental data from indentation tests on Gildehaus Sandstone reported in [105]. A qualitative validation relates to the formation of the crushed zone, from which tensile cracks initiate, while a quantitative validation rests on comparing the force-penetration data obtained from the experiments and the simulations.

Fig. 3.16 Indenter geometry used in [105] (dimensions are given in millimeter)



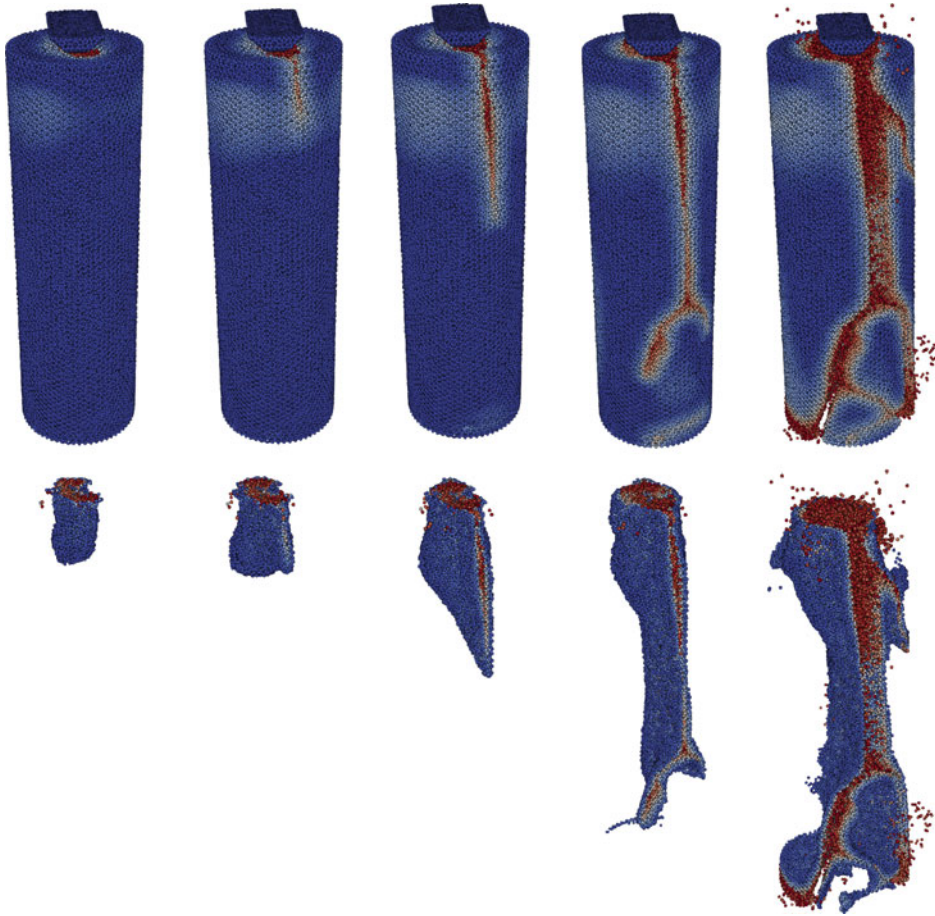
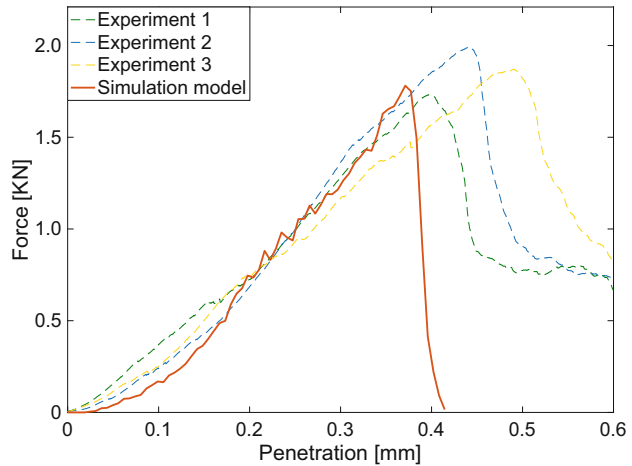


Fig. 3.17 Temporal evolution (left to right columns) of the fracture process during the indentation test (top row), the associated damaged and cracked regions are filtered out for visualization (bottom row)

The temporal evolution of fractures occurring due to the indentation load is presented in Fig. 3.17 for a specimen with 30 mm diameter and 100 mm height. The simulations capture the experimental observation of the successive formation of the crushed zone and the initiation of a central macroscopic tensile fracture splitting the sample in half. The interaction of the growing fracture with the sample's boundary leads to crack tip bifurcation [13, 15] and the crack branches. Finally, the specimen splits into two main and several small fragments. The loading stiffness as well as the peak load predicted by the simulation are in a good agreement with the experimental records (Fig. 3.18). However, the post-peak behavior differs slightly, which can be explained by the absence of damping in the simulations. As the main fracture starts propagating, the two large fragments move opposite to each other and separate faster than in the experiments, causing the indenter to

Fig. 3.18 Comparison of the force and penetration relationship measured in experiments and computed from the simulation model



loose contact with the rock as soon as the specimen splits and thus the force at the indenter goes to zero. The progressing fracture opening can be observed qualitatively by comparing the last two columns of Fig. 3.17.

Simulation of rock excavation with cutting discs At the level of a single cutting disc, interactions between the rock and the cutting disc can be characterized by the reaction force, which is decomposed into normal, rolling and side forces. These forces need to be estimated for an individual disc to predict the performance of a TBM, i.e., the global torque and thrust requirements. In the LCM test [35, 78] developed at the Colorado School of Mines (CSM) to predict the performance of a single cutting tool, the cutting disc moves along the rock specimen at a known penetration level and the reaction forces are measured at the cutting disc. We use this test as a benchmark for our analysis model.

We performed peridynamic simulations of the LCM test with a cutting disc of constant cross-section and a diameter of 432 mm for four levels of fixed tool penetration. The dimensions of the specimen are $0.4\text{ m} \times 0.4\text{ m} \times 0.15\text{ m}$ in the simulations and we ascribed properties of an elastic-brittle constitutive relation corresponding to Colorado red granite (Young's modulus 41.0 GPa, Poisson's ratio 0.234, uniaxial compressive strength 158 MPa, fracture energy 85.7 J/m^2). The simulation results obtained from the rock cutting with a tool penetration depth of 7 mm (Fig. 3.19a) show an evolving damaged zone beneath the cutting disc; the temporal evolution of rolling, normal and side forces (Fig. 3.19b) are examined from 0.1 to 0.3 m to avoid the influence of the specimen boundaries. The average normal forces obtained from the peridynamic simulations [14] agree well with the experimental data from LCM tests [35] (Fig. 3.19c).

Simulations of excavation with cutting discs in mixed ground The excavation process in mixed ground conditions is analyzed using a scaled-down cutting disc. The analyses

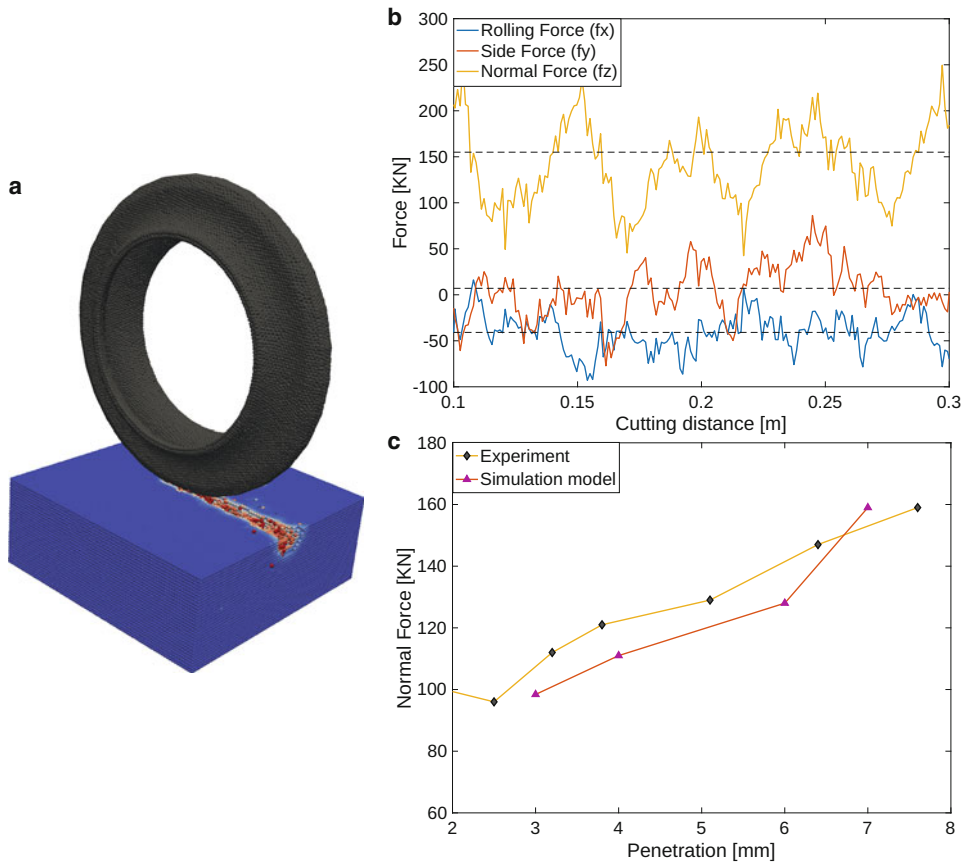


Fig. 3.19 Simulation of the LCM test showing the evolving fragmentation and crushing zone in the rock (a), evolution of cutting forces for a tool penetration of 7 mm (b) and average normal cutting forces for different tool penetrations compared against the results from the LCM experiment [35] (c)

consider a cutting disc moving from soft soil to hard rock medium. The soil material is modelled using an elastic-plastic constitutive relation and the rock material is modelled using an elastic-brittle constitutive relation. The soil's yield strength was 100 KPa and the rock's fracture energy $G_f = 23.7 \text{ J/m}^2$.

The simulated reaction forces at the cutting disc vary significantly with lateral displacement for the two penetration levels (Fig. 3.20b, d). The normal cutting forces are negligible (for the chosen yield strength) when the disc cutter is in the soil domain, but forces increase as it approaches the soil-rock interface (cutting length of 0.05 m) and when it thrusts through the rock domain. The peak in the cutting forces increases with an increase in tool penetration. Plastic deformations in the soil as well as the damage level in the rock also increase with increasing penetration levels (Fig. 3.20a, c).

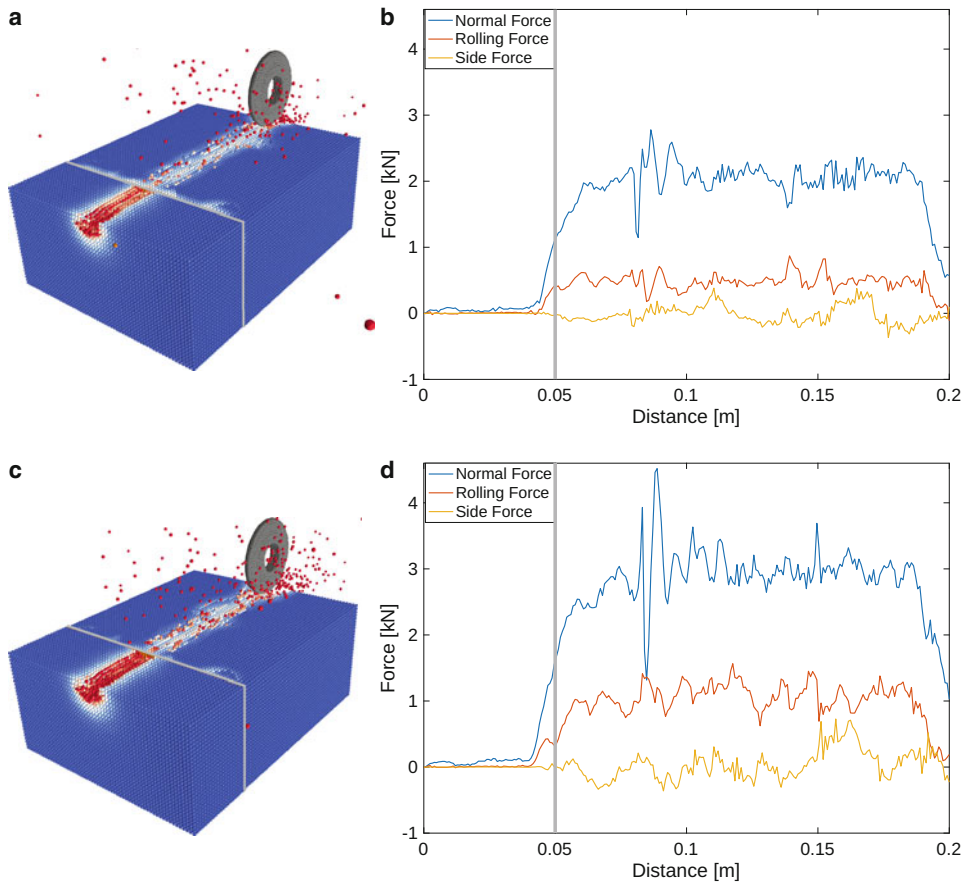


Fig. 3.20 Peridynamic simulation of a cutting disc working in mixed ground conditions (soft soil to hard rock domain) with a penetration of $p = 2$ mm and $p = 3$ mm. Plastic deformations and damage/fragmentation in hard rock is shown in **a** and **c** and the associated cutting forces acting on the disc are shown in **b** and **d**, respectively. (The vertical grey line represents the soil-rock interface)

3.2.3 Implications for Mechanized Tunneling and Outlook

Tool-soil interactions are a central component of mechanized tunneling excavations. The complexity of these interactions underlies the rapid evolution of the ground free surface and the development of large deformations, accompanied by the flow of the interstitial fluid in water-saturated soils. Laboratory tests performed on dry and water-saturated sand using a custom-made excavation device provided first-hand information regarding the topology of the material and the reaction forces generated on the tool during the excavation process. The presence of interstitial fluid and the development of shear bands strongly influences the reaction force-displacement curve. Presumably, this influence is associ-

ated with localized pore-pressure variations in the soil during the excavation. Numerical simulations of tool-soil interactions demonstrated that the proposed hypoplastic PFEM formulations were able to reproduce the main features of the mechanized excavation processes, including the soil deformations and the reaction forces on the tool. Furthermore, the presented models provided valuable insight into the spatial distribution of pore pressures in the ground and the effects of the initial density of the soil on the excavation process. Ongoing and future research concerning soil excavation include numerical simulations of mechanized excavations using an EPB cutting wheel model. Relevant boundary conditions, such as the required support pressure at the tunnel face, rotational speed and penetration rate of the wheel, will be considered. We will investigate the evolution of the torque generated at the wheel, the flow of excavated material at the face and the spatial distribution of pore pressures in the soil.

A crushed zone develops in rocks when the cutting discs installed on a rotating cutter head are hydraulically pressed against the tunnel face; as the disc continues to penetrate further, stresses around the crushed zone increase to the point that eventually macroscopic fractures are initiated. Fractures associated with neighboring discs coalesce leading to fragmentation and disintegration of the rock. Experimental investigation and analytical modeling of indentation tests identified the governing parameters for the involved mechanisms, non-localized damaging and localized brittle fracturing. The peak indentation pressure appears to indicate the transition from non-localized damaging below a truncated indenter to localized brittle fracturing, pre-requisite for the rock fragmentation that is aimed for in excavation procedures. Therefore, in practice, the tool has to exceed the penetration depth associated with the peak indentation pressure for efficient rock excavation. The corresponding thrust force may then be estimated through the established correlation between normalized peak indentation pressure and penetration. Thus, rock indentation tests performed in the laboratory provide relevant information on determination of operational parameters, such as thrust force and optimum penetration. In-situ, the rock fragmentation in mechanized tunneling is obviously complicated by many other factors, such as lithostatic stresses and the water-weakening effect, whose effects are poorly understood, and are therefore subject of ongoing research.

Numerical analyses performed using the framework of peridynamics theory have been proposed to predict the performance of a TBM in various scenarios. Results obtained from the indentation tests provided insight into the formation of the crushed zone from where the localized tensile fractures initiate leading to rock disintegration. Furthermore, the cutting forces obtained for a full-scale linear cutting test agree with the experimental recordings. Future work should account for different disc geometries, tool penetrations, tool spacings and cutting speeds. The cutting forces obtained from simulations of cutting discs moving from a soft ground domain to a strong rock layer yield a peak load at the soil-rock interface. The model was expanded to account for localized abrasive wear caused to the disc due to the cutting forces. Mechanized tunneling in mixed grounds results in highly variable loads on the cutting discs that may cause abnormal cutter wear leading to unexpected TBM stoppage.

3.3 Tool Wear in Mechanized Tunneling – Appearances, Mechanisms, and Countermeasures

Wear of tunneling tools causes downtimes of the TBM, both in a planned manner but more critically at unforeseen times if the wear rate of the tools exceeds preliminary wear predictions. It is crucial to understand the effective wear mechanisms that arise in the various geological conditions, to predict the rate of tool wear and its influence on the efficiency of the tunnel boring machine. Based on this assessment, the material concept for the tunneling tools can be adapted to minimize tool wear and reduce the risk of failure. This chapter illustrates the macroscopic appearance of the most important wear mechanisms, explains the underlying tribological micro-mechanisms, gives examples on how the wear behavior of materials can be measured, and points out possible improvements for material concepts.

Tools in tunneling are subject to high mechanical impact loads that are caused by boulders and retaining walls, and abrasive wear. Both cause damage to the tools, which must be replaced in the case of mechanical overload (breakage by brittle fracture) or when the wear limit of the tool is reached. These tool replacements result in downtimes, which reduce the economic viability of the tunneling project [47]. To minimize downtimes for tool replacements, a large number of wear forecast models were developed in the past, which are mainly based on simple abrasiveness parameters of the soil to be removed, semi-empirical equations, or empirical values [45, 49, 60]. With the help of these wear forecast models, optimal tool replacement times can be determined in advance, supporting logistical planning of the tunneling project. Unfortunately, there are sometimes large deviations between the estimated and the actual tool wear occurring during operation. The reason can be traced back to the complexity of the description of tool wear. Wear does not only depend on the abrasiveness of the soil to be excavated, the tool concepts used, or the machine parameters, but wear is a system variable. To understand how wear of tunneling tools can be counteracted efficiently, we follow a top-down approach. After the description of the macroscopically visible wear, the tribological system of tunneling tools is illustrated and tooling concepts that derive from the tribological system explained. Then, the micromechanisms of wear are investigated, and finally laboratory experiments and test-rigs for wear-prediction and wear-investigation are presented. A subdivision into soils and rocks is made to cope with the variety of grounds and therefore utilized tunneling tools,

3.3.1 Soils: Excavation, Tooling Concepts and Wear Appearances

Excavation of non-cohesive soils is mainly carried out by scraping the soil surface to detach the loosely bound soil particles (Fig. 3.24a). The commonly used tools for this purpose are chisels and rippers [36]. The wedged shape of the chisels causes a peeling process within the soil when the rotating TBM shield is pressed against the soil surface.

Table 3.2 Classification of material groups with applications in mechanized tunneling

Material Group	Application	Microstructure	Hardness
construction steels	welded constructions	Ferritic-Pearlitic	lowest
Q+T Steels	chisel substrates	tempered martensite	medium
tool steels	cutting discs	tempered martensite + 5–15% carbides	medium-high
metal matrix composites	wear protective layers	Ni-based metal matrix + 50% WSC	high
cemented carbides	cutting edges	70–95% WC in Co-based matrix	highest

After being detached from the soil-corpus, the loose particles drop into the feed section of a transport screw at the bottom of the TBM-shield and are transported away from the tunnel face. Based on this excavation mechanism, chisel tools experience mainly abrasive wear. Due to the tool's motion relative to the soil particles, the tool surface is frequently scratched by the abrasive particles. To counteract abrasion, tools are locally protected with wear protection elements, such as inserts of cemented carbides and hardfacings produced by a built-up welding technique [47]. However, the material response to abrasive wear differs for the wear-protective elements and the substrate (Table 3.2). The wear-protective elements, such as the cutting edge, inlays, and welded wear-protective layers, are worn evenly at a low and steady rate. In contrast, the substrate can experience uneven abrasive wear that may have an increasing wear rate over time. For example, suppose a wear protective element is lost due to missing support of a worn substrate. In that case, the wear rate at the place of the missing wear-protective element will increase drastically, compared to other areas of the tool, which still possess their wear-protective elements (Fig. 3.21).

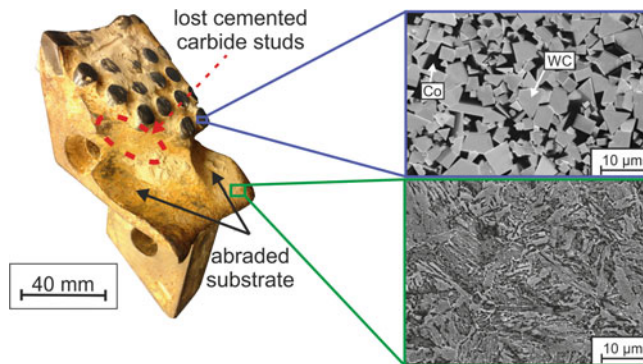


Fig. 3.21 Illustration of the graded build up of a chisel tool, consisting of a steel substrate and cemented carbide wear-protective elements

The abrasive attack on chisel tools is most pronounced at the cutting edge, which constantly encounters new soil layers and bears the highest cutting forces. Impacts, for example due to contact with large rock particle inclusions (e.g. pebbles) or layer interfaces, also act directly on the cutting edge; therefore, adequate toughness is necessary to avoid catastrophic fracture. The necessary combination of high resistance against abrasive wear and high fracture toughness renders the cutting edge the most demanding part of the tool. Cemented carbides of the type WC-Co have proven to be the only suitable group of materials, fulfilling the requirements for the cutting edge in practice. The microstructure of cemented carbides consists of 70-95 Ma% tungsten monocarbides WC , which are embedded in a cobalt-based binder phase [10].

To increase the fracture toughness, coarse grades with a Co-binder content of 15 Ma% or more are chosen for the cutting edge. At the same time, wear protective inserts on other places of the chisel tool may use a lower binder content to increase their wear resistance, as strong impact loads act less frequently on those parts. Other chisel parts, such as the backside, only experience wear due to excavated particles falling on them. In these cases, build-up welded wear-protective layers made of Ni-based metal matrices incorporating 30-50 Vol% Fused Tungsten Carbide (FTC) hard particles represent an easily applicable and cost effective solution to protect the steel substrate of the tool from abrasive wear. The substrate material forms the body of the tunneling tool and is the carrier of all functional elements, such as cutting edges and wear-protective elements. External forces acting on the tool are transmitted through these functional elements into the substrate, which must absorb and transmit the forces into the TBM superstructure. To avoid fracture because of mechanical overloads, the substrate has to be tough and must be able to dismantle critical stress peaks by means of small plastic deformations. Nevertheless, the substrate must also have the mechanical strength to bear the cutting forces during TBM operation and support the tool's functional elements. Quenched and tempered steels such as 42CrMo4 or 30CrNiMo8 are commonly employed as substrate materials for tunneling tools because of their high strength and sufficient toughness. A heat treatment of the forged base body enables the strength and toughness to be adapted to the needs in a wide range. Conventionally, quenched and tempered steels are hardened martensitically and tempered to a high degree to increase their toughness [9].

3.3.2 Rocks: Excavation, Tooling Concepts and Wear Appearances

Rocks cannot be excavated efficiently by scraping tools. Instead, cutting discs are used, which break down aggregates by induction of compressive stresses. The cutting discs roll over the rock surface in a circular path. Due to their direct contact with the rock and its fragments, cutting discs are exposed to abrasive wear, similar to chisel tools. However, their load collective is dominated by the high mechanical forces due to higher shear strength of rock compared to soil, as well as by a cyclic loading occurring upon repeated

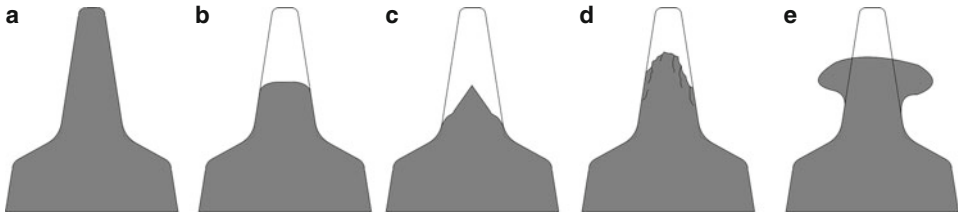


Fig. 3.22 Wear appearances on the cutting edge of cutting discs. **a** New cutting disc, **b** even abrasive wear, **c** flank wear, **d** surface fatigue, **e** plastic deformation

impact with the rock surface [47]. Therefore, cutting discs are typically not designed in a graded assembly of the substrate and dedicated wear-protection elements. Instead, the cutting disc is manufactured from forged tool steel with high strength and toughness and significantly higher hardness than the quenched and tempered steels used for substrates of chisel tools. In cases of extreme abrasive wear, cemented carbide studs may also be inserted into the cutting edge of cutting discs to increase the wear resistance.

The changes in geometry of the cutting edge during the use of the cutting disc depend on the activated wear mechanism (Fig. 3.22). Severe tapering of the edge as seen in Fig. 3.22c, for example, results from the different relative movements of soil particles to the cutting edge and the flanks of the cutting disc. While the contact of the cutting edge to the soil can be described as a rollover movement with ideally no relative movement, the flanks are in constant relative movement to soil particles. Especially the repeated movement of cutting discs in previously formed grooves can lead to flank wear.

Another form of uneven wear can be found on stuck or blocked cutting discs. If the cutting ring of the whole tool assembly is unable to rotate freely, one side is in constant contact with the soil and therefore worn out. This mechanism can occur especially in adhesive grounds or in case of a blocked roller bearing, for example, by infiltration of abrasive particles into the bearing assembly.

Surface fatigue mainly occurs on the surface of the wear-protective elements that are applied on tunneling tools. Worn tools show signs of spalling, as well as small cracks (Fig. 3.23).

The wear due to surface fatigue is concentrated to the parts of the tool that are regularly impacted by large abrasive particles. Due to the gradual sequence of the micro-processes of surface fatigue, the wear loss of the wear-protective elements can increase sharply after a particular time. Small fatigue cracks accumulate in the first stage of surface fatigue, but the actual wear loss only occurs in the last phase of spalling. Due to surface fatigue of the wear-protective elements, the soft substrate material underneath becomes exposed to the ground. As a result, the abrasive wear that has been prevented previously by the wear-protective elements increases and can lead to rapid unforeseen damage of the tunneling tools and even their support structures.

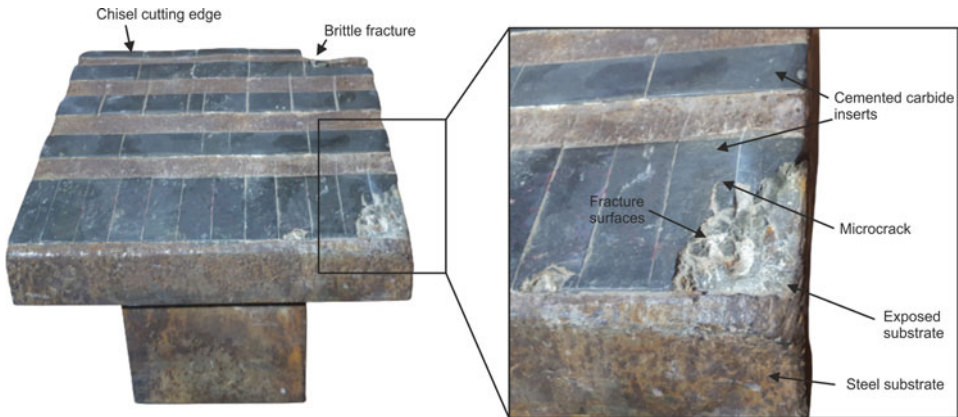


Fig. 3.23 Surface fatigue on the cemented carbide inserts of a chisel tool

3.3.3 Tool Wear Micromechanisms-Classification and Fundamental Concepts

The interaction of the tools with the ground can only be understood by developing a fundamental understanding of the tribological system. With this understanding, measures can be derived that improve the wear resistance of the tools and thus prolong their lifetime. The tribological system consists of the tool (base body), the wear-causing soil (counter body) and all other relevant variables such as the collective load (penetration, transferring forces), the surrounding medium (groundwater) and the intermediate medium (e.g. bentonite suspension) (Fig. 3.24) [23].

Four main wear mechanisms are distinguished, including abrasion caused by hard particles scratching the tool surface and surface disruption resulting from cyclical mechanical or impact stresses causing wear on TBM tools. Tribo-chemical reactions and adhesion have to be mentioned as well, however, they play a subordinate role in the wear damage to TBM tools. In reality, the main wear mechanisms overlap. For the derivation of suitable wear protection measures, the goal is to identify the dominant primary wear mechanism by developing a basic understanding of the tribological system. Because TBM tools are exposed to hard, abrasive particles and cyclical mechanical loads, both main wear mechanisms will be examined in more detail below. Once the dominant wear mechanism has been identified, it is essential to understand the interactions between the components in the material to be excavated and the individual structural components of the tool. With this knowledge, specific metallurgical measures can be derived that increase the tool life.

3.3.3.1 Abrasive Wear

Abrasive wear is the mass loss of a body due to scratching and/or grooving by a harder counter-body. In the case of mechanized tunneling, grains of quartz (SiO_2 , ca. 1100–

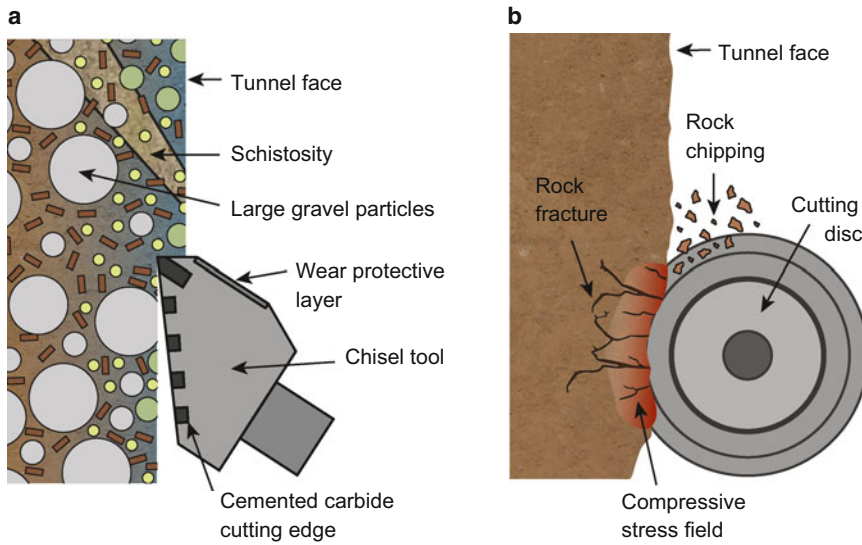


Fig. 3.24 Schematic illustration of the tribological system of **a** a chisel tool and **b** a disc cutter

1200HV0.05) [81], corundum (Al_2O_3 , ca. 2000–2200HV0.05), or other hard non-metallic compounds represent the counter-body; they are regarded as abrasive particles because their hardness exceeds the hardness of the steels (max. 900HV10) [10] used for the base construction of tunneling tools and the TBM itself, therefore causing abrasive wear.

Four distinct micro mechanisms of abrasive wear can be distinguished [33]: Micro ploughing, micro chipping, micro fatigue and micro cracking. Micro ploughing in its ideal form is not connected to mass loss, as the grooving of the base material by an abrasive particle is accomplished by severe plastic deformation to the sides of the formed groove. However, repeated ploughing of the material surface will lead to mass loss due to micro fatigue. Therefore, hardening mechanisms will embrittle the plastically deformed material and cause spalling at a future ploughing event. Micro chipping describes the removal of material in the form of a chip, which is ablated by an abrasive particle that scratches the surface of a body. Ideally, the volume of the chip matches the volume of the remaining groove. In a ledeburitic cold-work tool steel (Fig. 3.25b), the softer metal matrix is protected against abrasive wear by hard carbides. However, these reinforcement phases possess low fracture toughness due to their high hardness. Thus, ledeburitic cold work tool steels are susceptible to brittle failure induced by micro-breaking.

The dominant micro-mechanism of wear depends on the present tribological system. However, the main impact factors are the morphology and hardness of the abrasive particles, the hardness and microstructure of the scratched material, and the force and speed at which the abrasive particles interact with the abraded surface. The so called f_{ab} value helps to draw conclusions on the dominant micro-mechanism, integrating metallurgical

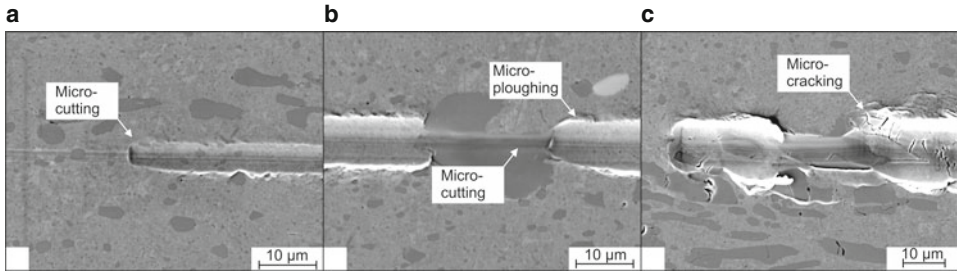


Fig. 3.25 **a** Micro cutting in a steel matrix, **b** micro ploughing of the steel matrix, **c** micro cracking of brittle carbides and the surrounding metal matrix due to severe plastic deformation

investigations and the characterization of the grooves resulting from the abrasive wear:

$$f_{ab} = \frac{A_g - A_s}{A_g}, \quad (3.5)$$

where A_s describes the volume of material displaced laterally through plastic deformation by micro-ploughing (positive value) or the volume removed laterally by the wear furrow through micro-breaking (negative value), and A_g represents the volume removed by an abrasive particle in a single scratch event. An f_{ab} value of 1 characterizes pure micro-chips, micro-breaking is preferably present in the case of $f_{ab} < 1$ and micro-ploughing in the case of $f_{ab} > 1$. The f_{ab} value describes abrasive wear between an abrasive particle and the constituents in the microstructure of the abrasively loaded material on the micro-scale. Deriving appropriate measures, micro-breaking can be counteracted, for example by increasing the material toughness. Otherwise, micro-ploughing can be reduced by increasing the hardness of the material. Thus a compromise has to be found for reducing the material removal due to wear because the material hardness and the toughness are inversely proportional to each other.

It is essential to understand that the cases of uneven wear presented in Sect. 3.3 are nevertheless based on the exact same micro-mechanisms, ploughing, chipping, cracking, and micro-fatigue, as evenly distributed abrasive wear and do not represent their own wear mechanisms. They are instead the result of certain parameter combinations in the tribological system.

3.3.3.2 Surface Fatigue

Surface fatigue is a wear mechanism, which is often insufficiently considered in the conceptualization of tooling and material concepts for mechanized tunneling. It is based on crack initiation and crack propagation at the tool surface due to cyclic mechanical loading. This type of loading occurs when the rotating tool hits larger soil particles such as rocks or gravel. However, also changing soil layers such as schistosity or slates, which cause a rapid change of the ground properties, can exert cyclic loading on the tunneling tools.

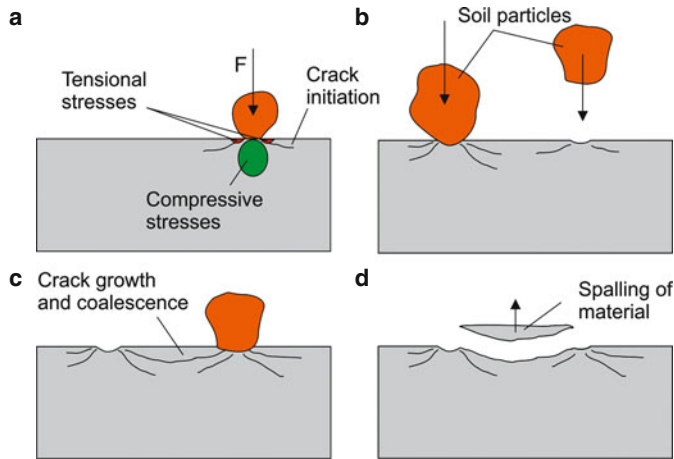


Fig. 3.26 **a** Stress distribution at the tool surface upon impact of soil particles and location of crack initiation, **b**, **c** repetitive impact of soil particles causes increase of the crack density and crack propagation, **d** material particles are spalled off the tool surface as cracks coalesce

Therefore, mixed grounds are especially capable of inducing cyclic loading, which has to be recognized and considered before choosing the tooling equipment. Surface fatigue must be distinguished from the micro fatigue mechanism of abrasive wear because surface fatigue requires no lateral movement of soil particles relative to the tunneling tool. Therefore, surface fatigue can also take place in hard rock excavation with cutting discs, which roll ideally over the rock surface whenever they get into contact. However, surface fatigue and abrasive wear often overlap to various extents, which hampers the determination of the dominant wear mechanism in practice. Awareness and understanding of the underlying wear mechanism are necessary to recognize the risks of wear due to surface fatigue and take appropriate action at an early stage. The wear mechanism surface fatigue can be subdivided into three stages crack initiation, crack propagation, and spalling (Fig. 3.26). Crack initiation can occur by either fracture or debonding of brittle phases, such as hard particles or non-metallic inclusions, inside the material when the forces of an external loading event cause internal stresses that exceed the strength of the brittle phase itself or its interfacial bonding strength, respectively. The loading event that causes the crack initiation does not have to exceed the tensile strength by itself; it instead acts as a trigger of residual stresses due to accumulated lattice defects around the brittle phase.

Crack initiation can take place after several loading events, which by itself do neither exceed the material strength nor its yield strength. In many cases, however, crack initiation is bypassed due to internal defects such as micro cracks or pores originating from the manufacturing process. The following stage of subcritical crack growth is characterized by an incremental extension of the crack, whenever external mechanical loading is applied. The material's microstructure has a crucial role in the interaction with the crack, which is

growing by dislocation movement processes at the crack tip. In particular, the morphology, distribution, and volume content of brittle, hard particles define the crack path inside the material, as the fracture or debonding of the hard particles consumes less crack energy than growth inside a tough metal matrix. The metal matrix controls the crack-velocity, as the crack growth rate mainly depends on the propagation velocity between the brittle hard phases. In the last stage of surface fatigue, small particles are spalled from the surface, causing the actual wear loss. This stage occurs when the subcritical-cracks have grown to a length that reduces the load-bearing cross section of the material to such an extent that it cannot withstand external mechanical loads. Alternatively, multiple micro-cracks from different starting positions join below the material surface, leading to the spalling of a particle enclosed by the cracks [48].

3.3.4 Tool Wear Tests

Wear tests are a fundamental component in the design process of material concepts for tunneling tools. Their purpose is to compare and to quantify the wear behavior of different materials. Wear tests should aim towards accurate representation of the tribological system in which the materials will be used to be meaningful and precise.

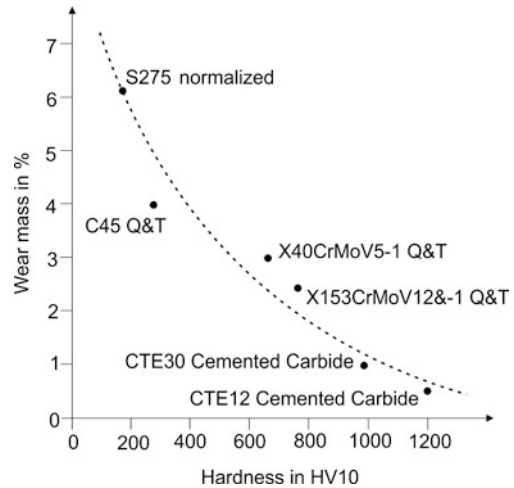
3.3.4.1 Tool Wear Tests for Abrasive Wear

Several standardized lab tests to measure soil abrasivity have been developed to predict the service life of tunneling tools in abrasive grounds (Table 3.3). Results of LCPC-tests and the Cerchar test can be found in several soil property reports of tunneling projects describing soil abrasivity. These tests are based on the abrasion of test specimens with a standardized indentation hardness (LCPC: 60–75 HRB; Cerchar: 550–630 HV). While these tests are user-friendly, they do not necessarily permit prediction of the wear rate in tunneling due to the simple classification of complex soils with index-values (e.g., 0 = extremely abrasive; 10 = not abrasive) tools for several reasons. First, the standardization of the test samples based on their indentation hardness is insufficient, as different materials with the same indentation hardness can have different wear rates in the same soil, as

Table 3.3 Overview of the most commonly employed abrasivity tests, as well as notable tunneling test-rigs for investigating wear on non-cohesive soils

Wear test	Specimen design	Rock grain size (mm)	
LCPC-Test	Metal-propeller	6.3	[95]
Cerchar Abrasivity Test	Metal-pin	Solid-body	[72]
ASTM-G65	Metal plate	0.6	[2]
Soft ground abrasion tester (SGAT)	Steel-propeller	10	[24]
Penn State Soil Abrasivity Test (PSAI)	Steel-propeller	7	[77]
RUB-Tunneling Device (RUB-TD)	Pins on Metal-propeller	4	[50]

Fig. 3.27 Wear loss of various steels and wear resistant materials correlated to their hardness



outlined on the example of the steels S275JR and C45 in soft-annealed condition, which both fulfill the hardness requirements of the LCPC-test but yield different wear rates when tested against the same abrasive (Fig. 3.27).

Reasons for the different wear resistance can be found in the microstructures of the steels, which both have a ferritic/pearlitic structure, but differ with regard to the size and distribution of the cementite lamellae of the pearlite and the overall pearlite content. The tempering steel C45 has a higher pearlite content than the construction steel S275JR, due to higher carbon content and more finely dispersed cementite lamellae [9]. The presence of the cementite lamellae (ca. 1100–1300 HV0.05) causes higher resistance against the grooving wear exerted by the abrasive particles in the LCPC-test, compared to the mostly ferritic microstructure of the steel S275JR.

Wear is a system property and has to be measured as such. Efforts have been made by several groups of researchers to recreate the tribological system of tunneling tools on a laboratory scale for wear testing (Table 3.3). The test rigs use a metal propeller, which rotates inside a conditioned soil sample, and acts as a carrier for wear specimens or the wear specimen itself. The wear-rate is determined by the mass-loss of the propeller, or the attached wear specimens. The TU Wien Abrasimeter [24], the SGAT, and the PSAI [77] have a vertical assembly of the rotating specimen in common, which is disadvantageous as it causes a time dependence of the wear test. The soil particles in contact with the rotating metal propeller are crushed over the course of the wear test, causing a steady decrease of the grain size and, therefore, a time-dependent change of the tribological system [46].

RUB-Tunneling Device The RUB-Tunneling Device was designed with the idea to create an accurate replication of the tribological system of tunneling tools. For the investigation of abrasive wear it uses a metal propeller, which acts as a carrier for up to 12 wear-pin specimens. The main difference to previously described test-rigs is the horizon-

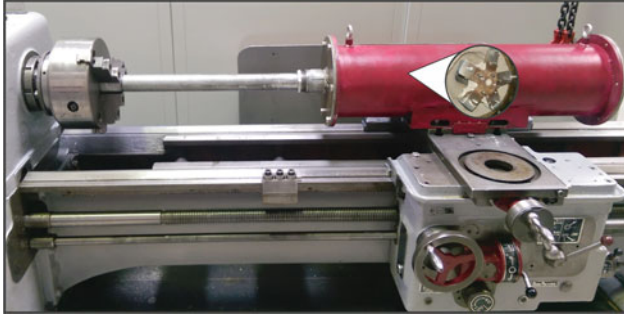


Fig. 3.28 Rub-Tunneling Device wear test-rig for experiments in non-cohesive soils

tal mounting of the metal propeller and a lateral movement of the soil-sample, relative to the wear-specimens. Both features are realized by the setup of the test-rig on a lathe, using the main spindle to rotate the metal propeller and the automatically driven support to move the soil-specimen (Fig. 3.28).

The wear-pins are constantly moved through fresh soil, which helps to keep the soil-properties as constant as possible over the whole test duration. Also, the replication of machine parameters such as penetration rate and rotational speed of the tools is possible. The soil-specimen can be conditioned with regard to grain-size, composition, and water-content before the experiment. In addition, further conditioning media such as bentonite suspension may be added through injection ports during the experiment. In the following, we present and discuss a selection of results that were obtained with the RUB-Tunneling Device.

Experiments on S275JR wear-pins show that the wear-rate increases with increasing penetration rate and is virtually independent from the rotational speed (Fig. 3.29a). This behavior can be explained with the increasing cutting forces, which are created at higher penetration rates due to a higher contact pressure between the tools and the soil. The increase of the cutting forces facilitates the indentation of abrasive particles into the material and therefore allows the formation of deeper wear scratches. A similar explanation applies to the observations made on the influence of the soil grain-size (Fig. 3.29b). Larger soil particles lead to a higher wear rate than small particles, as they create wider and deeper wear-grooves. In addition, coarse abrasive particles have the ability to extract small hard phases inside the tool material together with the surrounding matrix material. However, this effect does not apply to the steel S275JR that was tested in this study, as the material does not contain any hard phases.

Increasing non-uniformity of the soil causes an increase of wear (Fig. 3.29c), as the storage density of the soil can be increased when soil-particles with different sizes are present. Higher storage density leads to higher cutting forces, and therefore to increased wear. Dry soil has the lowest wear rate, as any presence of water increases the storage density of the soil and therefore increases the cutting forces (Fig. 3.29d). The peak of

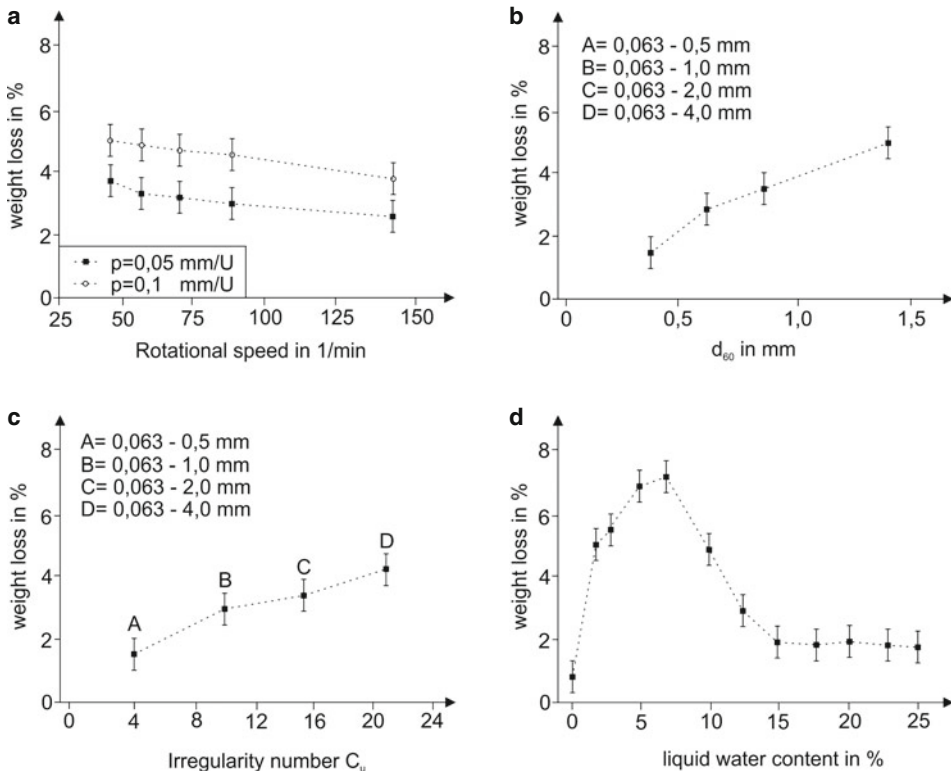


Fig. 3.29 Influence of the **a** rotational speed, **b** mean size of the abrasive particles, **c** irregularity number, **d** water content on the wear rate of S275 steel pins

the wear rate is found at a water content of 7.5%, followed by a decrease of the wear rate with higher water contents. The wear rate is highest when the pores between the soil particles are completely filled with water, leading to the maximum saturation of the soil, but simultaneously the water content is low enough to not significantly reduce the friction between the soil particles [50].

3.3.4.2 Tool Wear Tests for Surface Fatigue

Testing the resistance of materials against surface fatigue, requires to focus the attention on the underlying micromechanisms of subcritical crack propagation. Often, internal defects such as pores or microcracks originate already from the manufacturing processes. Therefore, the stage of crack initiation can be considered as completed and the service lifetime of a tool is mainly dependent on the crack propagation. We developed a test-setup for the lab-scale investigation of subcritical crack growth. It is based on the setup first presented by Jones et al. [44] and uses a spherical ceramic indenter that cyclically loads a flat specimen with a constant load and frequency [48]. Hertzian contact stresses due to

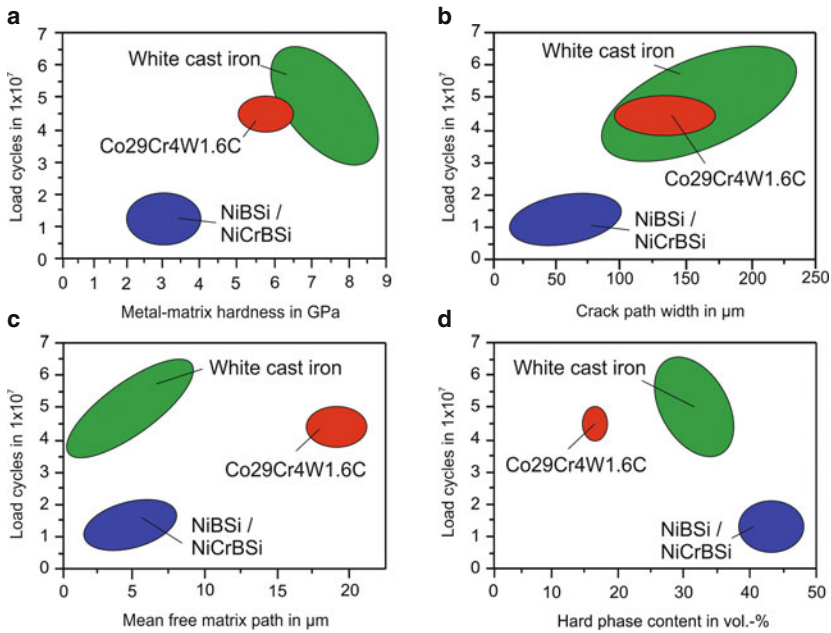


Fig. 3.30 Influence of the **a** metal matrix hardness, **b** mean width of the crack path, **c** mean free matrix length, **d** hard phase volume content on the fatigue life of various hard alloys (with regard to [12])

the cyclic loading cause the growth of a cylindrical crack around the contact area between the indenter and specimen [30]. As surface fatigue mainly occurs at the hard but brittle wear protective layers of the tunneling tools, these materials were the focus of attention.

Investigations on cemented carbides and several hard alloys on Fe, Ni, and Co-basis showed that the material's resistance against subcritical crack propagation depends on the content and morphology of metal matrix and hard phases, as well as on the mechanical properties of the respective phases (Fig. 3.30) [12]. In general, the metal matrix controls the crack propagation velocity due to its high toughness compared to the hard phases. High contents of the metal matrix and a microstructure with large metal matrix cells, creating large distances between adjacent hard phases are therefore beneficial to the crack propagation resistance. For the same reason, large hard phase sizes lead to a high crack propagation resistance, if materials with the same hard phase content but with different hard phase sizes are compared. In terms of mechanical properties, the strength of the individual microstructure constituents mainly determines the crack propagation resistance. As the subcritical crack propagation in the metal matrix originates from the gliding behavior of dislocations, strengthening of the metal matrix inhibits this mechanism and is therefore an effective method to increase the crack propagation resistance. Our investigations showed that martensitically hardened Fe-based metal matrices offer the highest

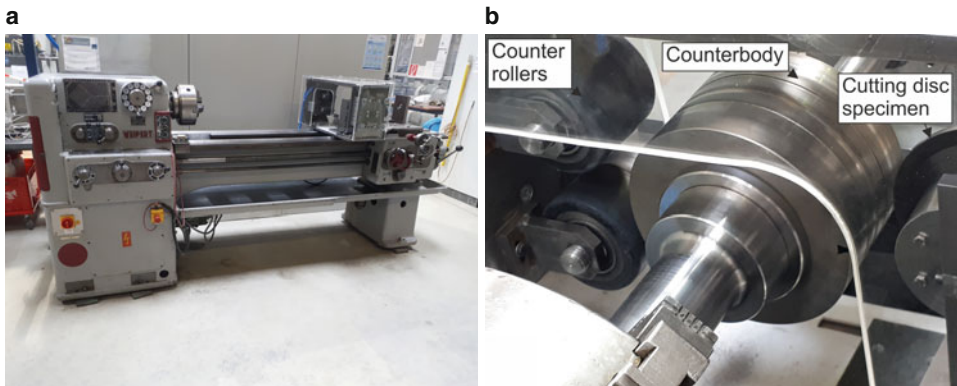


Fig. 3.31 Setup of the RUB-Tunneling device for testing the behavior of cutting discs under cyclic loading. **a** Overview of the test rig without built in counterbody, **b** close-up of the relative position of counterbody and cutting disc specimen

strength, followed by Co-based alloys. The Ni-based alloys that are commonly used for build-up welding have a weak metal matrix and therefore a low resistance against crack propagation. Cutting discs represent the second group of tools that is affected by surface fatigue. The RUB-Tunneling device wear-test rig was modified to accommodate miniature specimens of cutting discs (Fig. 3.31).

The specimens are pneumatically pressed against a counterbody, either made of rock or tool-steel, which is rotated by the main spindle of the lathe. Load cells in horizontal and vertical position enable measuring of the cutting forces, depending on the applied contact pressure, as well as on the rotational speed and type of the counterbody. To test the response of different tool-steels to cyclic loading, the cutting disc specimens roll over a metal counterbody with a weld seam, which exerts an impulse on the specimen on each rotation.

The tests were conducted over a duration of three hours (10,000 load cycles) with rotational speeds and estimated contact pressures that match the conditions reported from real tunneling projects. The strength of the metal matrix and the included hard phases have a significant impact on the behavior of the steels under cyclic loading; cracks are initiated at the surface of the cutting edge in most of the investigated steels and grow into the material (Fig. 3.32). Low metal matrix strength leads to severe plastic deformation of the cutting edge and fast crack initiation, due to facilitated mobility of dislocations. Large hard phases on the other hand act as barriers to the plastic deformation of the surrounding metal matrix, but the accumulated stresses at the matrix/hard phase boundary can lead to brittle fracture, as soon as the strength of the hard phase is surpassed. Therefore, sudden crack initiation and propagation are possible.

To gain more information about the high cycle fatigue behavior of the investigated steels, SN-curves were determined by the means of rotational bending tests (Fig. 3.33).

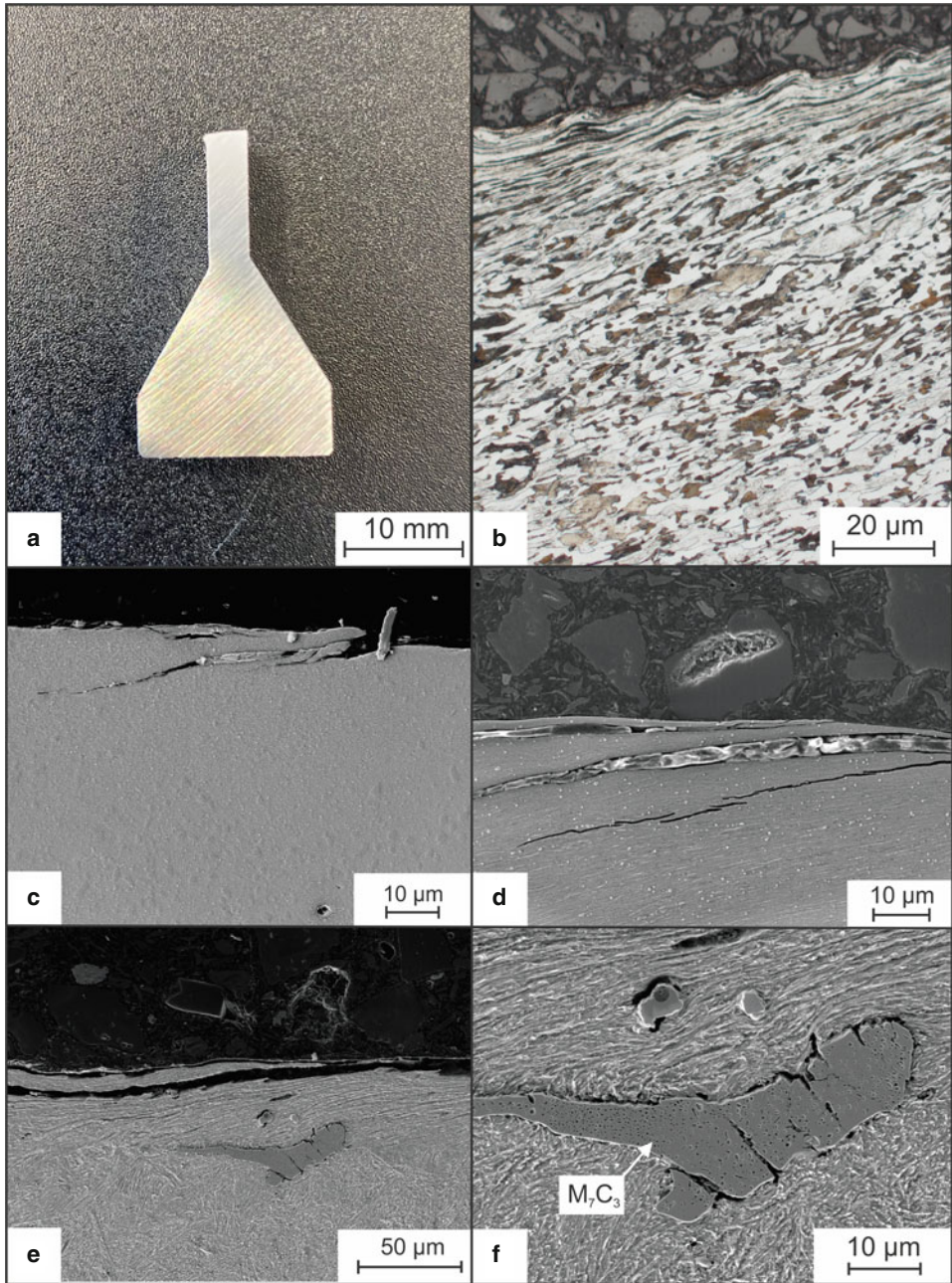


Fig. 3.32 **a** Cross section of a worn laboratory scale cutting disc, **b** cutting edge of construction steel S355, **c** cutting edge of cold work tool steel 90MnCrV8, **d** cutting edge of hot work tool steel X40CrMoV5-1, **e** cutting edge of cold work tool steel X153CrMoV12-1, **f** large carbides inhibit plastic deformation, due to their high Young's modulus and low plastic deformability

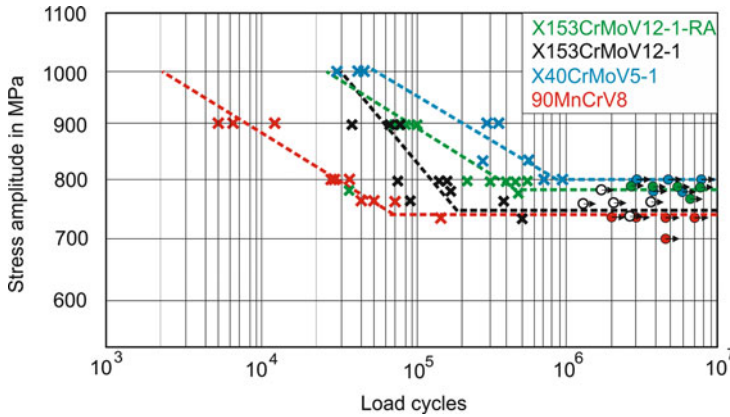


Fig. 3.33 Fatigue test results of different tool steels, obtained by rotary bending tests

The results indicate that the fatigue strength of carbide-rich cold work tool steels, such as X153CrMoV12-1, is lower compared to hot-work tool steels as X40CrMoV5-1, which contain no large eutectic carbides. However, by reconfiguring the heat-treatment, a content of about 10 vol% retained austenite could be implemented in the microstructure of the X153CrMoV12-1 steel. This led to an increase of the fatigue strength, due to stress induced transformation of the retained austenite and the subsequent formation of compressive residual stresses. A cold work tool steel with low carbon content that was also tested showed the worst fatigue properties. This behavior could be traced back to predominantly intergranular fracture of the grain boundaries, resulting in a brittle fracture behavior and low energy dissipation during crack propagation.

3.3.5 Abrasive Wear Modeling

Wear is related to sliding contact and abrasive wear occurs when a surface containing hard particles slides on another softer surface. The sliding causes the hard particles to dig into the softer surface and as the sliding motion continues, grooves are formed on the soft surface from where the material is removed. The volume lost due to abrasive wear can be quantified by considering the normal force between the two surfaces F_N , the abrasive wear coefficient k_{abr} , which depends on the average roughness of a surface, the hardness of the material to be abraded H , and the distance of sliding x in an *Archard* type wear model V_{wear} [4],

$$V_{wear} = k_{abr} \frac{F_N x}{H}. \quad (3.6)$$

The simulation model is verified using a sliding test for the abrasive wear. A steel block is resting under its body weight on a rock surface, it then slides on the rock specimen for

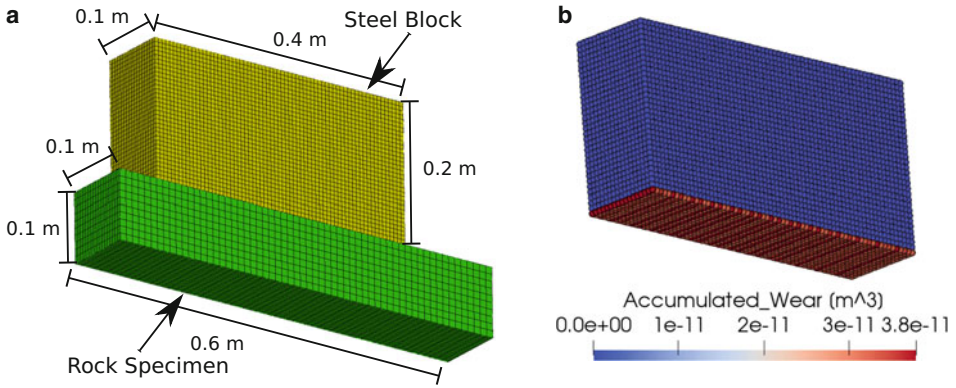
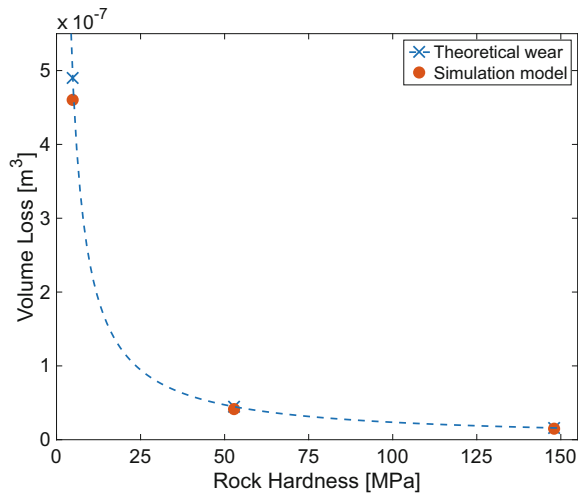


Fig. 3.34 Simulation setup and geometry of the steel and rock specimen for the wear test (a). Accumulated wear on the steel specimen surface after a sliding distance of 6.4 cm on Fell sandstone (b)

Fig. 3.35 Comparison of the theoretical total volume lost to abrasive wear with the peridynamic simulation model with respect to varying hardness of the rock surface



a known distance of 6.4 cm, as shown in Fig. 3.34a. The test is performed for three types of rocks with different hardness values: Sherwood sandstone ($H = 4.8 \times 10^6$ Pa), Fell sandstone ($H = 5.28 \times 10^7$ Pa) and Dealbeattie granite ($H = 1.48 \times 10^8$ Pa). Accumulated volume lost due to abrasive wear from Fell sandstone on the steel surface, computed using the peridynamic simulation model, is shown in Fig. 3.34b. Volume lost due to abrasive wear computed from the simulation model using rocks of varying hardness is compared with the theoretical values obtained from Eq. 3.6 in Fig. 3.35.

The verified model for abrasive wear can now be used to compute the volume lost on the cutting tools due to abrasion. The simulations performed for the LCM test in mixed ground conditions (Sect. 3.2.2.3) are used to investigate the abrasive wear on the cutting discs for two different penetration levels; $p = 2$ mm and $p = 4$ mm. Figure 3.36a shows the accumulated wear on the cutting disc at three stages, i.e. in the soil domain (left column),

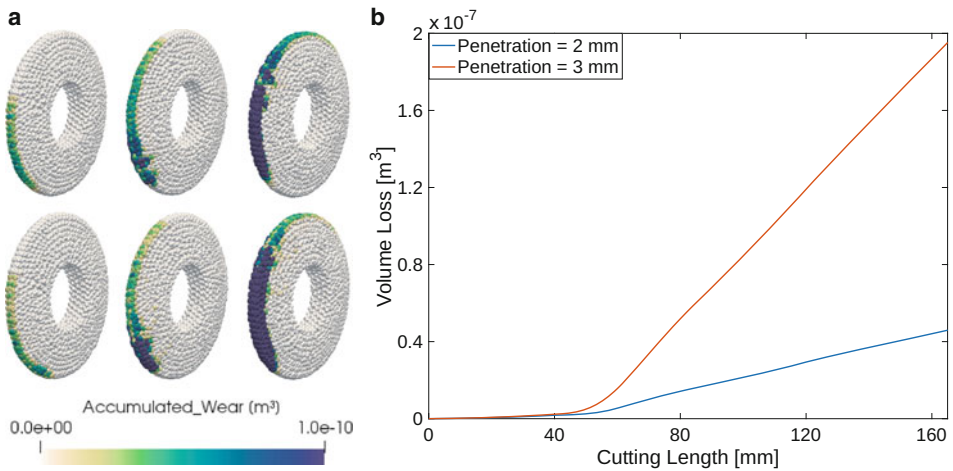


Fig. 3.36 Comparison of the abrasive wear on the cutting disc working in mixed ground conditions (Fig. 3.20) at two different penetration levels; $p = 2$ mm top row and $p = 3$ mm bottom row of **a**). Total volume lost on cutting disc due to abrasive wear over cutting length (**b**)

at the soil-rock interface (middle column) and in the rock domain (right column). It can be seen that the accumulated wear on the cutting disc increases significantly as the disc continues to move into the rock domain. Total volume lost due to abrasive wear at the cutting disc is plotted over the cutting length for both penetration levels in Fig. 3.36b.

3.3.6 Simulation of Abrasive Tool Wear on the Mesoscale

The interaction between tunneling tools and soil or rock causes abrasive wear in the tunneling process. Many different methods have been already used to describe the abrasive behavior of sand and rock, such as laboratory tests, field tests, and numerical simulations. The application of numerical analysis improves the design methodology and allows to achieve a more optimized shape for cutting tools. Numerical methods can be used to simulate the interaction between machine components and the ground. We introduce an efficient wear model for estimating the abrasive wear rate caused by a mixture of particles. Such a model can help the engineer to understand the wear mechanisms better, to determine the reasons for the cutting tool failure, and consequently to optimize the design of the tool components. The goal is to reduce the number of required laboratory tests in the design procedure of the TBMs, and thus to save costs.

Our wear model is based on the idea of extrapolating the behavior of a scratch caused by a single abrasive particle to the total wear rate of the particle mixture, employing relations resulting from 3D particle simulations. This objective is reached in two steps: in the first step, a single scratch test is modeled to investigate the cross-sectional geometry

of the resulting groove and to understand the dominant wear mechanism. In the second step, the results of single scratch tests are extended to the wear of the mixture by means of equations for the number of contact particles and normal contact forces obtained from particle simulations. Numerical methods used for these procedures are the Finite Element Method (FEM) for simulation of single scratch test and Distinct Element Method (DEM) for modeling of particle mixture. These steps are explained in detail in the following subsections.

3.3.6.1 Single Scratch Test

Abrasion can be numerically reproduced in a controlled way by simulating a single asperity scratch test where a pin or a conical indenter penetrates the surface of the specimen and slides over it. Scratch damage ranges from plastic grooving in ductile material to cracking and chipping in brittle material. The scratched surface is a result of the active micro-mechanisms of abrasion, namely, plowing, wedging, and cutting (see also Sect. 3.3).

A three-dimensional scratch process is modeled and simulated using a coupled damage-plasticity material model, implemented as a user subroutine (UMAT) in the finite element code Abaqus. The model consists of a rigid tip with a predefined radius and a flat deformable specimen (see Fig. 3.37). The specimen is fixed, and the tip slides over the surface in such a manner that a groove forms. The width and length of the specimen should be large enough to eliminate boundary effects. In the simulations, a displacement-controlled loading was applied in two steps:

- In the indentation step, a vertical displacement along the thickness of the specimen is applied to press the indenter down until it reaches the specified indentation depth.
- In the scratching step, a horizontal displacement is applied to slide the indenter in the z -direction at the constant indentation depth prescribed by the indentation step.

The contact area and the reaction forces were recorded during the process. The material properties of quartz (SiO_2), which is much harder than the steel of the specimen, are assigned to the tip. As a result, the tip does not wear during the scratching movement,

Fig. 3.37 Schematic representation of the scratch test in the initial undeformed configuration

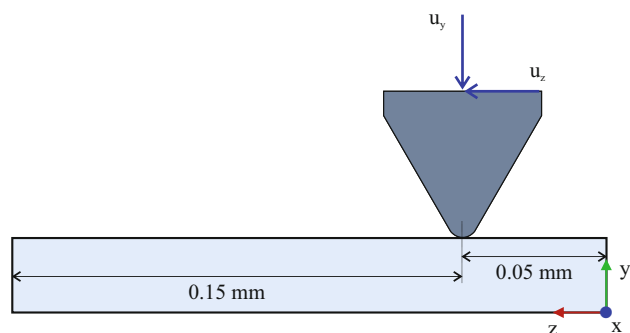


Table 3.4 Mechanical properties of the tested materials

Material	Quartz (SiO ₂)	Steel (1.0570)
Young's modulus (GPa)	73	210
Poisson's ratio	0.17	0.33
Density (kg/m ³)	2200	7800
Hardness (GPa)	9.8	2

and can be considered rigid. We selected material properties of standard steel DIN 1.0570 *AISI1024*, which is commonly used in machine components, for the specimen to be scratched. Table 3.4 lists the mechanical properties of quartz and the steel used in the model.

The initial model for the tip and the specimen used in the numerical simulations with their discretization are depicted in Fig. 3.38. A very fine mesh or a uniform fine mesh for the specimen will drastically increase the computation time, especially in the three-dimensional models. However, a coarse mesh is not sufficient to capture the plastic deformation and the localization of damage. Therefore, we employed mesh refinement around the scratching zone to reduce the number of elements and consequently speed up the simulations and at the same time obtain sufficiently accurate results.

The single asperity test was performed for an indentation depth of 0.002 mm. A total sliding distance of 0.1 mm was realized by the tangential movement of the tip. An illustration of the simulation results with groove is depicted in Fig. 3.39. The influence of the abrasive particle size on the wear volume is typically studied for abrasive particles up to around 100 μm . Hence, the simulations were performed for three tip radii of 25, 50, and 100 μm with the cone angle of 60° (see Fig. 3.40). In these simulations, the indentation depth is constant and equal to 0.003 mm.

The smaller the tip radius is, the lower shoulders of the groove are obtained, and consequently more wear is caused (Fig. 3.41). Thus, the wear volume increases with decreasing tip size for constant indentation depth. In addition, the employed coupled

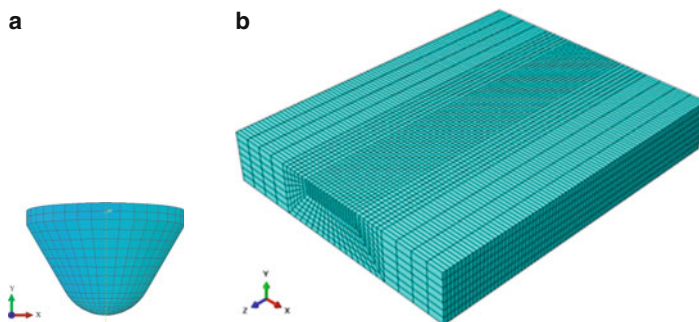


Fig. 3.38 **a** Spherical tip with a radius of $R = 50 \mu\text{m}$, **b** mesh for the specimen used in the numerical simulations

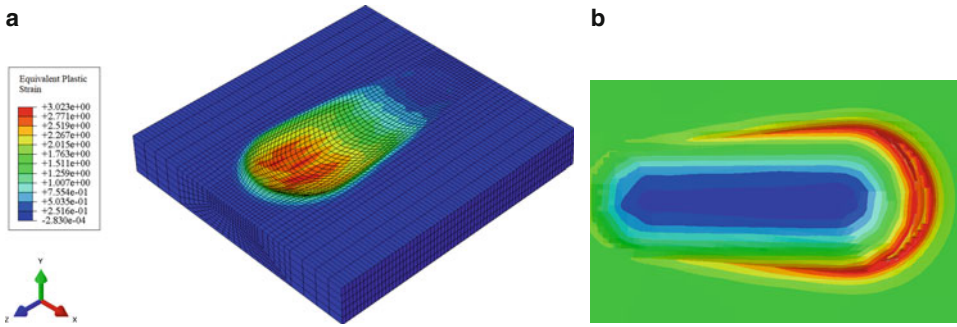


Fig. 3.39 A groove resulting from a single scratch test for $d = 0.002$ mm and $R = 50$ μ m. **a** Distribution of equivalent plastic strain in 3D view and **b** result of a microscopic height profile measurement (blue is low and red is high)

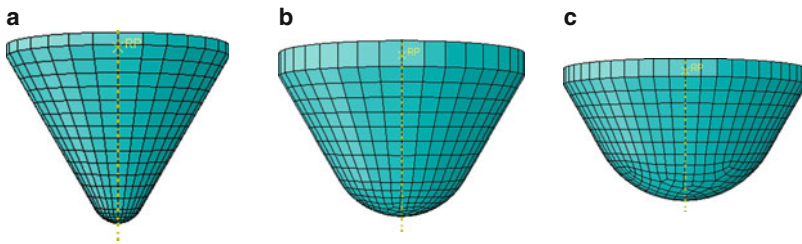


Fig. 3.40 Representation of the tips used in the simulations. **a** $R = 25$ μ m, **b** $R = 50$ μ m and **c** $R = 100$ μ m

damage-plasticity model accounts for the damage induced on the specimen, which results in the volume loss of the surface. In experiments, the particle size effect is studied using a grid of particles or tips. For a grid of particles under constant pressure, the force per particle has a direct relation with its radius. Because the number of particles per unit area decreases for larger particles, it results in a larger amount of wear caused by every single particle. The cross-sectional geometry of the groove caused by a tip with a radius of 100 μ m reveals a completely plastic deformation with large shoulders and no material removal. In contrast, for the scratch cross-section built by the tip with a radius of 25 μ m almost no shoulders are observable, and a large wear volume is recorded. This effect is discussed in the following Sect. 3.3.6.2, where a grid of particles is simulated using DEM.

3.3.6.2 Total Abrasive Wear of a Mixture

Particle simulations permit extension of the prediction of abrasiveness of individual particles to the actual ground consisting of abrasive particles with different sizes and shapes. The simulation of a mixture of particles was performed using the distinct element method in PFC^{3D} software. The abrasive particles were simulated as quartz grains, as quartz is one of the most abrasive minerals in common soils.

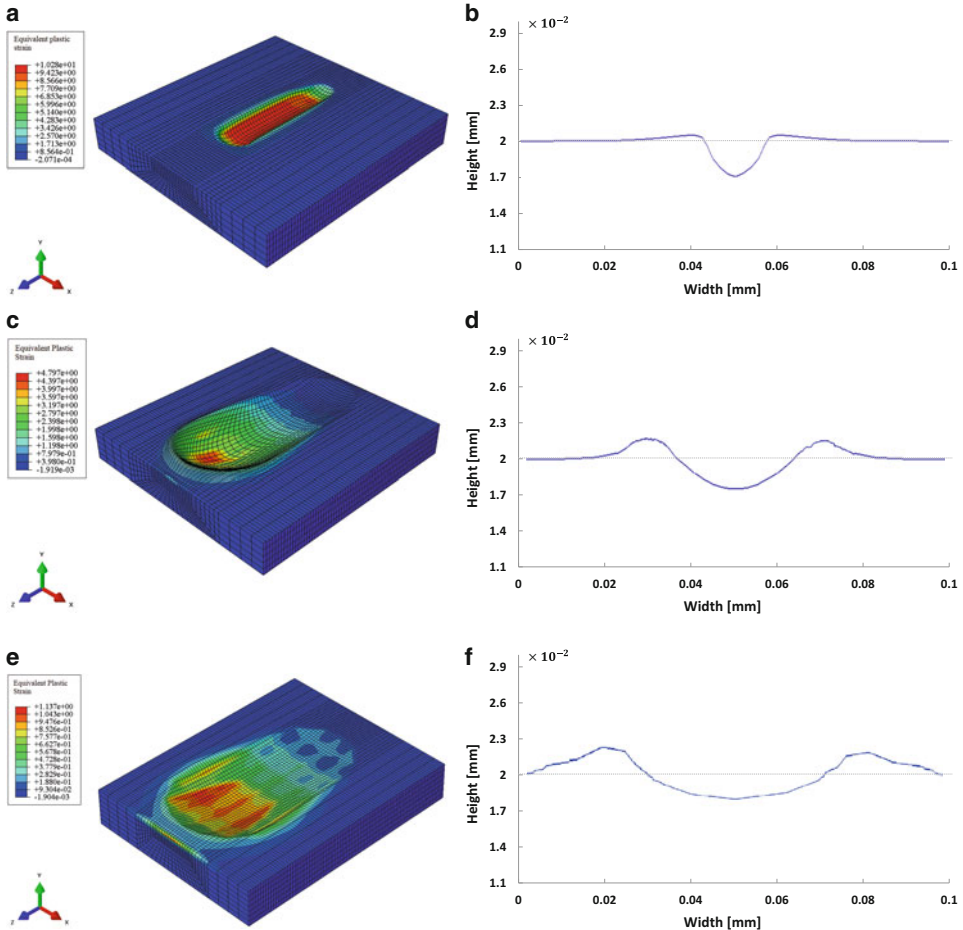
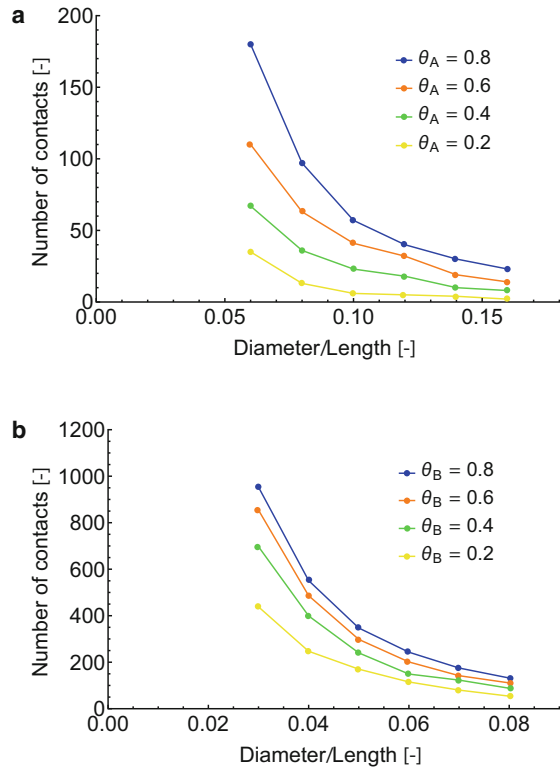


Fig. 3.41 Particle size effect (left) distribution of equivalent plastic strain for **a** $R = 25 \mu\text{m}$, **c** $R = 50 \mu\text{m}$ and **e** $R = 100 \mu\text{m}$ and (right) cross-section of the groove for **b** $R = 25 \mu\text{m}$, **d** $R = 50 \mu\text{m}$ and **f** $R = 100 \mu\text{m}$

The setup for the particle simulation consists of a box with unit dimensions filled with a mixture of particles with different radii. Two types of particles were assumed with the same mechanical properties, but different diameters, $D_A \geq D_B$, and a defined volume ratios θ_A and $\theta_B = 1 - \theta_A$. The particles are generated randomly inside the box and then settled down by applying gravity. Due to the small size of particles, the settling step takes a long time and is the most time-consuming step in the simulation. To have a satisfactory settlement prediction, the box is shaken in which a relative small velocity is applied to the side walls. A linear contact model is considered between the particles. The simulation results indicated that the inter-particle friction coefficient does not have a significant effect on the number of particles being in contact with the surface. Therefore, all wall and

Fig. 3.42 Relation between number of contacts and particle diameter for different volume ratios of **a** A-Particles and **b** B-Particles



particle contacts are supposed to be free of friction. Pressure is applied to the top surface of the particles.

A parametric study was performed to derive a relation between the number of contacting particles as a function of particle size and volume ratio. By varying the diameter and volume ratio, a database is created for each particle type. Figure 3.42 presents the results for the number of contacts per unit area by A- and B-particles. Best curve fitting to these data points is performed using the MATLAB curve fitting tool. Finally, expressions for the number of contacting particles N_c are found as

$$N_{c,A} = 0.9 \theta_A^{(2-1/r_{AB})} D_A^{-2}, \quad N_{c,B} = 0.9 \theta_B^{(1/r_{AB})} D_B^{-2}, \quad (3.7)$$

in which $\theta_A + \theta_B = 1$ and r_{AB} as a ratio of D_A to D_B for $D_A \geq D_B$. These relations are used in the next section to estimate the total abrasive wear rate of the particle mixture.

The contribution of a particle to the total abrasive wear rate is defined by

$$\dot{v}_i = f_{ab} A_{g,i} v_t, \quad (3.8)$$

where v_t indicates the tangential relative velocity between the abrasive particle and the tool. The average area of a groove caused by all particles of type i , $A_{g,i}$, is obtained from

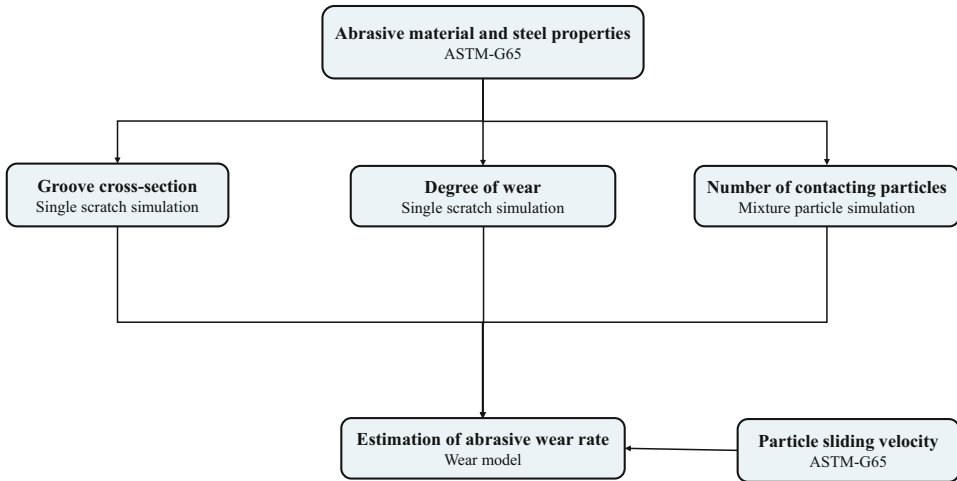


Fig. 3.43 Calculation procedure of abrasive wear model

the single scratch simulations. It is supposed to be a function of influencing parameters, i.e., the mean particle size and the normal contact force (or indentation depth).

The total wear rate \dot{v} of a material is the summation of the wear rate for particles in contact with the tool surface,

$$\dot{v} = \sum_{i=1}^n N_{c,i} \dot{v}_i, \quad (3.9)$$

in which n is the number of particle types and $N_{c,i}$ is the number of contacts per unit area for particles of type i . The abrasive wear rate is determined using the calculation procedure illustrated as a flowchart in Fig. 3.43. The parameters influencing the abrasive behavior and the wear rate can be divided in three categories: abrasive medium characteristic, machinery component properties, and the contact mechanism.

The abrasivity of rocks can be deduced from their mineralogical composition, especially the fraction of hard minerals such as quartz. The important mechanical and geometrical properties of particles are size, shape, and hardness. Based on the literature, larger particles generate a higher contact force, remove the material surface faster, and create a harder texture. However, our observation in the single scratch test is opposite to the size effect reported in the literature. We found that smaller particles, with sharper tips, cause more wear in the form of material removal compared to the plastic deformation caused by larger particles. We speculate that, under a constant load, a smaller particle penetrates deeper into the material and creates a larger groove area.

In general, material removal rate is linearly related to particle hardness. Harder particles act as rigid indenters compared to softer particles and increase the surface roughness. However, for the occurrence of significant abrasion, the ratio between the hardness of the

particles and the surface is important. For a hardness difference higher than ~ 1.2 , the abrasive wear rate remains constant. In tunneling applications, the most abrasive particles are quartz, which is almost five times harder than steel surfaces, such as that of construction steel (see Table 3.4). Therefore, it is supposed that the possible variation in the hardness of sand particles does not influence the resulting abrasive rate.

3.3.7 Simulation of Tool Wear by Micro-Cracking

Wear-protective layers of tunneling tools, used to protect the soft substrates from abrasive wear, are subjected to surface fatigue. This wear mechanism is mainly governed by elasto-plastic deformations, crack initiation and crack propagation on the microscale (see Sect. 3.3.3.2). These effects may not be visible on the macroscale at first, but may lead to macroscopic cracks during the excavation process and ultimately to failure of the tool. For instance, if the cracks cluster, parts of the tool's surface break out. These phenomena are affected by the material's microstructural properties, namely the microstructure morphology and the material properties of the constituents. The surface layers of mining tools consist of metal matrix composites (MMC), which contain brittle carbide inclusions surrounded by a ductile metal matrix. The inclusions supply the resistance against abrasion whereas the properties of the ductile matrix provide crack resistance and thus, the necessary resistance against surface fatigue. Numerical simulations of crack propagation through microstructures can be carried out based on voxel data obtained from micro-CT scans. Basing the simulations on structure images enables the observation of the governing effects, even in complex three-dimensional structures. This property is beneficial, because imaging processes of real microstructures suffer from the problem that the measurement of crack surfaces in three-dimensional bodies, especially for the crack propagation over time, is extremely costly if not partially impossible. Additionally, the mechanical fields, such as the plastic deformations and the stress distributions, can be visualized and investigated in the numerical simulations. Furthermore, the simulations enable comparative studies of different microstructures promising to improve those regarding crack growth resistance and thus wear by design and material choice.

3.3.7.1 Simulation Framework for Ductile Crack Propagation on the Microscale

We developed a numerical method for the efficient simulation of ductile crack propagation at finite strains based on voxel data cf. [101], which enables robust and mesh-independent simulations and is capable of simulating crack propagation along a priori unknown crack paths through brittle as well as ductile materials. Its starting point is the so called Eigen-erosion approach for crack propagation as introduced in [84] and implemented into the Finite Element Method in [69]. This approach was extended to ductile fractures at finite strains in [100].

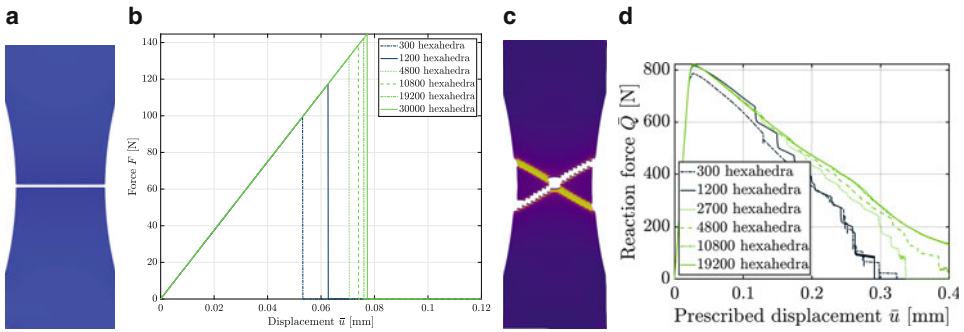


Fig. 3.44 Simulated tension test of **a** a brittle plate, which is loaded vertically with an over time linearly increasing displacements, **b** its resulting reaction force for different numbers of elements and **c** the specimen and **d** reaction force of a plate of ductile material, taken from [100]

The developed algorithm leads to plausible results as demonstrated for the example of a simple tension test (Fig. 3.44). A brittle plate fractures into two parts along a crack perpendicular to the load direction. A shear zone develops at an obtuse angle to the pulling direction. The mesh convergence of the brittle as well as the ductile specimen is demonstrated in the reaction forces. Previously, this algorithm was shown to be capable of simulating subcritical crack propagation under cyclic loading in [102]. For the efficient simulation based on voxel data, the approach is combined with the Finite Cell Method in a new algorithmic framework [101]. Thereby, the problem of meshing the complex microstructures is circumvented because therein, the mesh is generated independently from the inner material boundaries. The material boundaries are imposed by decomposing the elements, the so called “finite cells”, into subcells. These subcells are constructed conformingly according to the material interfaces allowing for a suitable integration of the material coefficient jumps inside the finite elements. A special discretization technique, which ensures efficiency on the one hand and a certain accuracy and numerical stability on the other hand, is applied. In order to maintain accuracy of the crack propagation, the mesh is adaptively refined at the crack tip by splitting the finite cells into separate finite elements whenever the crack enters a finite cell.

We demonstrated the concept of the proposed algorithm and its efficiency using an artificial microstructure as an example (Fig. 3.45). It consists of a spherical tungsten carbide inclusion that is surrounded by an η -carbide layer and a ductile nickel matrix, is simulated with the boundary conditions in Fig. 3.45d to show the concept of the proposed algorithm and its efficiency. Hereby, a tetrahedral mesh, a semi-regular hexahedral mesh with hanging nodes and the proposed algorithm is applied. As shown in Fig. 3.45b, e, the crack path is independent of the chosen discretization type. Furthermore, the semi-regular hexahedral FE mesh and the proposed algorithm lead to a very similar reaction force, cf. Fig. 3.45c. In Fig. 3.45f, the computational efficiency of the proposed approach is demonstrated by comparing the number of equations, that are solved in each Newton-Raphson iteration.

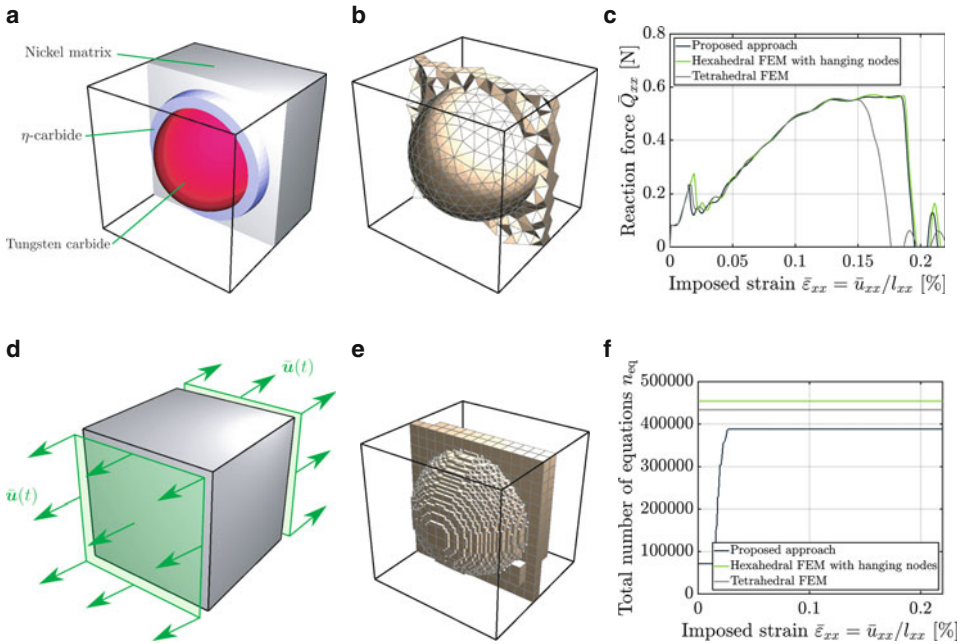


Fig. 3.45 Simulation on an artificial microstructure in **a** and boundary conditions in **d** resulting in the final crack paths for **b** a tetrahedral mesh and **e** a hexahedral mesh. In **c**, the resulting reaction forces and, in **f** the number of equations in each Newton step are shown, cf. [101]

Especially, in the beginning of the simulation of the proposed approach, the number of equations is reduced by a factor of 5 compared to the semi-regular hexahedral FE mesh. However, this academic example was constructed with the purpose of examining the accuracy rather than efficiency. Since all elements in the material interface are fractured in the end, no significant gain in the computational costs can be reached by the proposed method. This circumstance will change when considering real microstructures with only a small fraction of ruptured material interfaces.

3.3.7.2 Voxel-Based Analysis of Crack Propagation Through MMC

We performed simulations on the microstructure obtained from micro-CT scans to examine crack propagation in MMC used as wear-protective layer on tunneling tools. A typical micro-CT scan of the metal matrix composite Ferrotitanite (Fig. 3.46) consists of grey-scale values that represent the density of the specimen and is obtained by measuring the X-rays, which are emitted by an X-ray tube and which penetrate the specimen. The brighter the value, the higher the intensity of the measured X-rays and thus the lower the density of the investigated voxel. For the application, the resulting grey-scale values are processed to erase noise and artifacts. Afterwards, they are binarized by application of a threshold value to identify the distribution of the two composites, here the brittle and

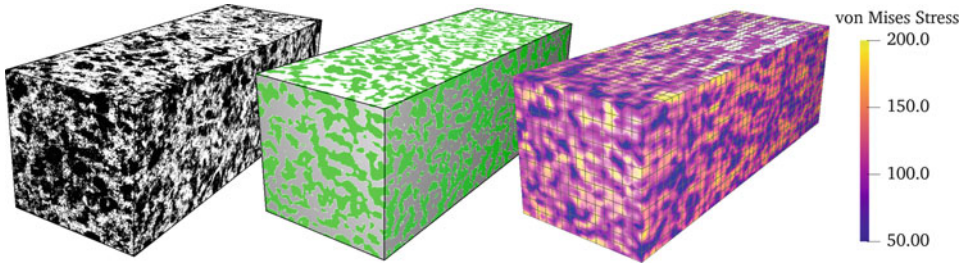


Fig. 3.46 Voxel data as grey-scale values obtained from a micro-CT scan, which is cleaned and binarized into the inclusion (green) and iron matrix phase (silver) and contour plot of the von Mises stress under one dimensional tension in axial direction

stiff titanium carbide inclusions and the ductile iron matrix. Even though the resulting microstructure is of a high complexity, it is discretized without high computational effort by the FCM. Based on this, efficient simulations are carried out on these data. As an example, the result of a one dimensional tension test without the assumption of crack propagation is shown in Fig. 3.46. The material properties of the inclusions are obtained from the literature whereas the material parameters of the iron matrix are fitted to tension tests to accurately represent the behavior in the plastic regime. The von Mises stress is high in the inclusion phase compared to the stress in the ductile matrix (Fig. 3.46). Hence, loads applied on the Ferrotitanite are primarily carried by the stiff inclusions.

A representative section is selected from the whole scan, under linearly increasing deformation in one direction and symmetry boundary conditions in lateral direction, cf. Fig. 3.47a, for the simulation of crack propagation through the microstructure. The crack is initialized as shown in Fig. 3.47b, c by assuming eroded elements at the beginning of the simulation, because the numerical framework only considers crack propagation and not crack initiation. The numerical parameters for the crack propagation, namely the Griffith-type energy release rate G_c and a regularization parameter ϵ , are obtained by fitting them so that the results of a specimen of a tension test breaks into two parts under the correct tensile stress. The overall material behavior is elastic even though one of the constituents, here the metal matrix, behaves elasto-plastically. Furthermore, the crack propagates in steps instead of breaking the material into two parts at once. The resulting crack surface propagates in general straight through the microstructure in agreement with observations from the experimental results.

3.3.7.3 Influence of Different Inclusion Shapes on Crack Propagation

The crack propagation through different microstructure morphologies is investigated, to improve the material microstructure of the layers applied to the mining tools regarding surface fatigue. Therefore, simulations are carried out under the assumption of simplified inclusion shapes.

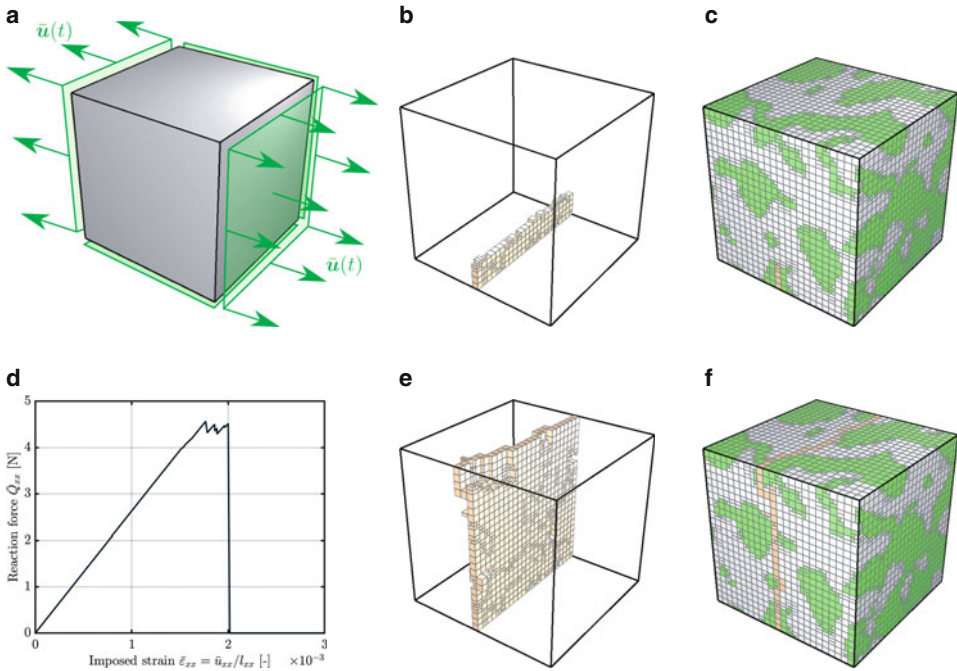


Fig. 3.47 a Boundary conditions of a one-dimensional tension test on MMC microstructure with b initial crack and microstructure, c consisting of titanium carbide inclusions (green) and iron matrix (silver) resulting in the reaction force in d and the crack path in d and e, cf. [101]

The inclusion shape depends on the production process of the material. The simplified microstructure of a cold-work steel, produced by hot-isostatic pressing (HIP), is characterized by spherical chromium carbide inclusions embedded in the ductile steel matrix (Fig. 3.48). In contrast, the inclusions are shaped as ellipsoids in Fig. 3.48d, which is typical for hot-rolled steels. Symmetry boundary conditions with an externally applied deformation (Fig. 3.47) are applied, which increases linearly over time. In the resulting crack paths of the cold work tool steel microstructure containing the spherical carbides (Fig. 3.48b, e), the crack primarily propagates around the inclusions whereas the crack in the microstructure containing ellipsoids propagates straight through the inclusion phase. This effect occurs because the crack propagates along the energetically most favorable path. Different from the case with ellipsoids, now the path around the spherical inclusions is energetically more favorable than the one intersecting them. The same effects are observed in experiments. For instance, the crack in Fig. 3.48c through a real microstructure which inherits rather spherical inclusions avoids propagation through the chromium carbides. However, cracks propagate through the ellipsoidal inclusions as well (Figure 3.48f), as also observed in the simulations.

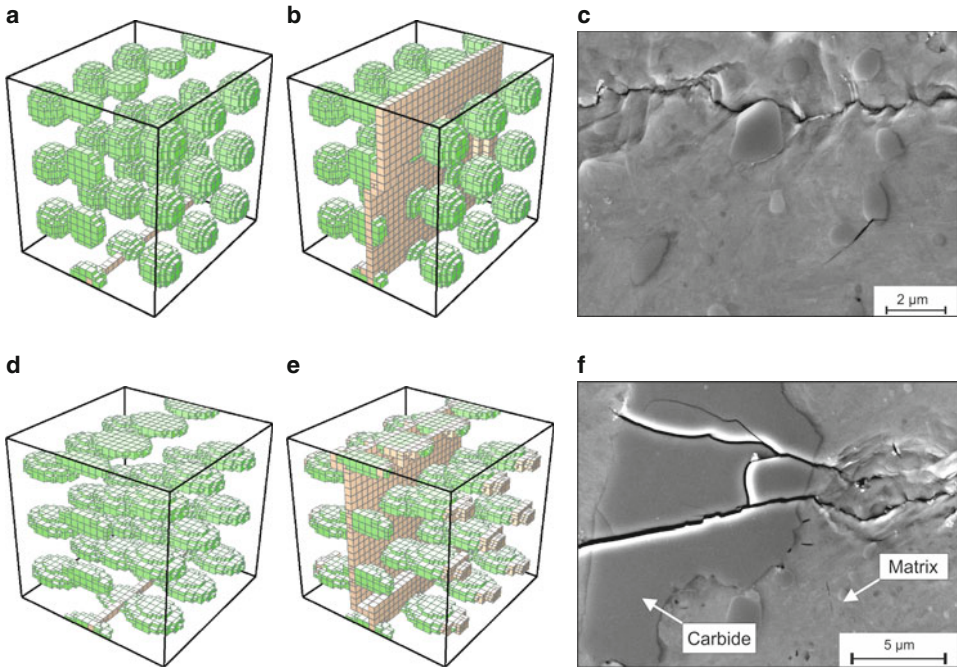
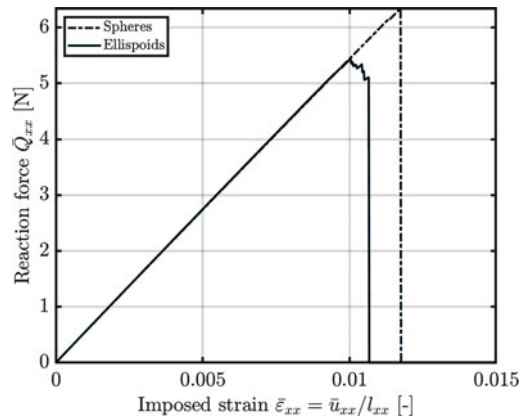


Fig. 3.48 Microstructure consisting of **a** spherical and **d** ellipsoidal chromium carbide inclusions (green) within ductile steel matrix and **b**, **e** the resulting crack paths (gold) that occur under the boundary conditions in Fig. 3.47a. **c** and **f** show the microstructure of comparable experiments

Fig. 3.49 Reaction force of one-dimensional tensile test with boundary conditions in Fig. 3.47a of the cold work steel microstructures in Fig. 3.48a, c



The maximum forces and displacements are extracted from the force-displacement curves, to decide, which morphology leads to a higher resistance against crack propagation and thus surface fatigue. The cold work tool steel microstructure with spheres (Fig. 3.49) is capable of enduring a higher force and larger imposed mechanical energy than the microstructure which includes ellipsoids. Therefore, it is expected that the unrolled material

inherits a higher resistance against surface fatigue than the rolled material. In general, the simulation of crack propagation for the investigation of the crack resistance can also be applied on different forms of microstructures, e.g., ones which result from other production processes, like casting. Furthermore, microstructures with different inclusion sizes and microscopic material properties can be analyzed. Improvements can be suggested regarding the choices of microstructures of the metal matrix composite layers on the tunneling tools by comparing the results of these simulations.

3.3.8 Monitoring of tool wear and damages

We investigated the possibility of monitoring the cutting tools of a TBM in real time to ultimately reduce maintenance and downtimes. While performance and other parameters of TBMs are routinely monitored [65], monitoring the cutting tools directly has to overcome many challenges. In civil structures and rotary machinery, such as jet engines, wind turbines and trains, where monitoring systems are already in use, the conditions are often assumed to be quasi static. During operation, the different phases of an operational cycle of a machine, are considered as a whole. They are therefore static, as the machine just repeats the same cycle. However, for a TBM this assumption is taken to a different magnitude compared to other machines. Factors that influence the “cycle” of a TBM are the amount of overburden, cavities and excavated materials leading to the shield partially not being in contact to the tunnel face as well as water content, shield force/head pressure and most importantly the type of rock or soil.

We introduced the general principles of machine monitoring and damage detection before discussing possible sensor technologies and where these can be applied regarding TBM. To address the possibility of monitoring a TBM, we used vibration-based experimental data from the RTD (Sect. 3.3.4.1) as a small scale model of the disc cutters. Then strategies and methods will be explained, and finally we conclude with a proof of concept using artificial damages.

3.3.8.1 Principle of wear and damage detection

The fundamental concepts of detecting damage in machine parts and structural components come from condition monitoring (CM) and structural health monitoring (SHM), respectively, and are highly application specific (e.g., [32]). The damages that should be detected need to be defined to build a monitoring system. Furthermore, the operational and environmental conditions should be determined to evaluate limitations of the data acquisition. The acquisition requires selecting the type, number, and location of sensors. It is important to normalize data, to separate damage relevant information from other influences. After that, feature extraction and information condensation take place. Finally, the extracted features need to be statistically analyzed and classified into damaged and undamaged cases. This last step is called statistical model development and can be performed involving one of three common methods: supervised learning, unsupervised learning or

novelty detection. The first and second are neural-network based methods, while the second and third method do not require a priori knowledge of the damaged case [28].

The economical aspects of a monitoring system are to be considered, in particular in the planning and testing phases. With more knowledge about the quality and characteristics of collected data and specifics of the monitored machine/structure, analysis methods become more robust and data acquisition can be reduced, lowering monitoring costs.

Our research concentrated on the most common damages of disc cutters and their bearings, using vibration-based feature extraction. For disc cutters these damages are wear, impact damage, split ring loss or blockage due to seal failure of the bearings [31] and for bearings these are single-point defects and generalized roughness faults [109]. While bearings are well investigated regarding monitoring [25, 61, 99], monitoring of disc cutters is in its infancies [82, 98] and until today rarely been used on actual TBMs [66]. Currently, the prediction of wear is based on many parameters of TBMs, which are already monitored, like cutter head revolutions per minute (RPM), cutter head torque, axial force and displacement of thrust jacks [65]. We explored the use of acceleration (model 333B30–PCB Synotech) and force (KM40–ME-Systeme) sensors in a small scale model of a TBM.

3.3.8.2 Vibration-based monitoring

Every machine that carries out physical work generates vibrations. These vibrations fundamentally depend on the properties of each machine component, i.e., geometry, material parameters, velocity, etc. While the machine is running, all of its components experience wear, which changes their properties and therefore the characteristics of the generated vibrations. The basic idea of monitoring is to determine how these vibrations change over time and distinguish between an operational state and a damaged one.

Most of the time, machines have components, like gears, bearings, and shafts, that generate repetitive signals, i.e., with systematic frequencies. These signals can be classified into stationary and non-stationary, meaning that statistical properties do not change over time, continuous or transient, and random or deterministic. The classification is important for a selection of an appropriate signal processing method, like Fourier transform, Hilbert transform, digital filters, and demodulation.

The greatest advantages of using vibrations for monitoring are the immediate response of vibrations to changes and the ability to identify the actual faulty component. Oil analysis, for example, can take days for wear to be detectable based on the accumulation of metal chips and even then it is unclear from which part these originate [75].

3.3.8.3 Proof of concept

To demonstrate that damages can be detected with the RTD, we use data from experiments and two models. Each of these datasets contains data for an undamaged and damaged case. Two different methods for damage detection, namely the Hilbert transform and a complex demodulation algorithm, were used to investigate the capability of damage detection [73]. We extracted the same feature with both envelope generating methods and compared them.

The data show that for the different datasets the Hilbert transform,

$$E_x = F^{-1}(F(x_i)2U) = x_i + iH(x_i), \quad (3.10)$$

with the discrete time series x_i , the Fourier transform F , the Heaviside step function U , the Hilbert transform H and the resulting Envelope of the data E_x , extracts damage relevant feature more efficiently.

Based on the results from [73], we conducted a larger study with purely experimental data to correlate the initial findings with an increasing, albeit artificially introduced, damage state of disc cutters [74]. We performed 65 experiments with three individual disc cutters of same geometry and material and up to four different damage states. The experiments were done using the RTD described in Sect. 3.3.4.1. However, the conditions the disc cutters were performing at can be described as rather ideal. Rocks were not used at this stage, instead the disc cutters rolled on a steel surface. We removed low frequency components from the recorded data using a moving average filter

$$\bar{x}_i = x_i - \frac{1}{2n+1} \sum_{k=i-n}^{i+n} x_k. \quad (3.11)$$

Here, $2n+1=21$ is the size of the used box car window of the filter. After this step, only high frequency noise and the interaction of the damage of the disc cutter, which happens exactly once every rotation, is left. Figure 3.50a shows an example of the raw data obtained from these experiments. Here, the disc cutter had a damage of roughly 2 mm

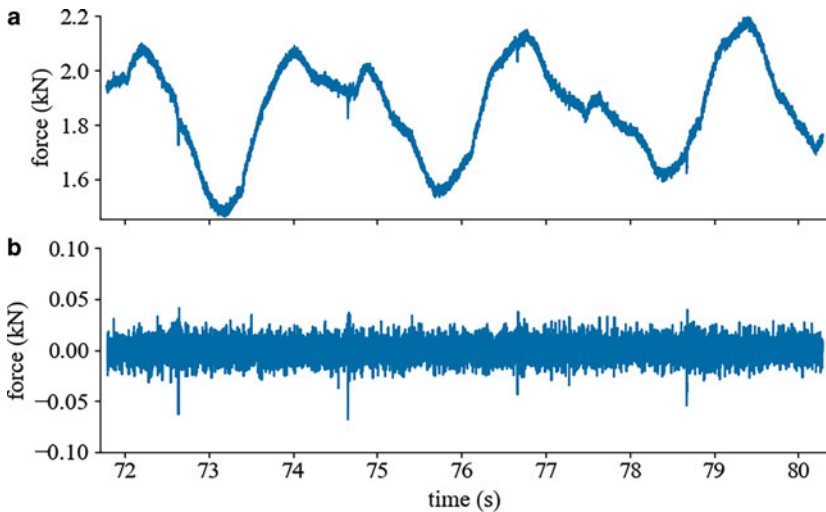


Fig. 3.50 **a** Exemplary time domain data of a disc with a damage interacting every two seconds. **b** The same data with the moving average removed from it, still showing the damage interaction

in size. Figure 3.50b shows the results of the filtering method. In this short example, the interaction can be seen four times with an interval of two seconds in between.

After the data is cleansed, the envelope is calculated according to Eq. 3.10 and transformed to the frequency domain, where the feature, called damage indicator (DI) from here on, is extracted. The DI we chose is the maximum value of the envelope between 0.45 and 0.55 Hz, as the frequency of the interaction of the damage is expected to be roughly 0.5 Hz. This expectation is based on the a priori knowledge of the speed of the RTD and the ratio of diameters of the parts involved. In an attempt to further improve the correlation between DI and damage size, the DI is normalized by the total energy of the signal

$$E_T = \frac{1}{N} \sum_{k=0}^{N-1} \|F_k\|^2, \tag{3.12}$$

with the total number of discrete samples N in the frequency domain.

The results for disc cutters A and B show a correlation between DI and damage size for both considered disc cutters (Fig. 3.51). DI from disc cutter A benefit from the normalization, while the same is not true for disc cutter B . Results for the third disc cutter were not conclusive and are not considered here. An extended analysis of these results revealed that the operational conditions have greater impact than expected [74].

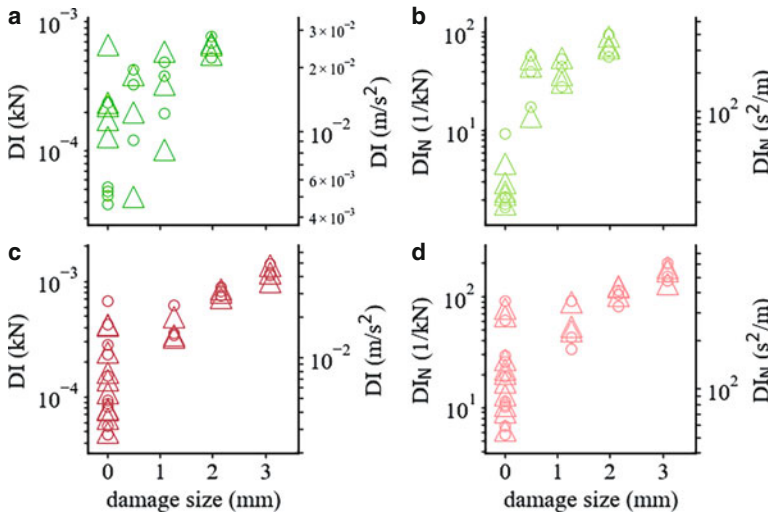


Fig. 3.51 The left column of plots, **a** and **c**, shows the damage indicator (DI) without normalization and the right column, **b** and **d**, show the DI with normalization. In the first row, only data of disc cutter A , green color, and in the second row data of disc cutter B , red color, is shown. Each of the four figures shows data from a force sensor on the left y -axis, represented by circles, and the right y -axis shows data from an acceleration sensor, represented by triangles

3.3.8.4 Outlook

In the future, we will expand our investigations towards disc cutters used on Anröchter sandstone, a rock with moderate anisotropy and low porosity (see Sect. 3.2.2.2). Exploratory tests showed that the rock is initially free of fractures. Specimens are drilled from blocks with a core drill. To define a baseline, data with mainly damage free discs and bearings will be collected. The baseline will then be used for statistical analysis to discriminate among damage sensitive and insensitive features. The monitoring will be improved by using high frequency sensors and video footage of the experiments. We plan to improve on the currently used sensors to enable modal analysis. Video footage will be used to correlate as many parts of the data as possible to different non-damage-related events, such as rock fracturing. Improvements of the data analysis will consider fitting algorithms, methods as well as using neural networks for direct disc cutter monitoring.

3.4 Influence of Tool Wear on the Effectiveness of Excavation

The material concept for tunneling tools is based on two main aims. A long and well predictable service lifetime helps to keep maintenance interruptions short and a high tunneling efficiency allows for fast penetration rates of the TBM. Based on the results of our laboratory testing and numerical modeling of tool wear, several recommendations can be derived to improve material concepts for tunneling tools and thus the excavation process.

Counteracting the dominant wear mechanism, which depends on the properties of the excavated ground, is the key to increase the tool's lifetime. Selection of the optimal material or an optimal tool design is based on suitable wear tests and in-depth analysis of the tribological system during the planning stage of the tunneling project. For granular soils, which will mainly be excavated by scraping tools, the hardness of the soil particles, their size and morphology have to be considered for the material choice of wear protective layers and inserts on chisels, reamers, and scrapers to inhibit abrasive wear. Furthermore, the presence of boulders, schistosity and other soil-inhomogeneities should be assessed to evaluate the extent of cyclic mechanical loading that is to be expected. If severe cyclic loading is predicted, it is advisable to choose materials with a low content of hard-phases for wear-protective layers or inserts to increase their content of the crack-resistant metal matrix. Küpferle [46] showed for cemented carbides that the fatigue strength of a 15 vol%-Co grade is increased by about 80 %, compared to a 6 vol%-Co grade under cyclic compressive loading. Thus optimizing Co-content bears the potential for significant improvement potential for wear protective inserts, that wear out due to fatigue micro-spalling under the repetitive impact of abrasive particles.

Apart from the hard-phase volume content, the behavior of the metal matrix in wear-resistant composite materials was identified as the decisive factor to promote a high fatigue strength. The commonly used Ni-based metal-matrix composites of NiBSi or NiCrBSi, reinforced with fused tungsten carbide hard particles, are susceptible to fatigue cracking due to their comparably low strength Ni-metal matrix, which promotes premature crack

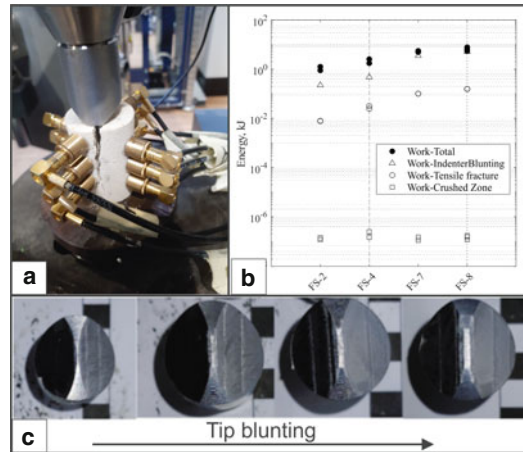
initiation at a low number of loading cycles. In contrast, Fe-based and Co-based hard alloys offer significant fatigue strength, due to their metal matrices, which exhibit a higher strength than Ni-based metal matrices (Fig. 3.30). Despite the challenges connected with the use of Fe-based hard alloys, such as higher processing temperatures and restricted availability of well-established hard phases, they represent a promising material concept. Possible applications that allow for the replacement of fused tungsten carbide with soft carbides of the type M_7C_3 , comprise soils with a hardness of the soil particles below 1000 HV (e.g. Flint), or soils with severe cyclic load potential due to large particle sizes and thus high impact energies during contact to the tool.

Regarding disc cutters, tool lifetimes can especially be improved for tunneling in soft-rock with a low amount of inhomogeneities. Then, the disc cutters are only rarely subjected to severe mechanical loads and the main wear mechanism is abrasion, as the disc cutters are dragged through the ground with a large relative movement. In these cases, carbide-containing cold-work tool steels like X153CrMoV12-1 or 90MnCrV8 may replace the currently used hot work-tool steels (X50CrMoV5-1) with a low content of hard-phases to achieve high abrasion resistance. Adjusted heat treatments can be applied to form low (< 15 vol%) amounts of the tough phase retained austenite to increase the fatigue strength and fracture toughness of these cold-work tool steels (Fig. 3.33). This metastable phase can transform to the hard phase martensite, featuring a higher resistance against abrasive wear. In addition, subcritical crack growth is stopped due to the residual compressive stresses that are created as a result of the lattice transformation. For excavation of hard rocks or heterogeneous soils, the hot-work tool steels remain the superior choice due to their overall high fatigue resistance. To guarantee the desired material behavior, tool manufacturers and suppliers must pay attention to the chemical purity of the utilized steel and to the heat-treatment. Especially the contents of sulfur, phosphor, and oxygen have to be kept to the lowest possible level, as these elements form non-metallic inclusions, which promote crack initiation under cyclic loading. Refinement processes such as electro-slag remelting can reduce the content of these unwanted elements and can increase the overall homogeneity of the steel, which improves the mechanical properties.

3.4.0.1 Implications for Tunneling Efficiency

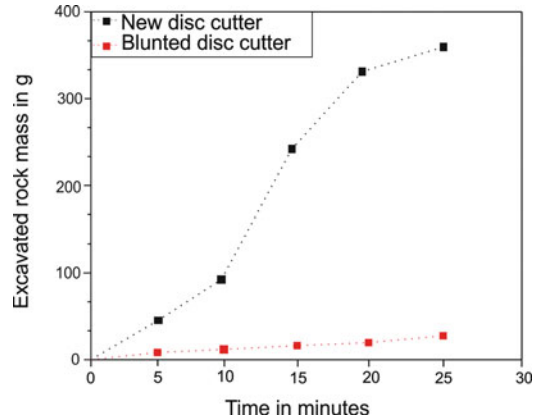
To realize the predetermined advancement rates of the TBM, the tunneling tools must be capable of excavating a certain amount of ground-volume in a fixed timespan. The excavation process includes the release of soil particles from the tunnel-face and the removal of the material from the excavation chamber. The excavation process of rock by the means of disc cutters involves introducing compressive stresses and subsequent crack propagation inside the rock, which eventually leads to chipping. To achieve high efficiency of this excavation mechanism, the applied external force has to be converted into the newly created crack surface, which encloses a maximum rock volume. The energetic assessment implies a positive impact of large single cracks in the rock on the tunneling efficiency, in comparison to a high number of small cracks that take up the same amount of fracture work than one large crack. Therefore, rock excavation should aim for large fragment sizes of the released material.

Fig. 3.52 **a** Experimental setup of uniaxial rock indentation testing, **b** calculated energy consumption of various system components in the indentation test, **c** blunting of a soft indenter over several cycles of use



Uniaxial indentation tests on several rock types (see Fig. 3.52a), as well as rock excavation experiments at the RUB-Tunneling Device were conducted, to investigate the interaction of different tool geometries with rocks. The most significant finding of the indentation experiments was that indenters with a sharp tip, which produces a small contact area and therefore high stresses in the contact area, facilitate the propagation of a large median crack, in contrast to blunt indenters. Blunt indenters cause the formation of a large pseudo-plastic zone at the rock surface, which is characterized by pore collapse and propagation of a high number of microcracks and therefore dissipates energy but will not lead to the desired fragmentation (see Fig. 3.52b). In addition, the plastic deformation of the indenter itself takes up a significant amount of the externally applied work. For these reasons, blunt indenters and correspondingly blunt cutting edge geometries of disc cutters appear unfavorable concerning the tunneling efficiency. Based on this result, geometry changes of the cutting edge during the tunneling process, which are caused by plastic deformation or other wear phenomena, must be critically assessed. Indentation tests with an indenter made of soft steel (300 HV30) on Fontainebleau sandstone revealed successive blunting of the indenter tip after several tests (see Fig. 3.52c). In correlation, the necessary indentation forces to fracture the rock specimen increased significantly. Excavation experiments on Anröchter sandstone with a pristine disc cutter (2.8 mm cutting edge width) and a worn disc cutter with blunted cutting edge (4.0 mm cutting edge width) demonstrated the impact of the tool geometry change on the tunneling efficiency. At the same contact pressure, the new disc cutters excavation performance was much better, compared to the blunted disc cutter (see Fig. 3.53). The large difference can be traced back to the rock fracture behavior that is caused by the disc cutters. While the new disc cutter caused fracture of large rock particles, the blunted disc cutter only generated rock dusting by releasing single rock grains and small chips. This experimental investigation confirms the previously presented theoretical analysis and emphasizes the importance of cutting edge retention of the disc cutters for the tunneling efficiency during rock excavation.

Fig. 3.53 Comparison of the excavation capability of a disc cutter with small edge width (2.8 mm cutting edge width) and a disc cutter (4.0 mm cutting edge width), measured on Anröchter sandstone



References

1. H. Alehossein, E. Detournay, and H. Huang. “An analytical model for the indentation of rocks by blunt tools”. In: *Rock Mechanics and Rock Engineering* 33.4 (2000), pp. 267–284. ISSN: 1434-453X. <https://doi.org/10.1007/s006030070003>.
2. American Society of Testing and Materials. *Standard Test Method for Measuring Abrasion Using the Dry Sand/Rubber Wheel Apparatus*. norm. 1985.
3. G. Angenheister, ed. *Zahlenwerte und Funktionen aus Naturwissenschaft und Technik*. Vol. Neue Serie, Gruppe 5. Landolt-Börnstein. Berlin: Springer, 1982.
4. J. Archard. “Contact and rubbing of flat surfaces”. In: *Journal of applied physics* 24.8 (1953), pp. 981–988.
5. M. Ashby and C. Sammis. “The damage mechanics of brittle solids in compression”. In: *Pure and applied geophysics* 133.3 (1990), pp. 489–521.
6. A. L. Bal and G. Meschke. “Adaptive two-phase Particle Finite Element model for soft soil excavations in partially saturated soils”. In: *th edition of the International Conference on Computational Methods for Coupled Problems in Science and Engineering (COUPLED PROBLEMS 2021)*. 2021.
7. A. R. L. Bal, T. S. Dang, and G. Meschke. “A 3D particle finite element model for the simulation of soft soil excavation using hypoplasticity”. In: *Computational Particle Mechanics* 7.1 (2020), pp. 151–172.
8. A. R. L. Bal et al. “Hypoplastic particle finite element model for cutting tool-soil interaction simulations: Numerical analysis and experimental validation”. In: *Underground Space* 3.1 (2018), pp. 61–71.
9. H. Berns and W. Theisen. *Eisenwerkstoffe: Stahl und Gusseisen*. Springer-Verlag, 2008.
10. H. Berns and W. Theisen. *Hartlegierungen und Hartverbundwerkstoffe: Gefüge, Eigenschaften, Bearbeitung, Anwendung*. Springer-Verlag, 1998.
11. W. Brace and D. Kohlstedt. “Limits on lithospheric stress imposed by laboratory experiments”. In: *Journal of Geophysical Research: Solid Earth* 85.B11 (1980), pp. 6248–6252.
12. L. Brackmann et al. “Subcritical crack growth in hard alloys under cyclic loading”. In: *Fatigue and Fracture of Engineering Materials and Structures* 2 (2021), pp. 349–365.

13. S. N. Butt and G. Meschke. “Peridynamic analysis of dynamic fracture: influence of peridynamic horizon, dimensionality and specimen size”. In: *Computational Mechanics* 67.6 (June 2021), pp. 1719–1745. ISSN: 1432-0924. <https://doi.org/10.1007/s00466-021-02017-1>.
14. S. Butt and G. Meschke. “A 3D peridynamic model of rock cutting with TBM disc cutters”. In: *Proceedings of the 7th GACM Colloquium on Computational Mechanics for Young Scientists from Academia and Industry*. Ed. by M. von Scheven, M. Keip, and N. Karajan. Stuttgart, Germany: Institute for Structural Mechanics, University of Stuttgart, 2017, pp. 752–755.
15. S. Butt and G. Meschke. “A rate-dependent damage model for prediction of high-speed cracks”. In: *Proceedings in Applied Mathematics and Mechanics (PAMM)* (2018). <https://doi.org/10.1002/pamm.201800330>.
16. S. Butt and G. Meschke. “Interaction of cutting disc with heterogeneous ground”. In: *Proceedings of Applied Mathematics and Mechanics* 20 (2021), 20: e202000060. <https://doi.org/10.1002/pamm.202000060>.
17. S. N. Butt, J. J. Timothy, and G. Meschke. “Wave dispersion and propagation in state-based peridynamics”. In: *Computational Mechanics* 60.5 (2017), pp. 725–738.
18. R. P. Chapuis and M. Aubertin. *Predicting the coefficient of permeability of soils using the Kozeny-Carman equation*. Tech. rep. 2500 Chemin de Polytechnique, Montreal, QC H3T 1J4 Canada: Polytechnique Montréal, 2003.
19. L. H. Chen and J. F. Labuz. “Indentation of rock by wedge-shaped tools”. In: *International Journal of Rock Mechanics and Mining Sciences* 43.7 (2006), pp. 1023–1033. ISSN: 1365-1609. <https://doi.org/10.1016/j.ijrmms.2006.03.005>.
20. C. Coetzee and D. Els. “Calibration of granular material parameters for DEM modelling and numerical verification by blade–granular material interaction”. In: *Journal of Terramechanics* 46.1 (2009), pp. 15–26. ISSN: 0022-4898.
21. R. Costamagna, J. Renner, and O. T. Bruhns. “Relationship between fracture and friction for brittle rocks”. In: *Mechanics of Materials* 39.4 (2007), pp. 291–301. <https://doi.org/10.1016/j.mechmat.2006.06.001>.
22. R. J. Cuss, E. H. Rutter, and R. F. Holloway. “The application of critical state soil mechanics to the mechanical behaviour of porous sandstones”. In: *International Journal of Rock Mechanics and Mining Sciences* 40 (2003), pp. 847–862.
23. H. Czichos. *Tribologie-Handbuch: Tribometrie, Tribomaterialien, Tribotechnik*. Vieweg + Teubner, 2010.
24. P. Drucker. “Abrasive of soil and tool wear in ground engineering and tunnelling”. In: 156 (2011), pp. 1–7.
25. Z. Duan et al. “Development and trend of condition monitoring and fault diagnosis of multi-sensors information fusion for rolling bearings: a review”. In: *The International Journal of Advanced Manufacturing Technology* 96.1-4 (Jan. 2018), pp. 803–819. <https://doi.org/10.1007/s00170-017-1474-8>.
26. A. V. Dyskin, L. N. Germanovich, and K. B. Ustinov. “A 3-D model of wing crack growth and interaction”. In: *Engineering Fracture Mechanics* 63.1 (1999), pp. 81–110.
27. E. Eberhardt. “The Hoek–Brown failure criterion”. In: *The ISRM Suggested Methods for Rock Characterization, Testing and Monitoring: 2007-2014*. Springer, 2012, pp. 233–240.
28. C. R. Farrar and K. Worden. “An introduction to structural health monitoring”. In: *Philosophical Transactions of the Royal Society A: Mathematical, Physical and Engineering Sciences* 365.1851 (Dec. 2006), pp. 303–315. <https://doi.org/10.1098/rsta.2006.1928>.
29. E. Fjaer. “Relations between static and dynamic moduli of sedimentary rocks”. In: *Geophysical Prospecting* 67.1 (2019), pp. 128–139. <https://doi.org/10.1111/1365-2478.12711>.
30. F. Frank and L. B. “On the theory of Hertzian fracture”. In: *Proceedings of the Royal Society of London A: Mathematical, Physical and Engineering Sciences* 299 (1967), pp. 291–306.

31. C. Frenzel, H. Käsling, and K. Thuro. “Factors Influencing Disc Cutter Wear”. In: *Geomechanik und Tunnelbau* 1.1 (Feb. 2008), pp. 55–60. <https://doi.org/10.1002/geot.200800006>.
32. H. Friedmann and P. Kraemer. “Vibration-based condition monitoring, structural health monitoring, population monitoring—Approach to a definition of the different concepts by means of practical examples from the field of wind energy”. In: *Proceedings of the 8th European Workshop on Structural Health Monitoring (EWSHM 2016), Bilbao, Spain*. 2016, pp. 5–8.
33. K.-H. Gahr. “Wear by hard particles”. In: *Tribology International* 31 (1998), pp. 587–596.
34. H. Gebrande. “Elastic wave velocities and constants of rocks and rock forming minerals”. In: ed. by G. Angenheister. Vol. 1b. Zahlenwerte und Funktionen aus Naturwissenschaft und Technik, Landolt-Börnstein, Neue Serie, Gruppe 5. Berlin: Springer, 1982, pp. 1–34.
35. R. Gertsch, L. Gertsch, and J. Rostami. “Disc cutting tests in Colorado Red Granite: Implications for TBM performance prediction”. In: *International Journal of rock mechanics and mining sciences* 44.2 (2007), pp. 238–246.
36. C. Gonzalez, M. Arroyo, and A. Gens. “Wear and abrasivity: observations from EPB drives in mixed soft-rock sections”. In: *Geomechanics and Tunneling* 3 (2015), pp. 258–264.
37. A. Griffith. “Theory of rupture”. In: ed. by C. Biezeno and J. Burgers. First International Congress Applied Mechanics. 1924, pp. 55–63.
38. G. Gudehus. *Physical Soil Mechanics*. Advances in Geophysical and Environmental Mechanics and Mathematics. Springer, 2011, p. 840. <https://doi.org/10.1007/978-3-540-36354-5>.
39. H. Huang, B. Damjanac, and E. Detournay. “Normal wedge indentation in rocks with lateral confinement”. In: *Rock Mechanics and Rock Engineering* 31.2 (1998), pp. 81–94. ISSN: 1434-453X. <https://doi.org/10.1007/s006030050010>.
40. H. Huang and E. Detournay. “Discrete element modeling of tool-rock interaction II: rock indentation”. In: *International Journal for Numerical and Analytical Methods in Geomechanics* 37.13 (2013), pp. 1930–1947. ISSN: 0363-9061.
41. J. C. Jaeger, N. G. Cook, and R. Zimmerman. *Fundamentals of rock mechanics*. John Wiley & Sons, 2009.
42. K. L. Johnson. “The correlation of indentation experiments”. In: *Journal of the Mechanics and Physics of Solids* 18.2 (1970), pp. 115–126. ISSN: 0022-5096. [https://doi.org/10.1016/0022-5096\(70\)90029-3](https://doi.org/10.1016/0022-5096(70)90029-3).
43. K. L. Johnson and K. L. Johnson. *Contact mechanics*. Cambridge university press, 1987. ISBN: 0521347963.
44. H. Jones et al. *Test Methods For High Rate Impact Loading Of Hardmetals*. EURO PM2012, 2012.
45. F. Köppl. *Abbauwerkzeugverschleiß und empirische Verschleißprognose beim Vortrieb mit Hydroschild TVM in Lockergesteinen*. TU München, 2014.
46. J. Küpferle et al. “Influence of the slurry-stabilized tunnel face on shield TBM tool wear regarding the soil mechanical changes – Experimental evidence of changes in the tribological system”. In: *Tunnelling and Underground Space Technology* 74 (2018), pp. 206–216. <https://doi.org/10.1016/j.tust.2018.01.011>.
47. J. Küpferle, A. Röttger, and W. Theisen. “Excavation tool concepts for TBMs – Understanding the material-dependent response to abrasive wear”. In: *Tunnelling and Underground Space Technology* 68 (2017), pp. 22–31.
48. J. Küpferle, A. Röttger, and W. Theisen. “Fatigue and surface spalling of cemented carbides under cyclic impact loading – Evaluation of the mechanical properties with respect to microstructural processes”. In: *Wear* 390–391 (2017), pp. 33–40.

49. J. K pferle et al. "Assessment of the LCPC abrasiveness test from the view of material science / Bewertung des LCPC-Abrasivit tstests aus werkstofftechnischer Sicht". In: *Geomechanics and Tunneling* 3 (2015), pp. 211–220.
50. J. K pferle et al. "The RUB Tunneling Device – A newly developed test method to analyze and determine the wear of excavation tools in soils". In: *Tunnelling and Underground Space Technology* 59 (2016), pp. 1–6.
51. B. R. Lawn, A. G. Evans, and D. B. Marshall. "Elastic/Plastic Indentation Damage in Ceramics: The Median/Radial Crack System". In: *Journal of the American Ceramic Society* 63.9-10 (1980), pp. 574–581. ISSN: 0002-7820. <https://doi.org/10.1111/j.1151-2916.1980.tb10768.x>.
52. A. R. Leon, T. S. Dang, and G. Meschke. "Computational Excavation Analysis of a Single Cutting Tool using a Hypoplastic Constitutive Model". In: *PAMM* 16.1 (2016), pp. 369–370. ISSN: 1617-7061.
53. A. R. Leon and G. Meschke. "Two-phase Particle Finite Element model for the coupled analysis of cutting tool-soil interaction in partially saturated soft soils". In: *International Journal for Numerical and Analytical Methods in Geomechanics* (2022). Submitted.
54. P. A. Lindqvist, H. H. Lai, and O. Alm. "Indentation fracture development in rock continuously observed with a scanning electron microscope". In: *International Journal of Rock Mechanics and Mining Sciences & Geomechanics Abstracts* 21.4 (1984), pp. 165–182. ISSN: 0148-9062. [https://doi.org/10.1016/0148-9062\(84\)90794-0](https://doi.org/10.1016/0148-9062(84)90794-0).
55. D. J. Littlewood. "Roadmap for peridynamic software implementation". In: *SAND Report, Sandia National Laboratories, Albuquerque, NM and Livermore, CA* (2015).
56. H. Y. Liu et al. "Numerical simulation of the rock fragmentation process induced by indenters". In: *International Journal of Rock Mechanics and Mining Sciences* 39.4 (2002), pp. 491–505. ISSN: 1365-1609. [https://doi.org/10.1016/S1365-1609\(02\)00043-6](https://doi.org/10.1016/S1365-1609(02)00043-6).
57. Q. Liu et al. "Experimental study on rock indentation using infrared thermography and acoustic emission techniques". In: *Journal of Geophysics and Engineering* 15.5 (2018), pp. 1864–1877. ISSN: 1742-2132. <https://doi.org/10.1088/1742-2140/aac096>.
58. D. Lockner. "The role of acoustic emission in the study of rock fracture". In: *International Journal of Rock Mechanics and Mining Sciences & Geomechanics Abstracts* 30.7 (1993), pp. 883–899. [https://doi.org/10.1016/0148-9062\(93\)90041-B](https://doi.org/10.1016/0148-9062(93)90041-B).
59. D. A. Lockner. "Rock failure". In: *Rock physics and phase relations: A handbook of physical constants*. Ed. by T. J. Ahrens. Vol. 3. AGU Reference Shelf. American Geophysical Union, 1995, pp. 127–147.
60. J. Macias. *Hard Rock Tunnel Boring – Performance Predictions and Cutter Life Assessments*. Trondheim: NTNU, 2016.
61. C. Malla and I. Panigrahi. "Review of Condition Monitoring of Rolling Element Bearing Using Vibration Analysis and Other Techniques". In: *Journal of Vibration Engineering & Technologies* 7.4 (May 2019), pp. 407–414. <https://doi.org/10.1007/s42417-019-00119-y>.
62. F. McClintock. "Friction on Griffith cracks in rocks under pressure". In: *Proc. 4th US Nat. Congr. Appl. Mech.* Vol. 2. 1962, pp. 1015–1022.
63. S. Miedema. "The cutting of densely compacted sand under water". In: *Terra et Aqua* 28 (1984), pp. 4–10.
64. S. Miedema. "The cutting of water saturated sand, the final solution". In: *WEDAXXV & TAMU37, New Orleans, USA* (2005).
65. M. A. Mooney, B. Walter, and C. Frenzel. "Real-time tunnel boring machine monitoring: A state of the art review". In: *North American Tunneling, 2012 proceedings* (2012), pp. 73–81.
66. K. Mosavat. "A smart disc cutter monitoring system using cutter instrumentation technology". In: *RETIC Proceedings*. 2017.

67. S. A. F. Murrell. "A criterion for brittle fracture of rocks and concrete under triaxial stress and the effect of pore pressure on the criterion". In: *Rock mechanics* (1963), pp. 563–577.
68. E. Oñate et al. "The particle finite element method. An overview". In: *International Journal of Computational Methods* 1.02 (2004), pp. 267–307.
69. A. Pandolfi, B. Li, and M. Ortiz. "Modeling failure of brittle materials with eigenosion". In: *Computational Modelling of Concrete Structures* 1 (2013), pp. 9–21. <https://doi.org/10.1007/s10704-012-9788-x>.
70. M. L. Parks et al. *Peridigm Users' Guide v1. 0.0*. Tech. rep. Sandia National Laboratories, 2012.
71. M. S. Paterson and T.-F. Wong. *Experimental rock deformation-the brittle field*. Springer Science & Business Media, 2005.
72. R. Plinninger et al. "Testing conditions and geomechanical properties influencing the CERCHAR abrasiveness index (CAI) value". In: *International Journal of Rock Mechanics and Mining Sciences* 40 (2003), pp. 259–263.
73. S. Priebe et al. "Comparison of Hilbert Transform and Complex Demodulation for Defect Identification in Cutting Discs using Vibration-Based Feature Extraction". In: *European Workshop on Structural Health Monitoring*. Springer, 2020, pp. 564–572.
74. S. Priebe et al. "Vibration-Based Feature Extraction for Artificial Damages in Small Scale Cutting Discs of Tunnel Boring Machines". In: *The e-Journal of Nondestructive Testing* 26.12 (Dec. 2021).
75. R. B. Randall. *Vibration-based Condition Monitoring*. WILEY, July 2021. 448 pp. ISBN: 1119477557.
76. L. Röchter. *Systeme paralleler Scherbänder unter Extension im ebenen Verformungszustand*. Lehrstuhl für Grundbau, Boden-und Felsmechanik, 2011.
77. J. Rostami. "Development of soil abrasivity testing for soft ground tunneling using shield machines". In: *Tunneling and Underground Space Technology* 28 (2012), pp. 245–256.
78. J. Rostami. *Development of a force estimation model for rock fragmentation with disc cutters through theoretical modeling and physical measurement of crushed zone pressure*. Colorado School of Mines, Golden, CO, USA, 1997.
79. J. Rostami and L. Ozdemir. "A new model for performance prediction of hard rock TBMs". In: 1993.
80. J. Rostami, L. Ozdemir, and B. Nilson. "Comparison between CSM and NTH hard rock TBM performance prediction models". In:
81. A. Röttger et al. *Abrasion in Tunneling and Mining*. ICSCM, 2015.
82. U. K. Sahinoglu and U. Ozer. "The prediction of cutter wear from temperature measurements on TBM discs and cutting face". In: *Arabian Journal of Geosciences* 13.5 (Feb. 2020). <https://doi.org/10.1007/s12517-020-5188-0>.
83. L. Sanavia, B. Schrefler, and P. Steinmann. "A formulation for an unsaturated porous medium undergoing large inelastic strains". In: *Computational Mechanics* 28.2 (2002), pp. 137–151.
84. B. Schmidt, F. Fraternali, and M. Ortiz. "Eigenfracture: an eigendeformation approach to variational fracture". In: *Multiscale Modeling & Simulation* 7.3 (2009), pp. 1237–1266. <https://doi.org/10.1137/080712568>.
85. T. Scholz et al. "Fracture toughness from submicron derived indentation cracks". In: *Applied physics letters* 84.16 (2004), pp. 3055–3057. ISSN: 0003-6951.
86. J. H. Schön. *Physical properties of rocks: Fundamentals and principles of petrophysics*. Elsevier, 2015.
87. S. A. Silling. "Reformulation of elasticity theory for discontinuities and long-range forces". In: *Journal of the Mechanics and Physics of Solids* 48.1 (2000), pp. 175–209.
88. S. A. Silling et al. "Peridynamic states and constitutive modeling". In: *Journal of Elasticity* 88.2 (2007), pp. 151–184.

89. G. Singh and R. W. Zimmerman. “Modification of Griffith–McClintock–Walsh model for crack growth under compression to incorporate stick-slip along the crack faces”. In: *International Journal of Rock Mechanics and Mining Sciences* 72 (2014), pp. 311–318. <https://doi.org/10.1016/j.ijrmms.2014.09.020>.
90. T. Szwedzicki. “Indentation hardness testing of rock”. In: *International Journal of Rock Mechanics and Mining Sciences* 35.6 (1998), pp. 825–829. ISSN: 1365-1609. [https://doi.org/10.1016/S0148-9062\(97\)00334-3](https://doi.org/10.1016/S0148-9062(97)00334-3).
91. D. Tabor. “Indentation Hardness and Its Measurement: Some Cautionary Comments”. In: *Microindentation Techniques in Materials Science and Engineering: A Symposium Sponsored by ASTM Committee E-4 on Metallography and by the International Metallographic Society, Philadelphia, PA*, ASTM International, p. 129. ISBN: 0803104413.
92. R. Teale. “The concept of specific energy in rock drilling”. In: *International Journal of Rock Mechanics and Mining Sciences & Geomechanics Abstracts* 3.1 (1965), pp. 57–73. ISSN: 0148-9062. [https://doi.org/10.1016/0148-9062\(65\)90022-7](https://doi.org/10.1016/0148-9062(65)90022-7).
93. K. Terzaghi. “Die Berechnung der Durchlässigkeitsziffer des Tones aus dem Verlauf der hydromechanischen Spannungserscheinungen”. In: *Sitzungsberichte der Akademie der Wissenschaften in Wien, mathematisch-naturwissenschaftliche Klasse* 132 (1923), pp. 125–138.
94. K. Terzaghi. *Theoretical soil mechanics*. Wiley, New York, 1943.
95. K. Thuro et al. “Soil Abrasivity Assessment Using the LCPC Testing Device”. In: *Felsbau* 24 (2006), pp. 37–45.
96. V. Vajdova, P. Baud, and T.-f. Wong. “Compaction, dilatancy, and failure in porous carbonate rocks”. In: *Journal of Geophysical Research: Solid Earth* 109.B5 (2004).
97. M. T. Van Genuchten. “A closed-form equation for predicting the hydraulic conductivity of unsaturated soils”. In: *Soil Science Society of America Journal* 44.5 (1980), pp. 892–898.
98. F. Wang et al. “Optimum Design and Application Research of Eddy Current Sensor for Measurement of TBM Disc Cutter Wear”. In: *Sensors* 19.19 (Sept. 2019), p. 4230. <https://doi.org/10.3390/s19194230>.
99. H. Wang et al. “Research on rolling bearing state health monitoring and life prediction based on PCA and Internet of things with multi-sensor”. In: *Measurement* 157 (June 2020), p. 107657. <https://doi.org/10.1016/j.measurement.2020.107657>.
100. D. Wingender and D. Balzani. “Simulation of crack propagation based on eigenosion in brittle and ductile materials subject to finite strains”. In: *Archive of Applied Mechanics* (2022), pp. 1199–1221. <https://doi.org/10.1007/s00419-021-02101-1>.
101. D. Wingender and D. Balzani. “Simulation of crack propagation through voxel-based, heterogeneous structures based on eigenosion and finite cells”. In: *Computational Mechanics* (2022), pp. 1–22. <https://doi.org/10.1007/s00466-022-02172-z>.
102. D. Wingender et al. “Simulation of ductile crack propagation in metal matrix composites – Comparison with cyclic experiments”. In: *PAMM* 21.1 (2021), e202100113. <https://doi.org/10.1002/pamm.202100113>.
103. P.-A. von Wolffersdorff. “A hypoplastic relation for granular materials with a predefined limit state surface”. In: *Mechanics of Cohesive-frictional Materials* 1.3 (1996), pp. 251–271. ISSN: 1099-1484.
104. D. M. Wood. *Soil Mechanics: A One-Dimensional Introduction*. Cambridge University Press, 2009. <https://doi.org/10.1017/CBO9780511815553>.
105. H. Yang et al. “Normal indentation of rock specimens with a blunt tool: role of specimen size and indenter geometry”. In: *Rock Mechanics and Rock Engineering* (2022).
106. L. J. Yin et al. “Use of indentation tests to study the influence of confining stress on rock fragmentation by a TBM cutter”. In: *International Journal of Rock Mechanics and Mining*

- Sciences* 72 (2014), pp. 261–276. ISSN: 1365-1609. <https://doi.org/10.1016/j.ijrmms.2014.07.022>.
107. H. Zhang et al. “Experimental investigation of deformation and failure mechanisms in rock under indentation by digital image correlation”. In: *Engineering Fracture Mechanics* 96 (2012), pp. 667–675. ISSN: 0013-7944. <https://doi.org/10.1016/j.engfracmech.2012.09.012>.
108. W. Zhu, P. Baud, and T.-F. Wong. “Micromechanics of cataclastic pore collapse in limestone”. In: *Journal of Geophysical Research: Solid Earth* 115.B04405 (2010), B04405. ISSN: 0148-0227. <https://doi.org/10.1029/2009JB006610>.
109. H. Zoubek, S. Villwock, and M. Pacas. “Frequency Response Analysis for Rolling-Bearing Damage Diagnosis”. In: *IEEE Transactions on Industrial Electronics* 55.12 (2008), pp. 4270–4276. <https://doi.org/10.1109/TIE.2008.2005020>.

Open Access This chapter is licensed under the terms of the Creative Commons Attribution 4.0 International License (<http://creativecommons.org/licenses/by/4.0/>), which permits use, sharing, adaptation, distribution and reproduction in any medium or format, as long as you give appropriate credit to the original author(s) and the source, provide a link to the Creative Commons license and indicate if changes were made.

The images or other third party material in this chapter are included in the chapter’s Creative Commons license, unless indicated otherwise in a credit line to the material. If material is not included in the chapter’s Creative Commons license and your intended use is not permitted by statutory regulation or exceeds the permitted use, you will need to obtain permission directly from the copyright holder.

